ALMA MATER STUDIORUM
UNIVERSITÀ DI BOLOGNA

DOTTORATO DI RICERCA IN

SCIENZE E TECNOLOGIE AEROSPAZIALI
Ciclo 37

Settore Concorsuale: 09/A1 - INGEGNERIA AERONAUTICA, AEROSPAZIALE E NAVALE
Settore Scientifico Disciplinare: ING-IND/06 - FLUIDODINAMICA

EXPERIMENTAL ANALYSIS OF TURBULENT FLOWS AT HIGH REYNOLDS NUMBERS IN THE CICLOPE "LONG PIPE"

Presentata da: Lorenzo Lazzarini

Coordinatore Dottorato

Dario Modenini

Supervisore

Alessandro Talamelli

Co-supervisore

Gabriele Bellani

Esame finale anno 2025

"I’ve missed more than 9,000 shots in my career. I’ve lost almost 300 games. Twenty-six times I’ve been trusted to take the game-winning shot and missed. I’ve failed over and over and over again in my life. And that is why I succeed."

Micheal Jordan

Abstract

Lorenzo Lazzarini 2024, **Experimental analysis of turbulent flows at high Reynolds numbers in the CICLoPE "Long Pipe"**, Università degli Studi di Bologna, Doctoral Course in Aerospace Science and Technology (DAST), *Cycle XXXVII*

This thesis aims to investigate wall shear stress uncertainties and asymptotic scaling laws in turbulent pipe flows, with a focus on their implications for active flow control strategies. The experiments were conducted mainly at the Long Pipe facility of the CICLoPE laboratory at the University of Bologna, a state-of-the-art facility designed to reproduce canonical turbulent pipe flow across a wide range of Reynolds numbers while minimizing measurement uncertainties related to spatial resolution. This research include the development and refinement of the Oil Film Interferometry (OFI) as a direct local measurement technique for wall shear stress in the Long Pipe and a comprehensive uncertainty analysis comparing OFI with static pressure drop methods, classical methodology to obtain global wall shear stress in pipe flows. These findings enabled the reduction of overall uncertainties in determining asymptotic scaling laws. Additionally, OFI was applied to active flow control scenarios, demonstrating its versatility. Further investigations into wall-pressure fluctuations revealed their scaling behavior and coherence with near-wall velocity fluctuations both streamwise and wall-normal. A consistent linear correlation in the logarithmic region of the flow highlights the potential for scalable, real-time flow control applications. These results affirm the CICLoPE facility's significant role in advancing the understanding of wall-bounded turbulence and its application to active drag reduction strategies.

Key-words: Wall turbulence, Pipe flow, high Reynolds number, wall shear stress, OFI, Hot-wire, X-wire, POD, hPOD, CSA, spectra, statistics, Wall-pressure–velocity coherence, active flow control

Table of contents

Chapter 1

Introduction

1.1 Background

"When I meet God, I am going to ask him two questions: why relativity? And why turbulence? I really believe he will have an answer for the first." This quote, often attributed to physicist Werner Heisenberg, encapsulates the mystery and complexity that turbulence presents to scientists even today. Turbulence is a phenomenon everyone has encountered: the wake trailing behind a boat, the swirling smoke rising from a chimney, or the ever-shifting clouds driven by the wind. It also plays a crucial role in our daily lives: whether in the fuel efficiency of cars and airplanes or in natural processes like atmospheric dynamics and ocean currents, which affect everything from weather patterns to the distribution of pollutants.

The study of turbulence has a rich history. Leonardo da Vinci was one of the first to observe and sketch turbulent flows, capturing the swirling motion of water in his notebooks with remarkable accuracy. However, the first systematic study came much later, in 1883, when Osborne Reynolds conducted groundbreaking experiments on the transition from laminar to turbulent flow in a glass pipe filled with water. His work laid the foundation for modern turbulence research, introducing the Reynolds number. He discovered that the process of transition is dominated by a specific dimensionless parameter:

$$Re = \frac{UL}{\nu} \tag{1.1}$$

where U is the flow velocity, L the characteristic length of the considered object (e.g.: Diameter in a pipe, half-width on a channel) and ν the kinematic viscosity of the flow considered.

Despite being the subject of extensive research over the past 140 years, and its wide-ranging applications in both industry and everyday life, many aspects of turbulence and the

theory behind it remain complex and not fully understood. Turbulence still lacks a precise and universally accepted definition. It often manifests as a highly irregular, three-dimensional system of eddies of varying sizes that continuously grow, interact, and dissipate. In the case of high Reynolds number wall-bounded turbulence, the complexity intensifies due to the wide range of scales involved. The larger eddies are primarily influenced by inertial forces and their size is constrained by the external geometry, while the smallest eddies are controlled by viscous forces, resulting in an intricate and multi-scale flow structure.

Unlike the largest scales, the smallest turbulent scales, known as Kolmogorov scales (named after the scientist who first theorized them in 1941), do not have a size that is determined by geometry. In fact, the range of turbulent scales and their dimensions are directly influenced by the Reynolds number. As the Reynolds number increases, the dissipation scales become progressively smaller in comparison to the larger ones, leading to what is known as scale separation—a hallmark of high Reynolds number regimes. This separation of scales is key to the self-sustaining nature of turbulence, as described by classical turbulence theory. Energy is supplied to the largest scales from the mean flow, and it is then transferred down to progressively smaller eddies through a mechanism known as the energy cascade. This process continues until viscous forces dominate over inertia at the smallest scales, where turbulent kinetic energy dissipates into heat, marking the endpoint of the energy cascade.

Further challenges arise from the inherent complexity of turbulence dynamics. The behavior of turbulent flows is so rich and multifaceted that a detailed understanding or prediction of their behavior remains achievable only for highly simplified cases, often based on unrealistic assumptions. This difficulty stems from the so-called closure problem of turbulence. The behavior of all fluid flows is governed by the Navier-Stokes equations, a set of nonlinear partial differential equations that are notoriously difficult to solve, with only a few exact solutions available for simplified scenarios. When the governing equations are subjected to Reynolds averaging, a traditional method used to separate the mean and fluctuating components of the flow, The non-linear terms generate new terms, which include quantities like Reynolds stresses, in addition to the mean velocity and pressure fields. However, this approach leads to an unclosed system of equations, where the number of unknowns exceeds the number of available equations. Essentially, for every new equation formulated to describe these additional unknowns, more variables are introduced, perpetuating the imbalance. In simple terms, a complete statistical description of turbulence would theoretically require an infinite number of equations to resolve all the interacting scales, thus making a direct solution practically impossible.

Direct Numerical Simulations (DNS) offer the only current method to fully solve the Navier-Stokes equations without relying on any simplifications or modeling assumptions.

DNS resolves all the scales of turbulence, from the largest eddies down to the smallest dissipative scales, by directly computing the entire spectrum of turbulent fluctuations. However, this approach is computationally expensive and requires immense processing power and memory, which limits its applicability to low Reynolds number flows. Although DNS has made significant advances in recent years, allowing simulations to reach Reynolds numbers comparable to the lower range observed in actual wind tunnel experiments, it still remains impractical for simulating high Reynolds number flows. The computational cost increases dramatically with Reynolds number due to the growing disparity between the largest and smallest scales of turbulence. As a result, DNS remains a powerful research tool for studying fundamental turbulence physics in controlled environments, but is not yet feasible for the high Reynolds number flows typical of industrial or environmental applications. Gaining a deeper understanding of the physics underlying high Reynolds number flows offers a twofold benefit. Firstly, it provides general insight into the behavior, nature, and dynamics of turbulent flows, contributing to our fundamental knowledge of turbulence. Secondly, it supports the development of more accurate models and predictions, which can have far-reaching applications. For example, improved understanding can aid in friction control strategies, potentially leading to enhanced efficiency in engineering systems such as pipelines, vehicles, and aircraft, where minimizing friction plays a critical role.

Friction becomes particularly significant when fluid flow interacts with surfaces, especially in wall-bounded turbulent flows. In such flows, turbulence originates in a thin region near the surface known as the boundary layer, a concept first introduced by Prandtl in 1904. Within this boundary layer, viscous forces dominate, causing the fluid's velocity to rapidly drop to zero as it approaches the wall. Despite its thinness, the boundary layer is crucial because it is where friction between the wall and the fluid begins to develop. This friction is not only a major contributor to energy loss in many practical situations, but it is also the driving mechanism of wall-bounded turbulence. As a result, friction is a key factor in scaling wall-bounded flows, and understanding it is essential for advancements in areas such as drag reduction.

In aerospace applications, where Reynolds numbers are high and the boundary layer developing on a surface becomes turbulent, the theme of drag reduction becomes particularly relevant. For example, at subsonic cruising speeds, around 50% of the total drag experienced by an aircraft during landing or take-off is due to friction, which can increase to 70% during cruise. Friction not only impacts fuel consumption but also affects emissions released into the atmosphere.For instance, reducing friction by just 1% could save a typical long-range aircraft around 4 million liters of fuel annually, significantly lowering operational costs and reducing environmental impact. Such savings would also cut down CO_2 emissions

by approximately 5,000 kg annually (IATA, 2020; ICAO, 2019). Given the global push to reduce CO_2 emissions by 40% by 2030, in line with initiatives like the Paris Agreement, understanding the underlying physics of friction becomes critical (Clean Sky 2 Initiative, 2021; World Economic Forum, 2021). A deeper exploration of these mechanisms will not only accelerate the development of technologies for drag reduction but also improve the accuracy of predictive models, benefiting both the aerospace industry and broader environmental efforts.

Measurement of wall shear stress poses several challenges, especially in high Reynolds number flows. One of the key difficulties is represented by the spatial resolution. To address these challenges and provide high-quality, high-Reynolds-number data, the CICLoPE (Center for International Cooperation in Long Pipe Experiments) laboratory was established. Central to this project is the construction of a new large-scale wind tunnel, known as the Long Pipe facility. The laboratory takes a unique approach: rather than achieving high Reynolds numbers through increased flow speed U or fluid density ρ, it leverages a large-scale setup by increasing L in Equation 1.1. This allows for both high Reynolds numbers and enhanced spatial resolution. The facility's specifications were determined by an international team of turbulence researchers, with the objective of reaching Reynolds numbers high enough to observe scale separation while maintaining compatibility with established measurement techniques and avoiding spatial resolution limitations.

In the Long Pipe, wall shear stress can be measured using the static pressure drop across the last 30–40 meters, though this yields a "global" measurement of wall shear stress. To minimize the uncertainty associated with wall shear stress and thus friction velocity, a parameter essential for scaling and comparing with other canonical flows, the Oil Film technique can be applied, offering a more localized approach to reduce uncertainties associated with friction effectively.

1.2 State-of-the-art

This section provides a brief overview of the key studies that form the basis of current research. The most relevant topics and unresolved questions are highlighted to contextualize the present work.

1.2.1 Friction measurements

The accurate measurement of wall-shear stress and skin friction is essential in the study of wall-bounded turbulent flows. These measurements provide critical insights into the behavior

of turbulent boundary layers and their influence on drag. Over the years, experimental techniques have evolved to meet the challenge of accurately capturing frictional forces at the wall in various turbulent flow regimes, particularly at high Reynolds numbers. The following are the key techniques used for friction measurements and their respective contributions to the field. One of the most widely used methods for measuring wall-shear stress is Oil-Film Interferometry (OFI), a technique that utilizes a thin layer of oil applied to the surface. The oil's thinning rate is monitored, as it correlates with the local wall-shear stress. OFI has been particularly valuable in high-resolution experiments in boundary layers and pipe flows due to its ability to capture small-scale variations of wall-shear stress. Segalini et al. (2015) discussed the precision of OFI in turbulent boundary layer measurements, though challenges such as calibration, surface contamination, and temperature variation remain important considerations.

Earlier, Tanner and Blows (1976) used oil-film techniques to measure skin friction in turbulent flows, helping to establish the method's reliability. Another historically significant direct measurement technique is the floating element method, which involves measuring the force exerted on a floating sensor element flush with the wall. Tanner and Blows (1976) provided early experimental results using this technique to capture wall-shear stress in turbulent boundary layers. This method offers high accuracy in controlled environments, but its sensitivity to external vibrations and noise limits its application in complex, high-speed flows . Wall shear stress transducers offer another direct method of measuring time-resolved wall-shear stress in turbulent flows. These transducers are typically embedded into the surface and can capture both the mean and fluctuating components of the shear stress at the wall. Ruedi et al. (2003) employed shear stress transducers to measure wall-shear stress in high-Reynolds-number turbulent boundary layers, demonstrating the method's utility in capturing unsteady flow features. (Naughton and Sheplak, 2002)

One of the most basic yet effective approaches for estimating wall-shear stress is the pressure drop method. This method relies on measuring the pressure loss over a defined length of a channel or pipe and using that to calculate the mean wall-shear stress. Squire (1961) used the pressure drop method extensively in turbulent boundary layers, providing foundational insights into friction in such flows . More recently, Ruedi et al. (2003) applied this technique in large experimental facilities, emphasizing the importance of long measurement sections to minimize uncertainties. However, the pressure drop method is inherently limited by its inability to provide spatially resolved wall shear stress measurements and by the influence of additional pressure losses, such as those due to flow separation or secondary flow structures, which can complicate the interpretation of results.

Another indirect method for estimating wall-shear stress involves measuring the velocity gradient near the wall. The velocity gradient is related to the wall-shear stress through the Newtonian assumption that relates shear stress to the velocity gradient in the viscous sublayer. Techniques such as hot-wire anemometry (HWA) and laser Doppler velocimetry (LDV) have been extensively used to acquire near-wall velocity profiles. From these measurements, wall-shear stress can be inferred. This method, however, requires extremely high spatial resolution near the wall, where velocity gradients are steep, and any slight errors in probe positioning can lead to significant measurement uncertainty. Ruedi et al. (2003) conducted extensive velocity gradient measurements using hot-wire anemometry to infer wall-shear stress in turbulent boundary layers, and their work remains a key reference for researchers working on high-Reynolds-number flows . Similarly, Naughton and Sheplak (2002) reviewed this method, noting the difficulties in applying it to high-speed flows where probe interference can introduce additional errors.

The Preston tube method is another classic technique where a cylindrical tube is positioned near the wall, and the pressure difference across it is used to infer wall-shear stress. Squire, Tanner, and Blows (1962) were among the first to develop empirical calibration curves for the Preston tube method, allowing it to be widely adopted in turbulent flow experiments . While relatively simple to use, this technique relies heavily on calibration and is limited to certain flow conditions where empirical relationships remain valid. Naughton and Sheplak (2002) also explored the limitations of this method, pointing out that it is generally reliable for low-to-moderate Reynolds numbers but becomes less accurate at very high Reynolds numbers.

One of the major challenges in friction measurements at high Reynolds numbers is the increasing difficulty in resolving the very fine scales near the wall where the shear stress is determined. Wall-shear stress can fluctuate rapidly in time and space, especially in turbulent boundary layers. As a result, uncertainty quantification has become an essential part of modern experimental studies, with methods such as Monte Carlo simulations used to estimate errors and improve the reliability of the data. For example, OFI measurements can be influenced by uncertainties in film thickness, surface contamination, and temperature, which must all be carefully controlled or modeled. Similarly, Ruedi et al. (2003) highlighted the limitations of hot-wire anemometry in near-wall measurements, noting the importance of precise calibration and sensor positioning to reduce uncertainty. Monkewitz and Nagib (2015) emphasized the scaling challenges at very high Reynolds numbers, showing how different methods can yield slightly different friction values due to scaling laws and probe interactions. Their work underscored the importance of consistent calibration and methodol-

ogy in friction measurements to ensure accurate comparisons across different facilities and flow regimes.

1.2.2 Turbulent structures

Despite the intrinsic chaos of wall-bounded turbulent flows, these flows exhibit a structured internal organization. Investigating the arrangement and interactions of these organized motions is essential for a better understanding of turbulence, its dynamics, and for improving control strategies. Although there is no universally accepted definition of organized motion, they are generally described as regions in space and time that involve mass and momentum transport. According to the traditional classification (Smits et al., 2011b), four main structures are identified: near-wall streaks, hairpin vortices, large-scale motions (LSMs), and very-large-scale motions (VLSMs). The basic units of these turbulent motions are the near-wall streaks, first observed by Kline et al. (1967) within the viscous sublayer (for $y^+ < 70$). These streaks develop in the streamwise direction, with a spanwise spacing of approximately $100\nu/u_\tau$, and are characterized by high or low momentum regions, independent of Reynolds number or flow geometry. Alternatively, hairpin or horseshoe vortices, as suggested by Adrian (2007), are considered the fundamental building blocks of coherent structures. Perry et al. (1986) also described turbulent flows as resembling a "forest" of hairpin vortices, first theorized by Theodorsen (1952) to extend across a wide range of scales, with a minimum height of about $100\nu/u_\tau$, originating at the wall.

Despite ongoing debates regarding the exact role of coherent structures in turbulence dynamics (Cantwell, 1981; Schoppa and Hussain, 1998), their significance and widespread presence in boundary layers were first strongly evidenced by the experimental observations of Head and Bandyopadhyay (1981) and later confirmed by the numerical work of Wu and Moin (2009). With recent advancements in computational power and measurement technologies, studies at higher Reynolds numbers have revealed the organization of these structures into larger formations known as large-scale motions (LSMs). Although many questions remain about their origin and dynamics, the prevailing theory (Ganapathisubramani et al., 2005; Guala et al., 2006; Kim and Adrian, 1999; Tomkins and Adrian, 2003) suggests that LSMs are formed by packets of hairpin vortices traveling at the same convection velocity.

Large-scale motions (LSMs) extend approximately 2-3 δ in the streamwise direction, with the heads of their hairpin vortices inclined at around 20° to the wall, a feature critical to their dynamics (Adrian et al., 2000). These structures contribute to turbulent bulges in the near-wall region by inducing low streamwise momentum between the vortex legs (Adrian et al., 2000; Ganapathisubramani et al., 2003). In 1999, Kim and Adrian (1999) identified even longer meandering structures characterized by low streamwise momentum flanked by

faster-moving fluid: the very-large-scale motions (VLSMs), also known as superstructures in boundary layers. Though their origin remains uncertain, they are thought to result from the alignment of LSM packets (Fig.1.1), which are centered in the logarithmic region and extend into the outer region in internal flows, but tend to break down in turbulent boundary layers (Bailey et al., 2010). Their meandering nature makes it difficult to accurately measure their true length using single-point statistics like spectra or correlations. Experimental studies using hot-wire rakes have captured structures in boundary layers extending up to 10-20 δ (Hutchins and Marusic, 2007a), while similar techniques in pipe and channel flows revealed structures stretching 20-30 radii or channel half-heights (Monty et al., 2007). Spectral analyses underscore the energetic and dynamic significance of LSMs and VLSMs. Feature detection algorithms and PIV data showed that these structures contribute about 50% of the Reynolds shear stress (Ganapathisubramani et al., 2005, 2003), with Balakumar and Adrian (2007) noting that modes with $\lambda_x/\delta > 3$ contribute up to 65% of the total turbulent kinetic energy.

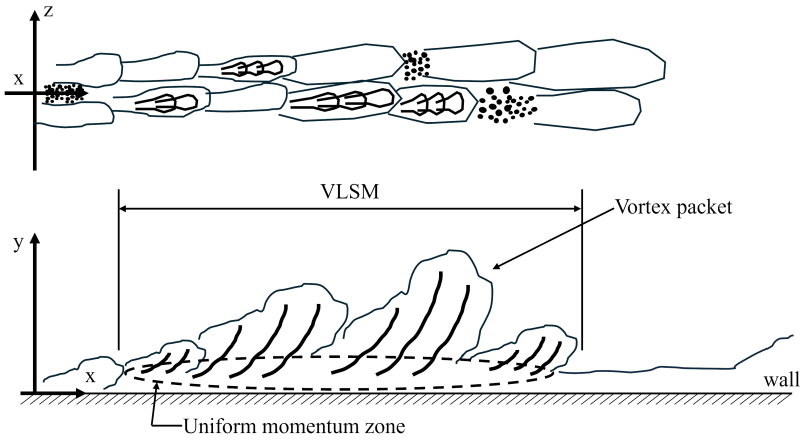

Fig. 1.1 Schematic of the alignment of the hairpin packets forminf in the large and very-large-scale motions. Reprinted from (Kim and Adrian, 1999)

The large wall-normal extension of LSMs and VLSMs suggests a potential correlation with the near-wall region. Studies by Mathis et al. (2009) and Hutchins and Marusic (2007b) demonstrated how these larger scales interact with the near-wall region through a combined effect of energy superposition and modulation of small-scale velocity fluctuations. Understanding the nature of this interaction could help resolve some of the controversies surrounding turbulence scaling in wall-bounded flows. For example, the interaction between small- and large-scale motions, observed in data from CICLoPE (Örlü et al., 2017) and by Klewicki and Falco (1990), as well as Hutchins et al. (2009), challenges the classical inner-scaling of streamwise turbulence intensity, which does not account for this dynamic.

However, this scaling has been validated by experiments conducted at the SuperPipe. More recently Discetti et al. (2019) had investigated VLSMs in the CICLoPE Long pipe combining classical anemometry with PIV acquisition along with an extended-POD-based dynamic estimation. Such approach enables the identification of "global" ejections and sweep events. Key findings indicate that low-momentum ejections are more frequent and persist longer than high-momentum sweeps, which tend to form closer to the wall and with more consistent radial thickness at $y/R \approx 0.25 - 0.30$.

1.2.3 The attached eddy hypothesis

This section provides a brief overview of the attached eddy model, focusing on its key hypotheses and the predictions derived from it. Originally formulated by Townsend (1976) and later expanded and refined in works by Perry and Chong (1982) and Perry et al. (1986), the attached eddy model is one of the few models developed for wall turbulence. Over the years, it has generally received strong support from experimental data.

The Attached Eddy Hypothesis (AEH) conceptualizes wall-bounded flow as an ensemble of inertia-driven, self-similar coherent structures that are randomly distributed along the wall plane. According to the AEH, these coherent structures, or eddies, scale with the distance from the wall, with their heights following a geometric progression Perry and Chong (1982). To evaluate the self-similarity of coherent structures in wall-bounded flow, Del Alamo et al. (2006)) analyzed their sizes by examining the dimensions of vortex cores identified through thresholding the discriminant of the velocity gradient tensor, utilizing direct numerical simulation (DNS) datasets.

Their findings reveal that tall vortex clusters, which extend from the near-wall region (below 20 viscous units) to the logarithmic region, scale with the distance from the wall. Additionally, Hwang (2015) suggests that these self-similar structures can sustain themselves, playing a crucial role in driving wall-bounded turbulence. Experimentally, resolving the full velocity gradient tensor is challenging, so the streamwise velocity is often used as a substitute. For instance, Hellström et al. (2016) applied proper orthogonal decomposition (POD) to instantaneous snapshots of streamwise velocity in a radial–azimuthal plane of pipe flow. They observed that the POD mode shapes of radial–azimuthal structures in pipe flow follow a self-similar scaling progression, showing a direct relationship between azimuthal mode number and characteristic wall-normal extent. Marusic and Monty (2019) provides an excellent overview of key assumptions and limitations associated with the AEH.

Recently Baidya et al. (2019) uses a correlation-based metric to analyze wall-attached structures in wall-bounded turbulence. Unlike single-height correlation assessments relying on Taylor's hypothesis, synchronized measurements at two wall-normal positions are used.

Wall skin friction is measured with hot-film sensors, and velocity is recorded at multiple heights. This approach assesses coherence between turbulent scales and the wall-reference signal. The goal is to characterize the coherent part of the velocity signal linked to wall-attached structures in terms of wavelength ($\lambda_x = 2\pi/k_x$), transverse offset (Δs), and wall-normal offset (z), expanding previous observations to include Δs trends.

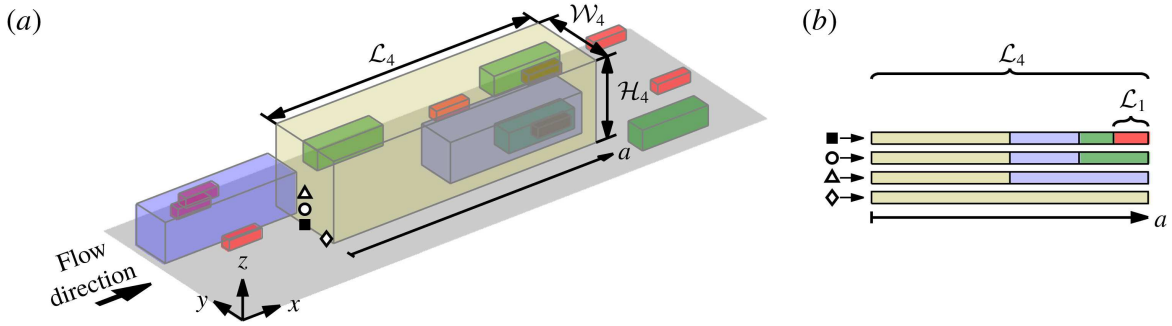

Fig. 1.2 The schematic illustrates a hierarchy of attached eddies employed to model wall-bounded flows. It displays four levels of hierarchy, with each level's volume of influence represented by differently colored cuboids, while the symbols indicate the probe locations. Part (b) shows the contributions or signals at four locations (as indicated by the corresponding symbols in part a) over a streamwise distance; the symbols denote the streamwise, spanwise, and wall-normal extents of the eddies at the nth hierarchy level. Reprinted from Baidya et al. (2019)

Figure1.2 presents a sketch that illustrates the relative scales in the Attached Eddy Hypothesis (AEH), where a hierarchy of self-similar structures is used to represent the logarithmic region of a wall-bounded flow. Each hierarchy level is depicted in a different color, and the sizes follow a geometric progression with a common ratio of 2, extending up to a height equal to the outer length scale. In this schematic, the population density decreases by half in both the x and y dimensions with each increment in hierarchy level. Consequently, Figure1.2 displays a total of four hierarchy levels, with eddies at each level characterized by their extents in the x, y, and z directions, denoted as L_i, W_i, and H_i, respectively. Now, consider probes positioned at ■ (measuring u_τ) and ∘ (measuring u), as illustrated in Figure1.2(a). The recorded signals from these probes are shown in Figure1.2(b). It is clear that the signal from the ∘ sensor lacks contributions from the smallest eddies compared to the signal from the ■ sensor.

1.2.4 Wall-pressure–velocity correlations

Turbulence stresses in wall-bounded flows are closely tied to the generation of skin-friction drag, driving interest in their relationship with wall-based quantities Renard and Deck (2016).

A key focus is the correlation between velocity fluctuations away from the wall and wall-pressure fluctuations (p_w), particularly for their potential use as input in real-time flow control systems aimed at reducing skin-friction drag. Achieving this requires developing transfer functions Sasaki et al. (2019) that allow the temporal dynamics of velocity structures to be inferred from minimally intrusive, wall-based measurements using sparse data inputs.

Research on wall-pressure fluctuations in turbulent wall-bounded flows has concentrated, among other aspects, on the scaling of intensity and spectral characteristics. These scaling trends depend on the friction Reynolds number, $Re_\tau \equiv \delta U_\tau/\nu$, where δ represents the boundary layer thickness (which, in our study, corresponds to the pipe radius R), $U_\tau \equiv \sqrt{\tau_w/\rho}$ denotes the friction velocity (with τ_w as the wall-shear stress and ρ the fluid density), and ν is the kinematic viscosity. Notable experimental studies that have evaluated this scaling include those by Farabee and Casarella (1991), Tsuji et al. (2007), and Klewicki et al. (2007). These studies identified a distinct inner-spectral peak at a frequency of $f_p^+ \approx 0.04$. The amplitude of this peak increases with rising Re_τ, along with the large-scale energy content. Over the past decade, computational research has corroborated these findings (*e.g.*, Jiménez and Hoyas, 2008; Panton et al., 2017) and demonstrated that, when examining spatial spectra, the inner-spectral peak is located at $\lambda_{x,p}^+ \approx 250$. Consequently, f_p^+ and $\lambda_{x,p}^+$ are related at the peak scale through a convection velocity of $U_c^+ \approx 10$.

Investigations have also been conducted on the relationships between wall-pressure events and velocity structures. For example, Thomas and Bull (1983) identified characteristic wall-pressure signatures linked to near-wall burst-sweep events that are exclusively confined to the near-wall region. Gibeau and Ghaemi (2021) examined the spatio-temporal correlation between wall-pressure and velocity fluctuations across a boundary layer, reporting a low but significant coherence at low frequencies for u and v fluctuations within the logarithmic region (where lower-case symbols denote fluctuations and upper-case symbols represent time-averaged quantities). They attributed this stochastic coupling to the presence of large-scale motions (LSMs). Connecting the wall-pressure field with LSM dynamics is particularly important for real-time flow control, as LSMs are a promising target for control strategies in wall-turbulence applications (Abbassi et al., 2017; Dacome et al., 2024a). This is due to their relatively long length and time scales, which result in intrinsically long formation times. Moreover, at friction Reynolds numbers relevant to practical applications, LSMs in the logarithmic region dominate energetically over the smaller scales (Hutchins and Marusic, 2007a) and account for the majority of turbulence kinetic energy production (Smits et al., 2011a). A recent study demonstrated a Reynolds-number-independent wall-scaling of the linear coherence between wall-pressure and u fluctuations in the logarithmic region of a turbulent boundary layer (TBL) at DNS-range Reynolds numbers (Baars et al., 2024).

Furthermore, it was found that wall-pressure squared exhibits a higher coherence with large-scale-filtered u fluctuations, indicating that the quadratic operator incorporates large-scale content. These findings align with an earlier conclusion by Naguib et al. (2001), which stated that the accuracy of stochastically estimating streamwise velocity fluctuations from wall-pressure improves when the quadratic term is considered.

1.3 Objectives and outline of the thesis

This thesis is part of a larger project aimed at developing both active and passive drag reduction strategies by investigating uncertainties in wall shear stress and asymptotic scaling laws in turbulent pipe flows. A more detailed delineation of the objective of this thesis can now be outlined. The primary objective of this research is to reduce friction drag through precise and innovative measurement techniques, leveraging the unique capabilities of the CICLoPE Laboratory and the Long Pipe facility. Due to the challenges inherent in high Reynolds number flows, an experimental approach is essential. This study addresses these challenges by first focusing on minimizing uncertainties in the measurement of wall shear stress, particularly those affected by spatial resolution limitations in the near-wall region. This goal is supported by the specialized design of the Long Pipe facility, which enables more accurate wall-shear stress measurements—a crucial factor, as friction velocity directly influences classical scaling laws (*e.g.*: the logarithmic law of the wall introduced by Theodore Von Kármán and later refined by Ludwig Prandtl. This law provides a fundamental framework for describing turbulent flow behavior near walls and has significant implications in engineering, especially for predicting drag and heat transfer in wall-bounded flows).

Effective drag control strategies require precise wall-shear stress measurements, but they also depend on accurate flow information, often obtained through velocity data. However, in practical applications, capturing velocity information is challenging, whereas wall pressure data are more accessible. Therefore, another key objective of this research is to explore the correlations between velocity and wall pressure, with the aim of utilizing wall pressure as a sensing element for open- or closed-loop drag reduction control strategies. This approach holds promise for advancing both the fundamental understanding of wall-bounded turbulence and its practical applications, such as friction control technologies. In support of these aims, the following specific objectives were identified:

- **Assess and minimize uncertainty on wall-shear stress measurements in the Long Pipe facility** Wall shear stress in the Long Pipe is commonly measured via static pressure drop over the last $40\,m$ of the pipe. The 'global' wall shear stress is computed combining two different experimental setups that handle the uncertainties differently.

Oil Film Interferometry (OFI) is then introduced in the Long Pipe facility as 'local' skin friction information computed in different sections of the pipe. A careful evaluation of the measurement technique is carried out assessing uncertainty related to the measurements itself, exploring effect of temperatures and different possible source of errors. A comparison between an optimized version of the static pressure drop technique and OFI is then addressed also comparing presents results with one coming from literature.

- **Scaling of wall-pressure fluctuations** Wall-pressure fluctuations measured using a sparse sensors setups of microphones are acquired. The acquired signals are then post-processed (filtered) using three different techniques: POD, harmonic POD and conditional spectral analysis aiming at the minimization of the noise sensed by the instrumentation and retaining only hydrodynamic wall pressure fluctuations. Inner and outer scaling laws in pressure fluctuations are addressed comparing data with available simulations. Finally, inner scaled pressure intensities are also compared to results proposed by Klewicki et al. (2007).

- **Wall-pressure–velocity coherence** Wall-pressure–velocity coherence is assessed by combining microphone measurements with velocity acquisition by means of Hot-wire spanning different relative position to understand the physics behind such correlations. X-wire are also implemented to obtain information related to wall-pressure and wall-normal component of the flow velocity, supposed to be the mostly coherent signal to wall-pressure fluctuations. In conclusion, the primary objective of this experimental activity is to validate the potential of using wall pressure information as a reliable sensing tool for active flow control strategies aimed at minimizing friction drag. By exploring correlations between wall pressure and flow dynamics, this research seeks to establish wall pressure as a practical and accessible sensing quantity scalable up to real life scenarios.

The thesis is structured as follows: Chapter 2 covers the mathematical tools and fundamental equations for fully developed turbulent pipe flow, including key concepts from the Navier-Stokes equations and scaling laws. Chapter 3 describes the experimental setup at the CICLoPE facility, detailing the instruments and methods used to measure wall shear stress and pressure in high-Reynolds-number flows. Chapter 4 presents the uncertainty assessment of wall shear stress measurements, focusing on Oil Film Interferometry and Monte Carlo simulations to evaluate potential errors. This chapter also compares results from OFI and static pressure drop measurements. Chapter 5 investigates wall-pressure–velocity correlations to explore their use in drag reduction strategies. Chapter 6 summarizes the main

findings, emphasizing uncertainties in wall shear stress measurements as well as scaling laws contribution to practical application for active flow control.

Chapter 2

Theoretical background

This chapter will provide the mathematical tools and definitions used in the thesis, as well as a theoretical basis on turbulent wall-bounded flows.

2.1 Pipe flow

To describe a pipe flow, we can start from the Navier-Stokes equations for an incompressible fluid, written in Eulerian form and neglecting body forces:

$$\frac{\partial U}{\partial t} + (U \cdot \nabla)U = -\frac{1}{\rho}\nabla p + \nu \nabla^2 U, \tag{2.1}$$

$$\nabla \cdot U = 0, \tag{2.2}$$

Equation 2.1 represents the momentum balance, while 2.2 is the conservation of mass (or continuity) equation. $U = (U, V, W)$ is the velocity vector, p is the pressure, $\rho = \text{const.}$ is the fluid density, and $\nu = \mu/\rho$ is the kinematic viscosity.

Considering that we are dealing with a turbulent flow, and the velocity $U(x,t)$ can be treated as a random variable, we apply the Reynolds decomposition technique to divide the random quantities into their mean and fluctuations about the mean:

$$U(x,t) = \bar{U}(x,t) + u(x,t), \tag{2.3}$$

where the over-bar $\bar{U}$ indicates averaged quantities, and the lower-case u letters represent fluctuations. Applying the Reynolds decomposition to the Navier-Stokes equations yields the Reynolds-averaged Navier-Stokes equations (RANS). These equations can be specialized for the case of a circular pipe. Given the axial symmetry of the problem, it is convenient

to define a cylindrical coordinate system (x, r, θ). The axial coordinate is denoted by x, the radial coordinate by r, originating from the pipe centerline and normal to the wall, and the angular coordinate is θ. The components of the velocity vector U in the coordinate system are (U, V, W), representing the streamwise, wall-normal, and spanwise components, respectively. In the Reynolds decomposition, the mean part is $(\bar{U}, \bar{V}, \bar{W})$, and the fluctuating part is (u, v, w). R represents the pipe radius.

A turbulent pipe flow is statistically axial-symmetric, so that:

$$W = u_w = v_w = \frac{\partial}{\partial \theta} = 0. \tag{2.4}$$

Considering equation 2.4 and substituting it into the RANS equations, the continuity equation and momentum balance in the x and r directions become:

$$\frac{\partial U}{\partial x} + \frac{1}{r}\frac{\partial}{\partial r}(rV) = 0; \tag{2.5}$$

$$\frac{\partial U}{\partial t} + U\frac{\partial U}{\partial x} + V\frac{\partial U}{\partial r} = -\frac{1}{\rho}\frac{\partial \bar{p}}{\partial x} - \frac{\partial}{\partial x}u^2 - \frac{1}{r}\frac{\partial}{\partial r}(r\overline{uv}) + \nu\nabla^2 U; \tag{2.6}$$

$$\frac{\partial V}{\partial t} + U\frac{\partial V}{\partial x} + V\frac{\partial V}{\partial r} = -\frac{1}{\rho}\frac{\partial \bar{p}}{\partial r} - \frac{\partial}{\partial x}\overline{uv} - \frac{1}{r}\frac{\partial}{\partial r}(rv^2) + \frac{w^2}{r} + \nu\left(\nabla^2 V - \frac{V}{r^2}\right). \tag{2.7}$$

If we assume the flow is statistically stationary and fully developed (i.e., no dependence on the axial coordinate x), we arrive at the following relations:

$$\frac{\partial}{\partial t} = 0; \tag{2.8}$$

$$\frac{\partial U}{\partial x} = \frac{\partial u^2}{\partial x} = \frac{\partial v^2}{\partial x} = 0. \tag{2.9}$$

For the no-slip condition and axial symmetry, $V|_{r=R} = V|_{r=0} = 0$. Using the continuity equation (1.42), we conclude that the mean wall-normal velocity must be zero across the entire profile:

$$V = 0. \tag{2.10}$$

Substituting equations 2.8, 2.9, and 2.10 into the r component of the momentum equation, we get:

$$\frac{1}{\rho}\frac{\partial \bar{p}}{\partial r} + \frac{\partial v^2}{\partial r} = \frac{w^2}{r} - \frac{v^2}{r}. \tag{2.11}$$

Integrating equation 2.11 between a generic radial coordinate r and R, we obtain:

$$\frac{1}{\rho}(p_w - \bar{p}) - v^2 = \int_R^r \left(\frac{w^2}{r} - \frac{v^2}{r}\right) dr, \tag{2.12}$$

where the subscript w indicates the wall, at $r = R$. Taking the x derivative of 2.12 and using the assumption of fully developed flow 2.9, we obtain the result:

$$\frac{\partial \bar{p}}{\partial x} = \frac{\partial p_w}{\partial x}. \tag{2.13}$$

This implies that the axial pressure gradient is uniform across the pipe radius. Substituting 2.8, 2.9, 2.10, and 2.13 into the x component of the momentum equation, we get:

$$\frac{1}{\rho}\frac{dp_w}{dx} = -\frac{1}{r}\frac{d}{dr}(r\overline{uv}) + \nu\frac{1}{r}\frac{d}{dr}\left(r\frac{dU}{dr}\right). \tag{2.14}$$

Introducing the total shear stress $\tau(r)$ as:

$$\tau = \mu\frac{dU}{dr} - \rho\overline{uv}. \tag{2.15}$$

Equation 2.13 can be rewritten as:

$$\frac{dp_w}{dx} = \frac{1}{r}\frac{d(r\tau)}{dr}, \tag{2.16}$$

which can be integrated from 0 to R:

$$\tau_w = \frac{R}{2}\frac{dp_w}{dx}. \tag{2.17}$$

Equation 2.17 provides an analytical link between the axial pressure gradient and the wall friction τ_w, a crucial relationship in experimental investigations of pipe flows. If we integrate up to a generic r instead of R, and introduce the variable $y = R - r$ (the wall-normal distance), we get the general relation:

$$\tau(y) = \tau_w\left(1 - \frac{y}{R}\right), \tag{2.18}$$

which shows a linear relationship, decreasing from the wall where $\tau = \tau_w$, to the centerline where $\tau = 0$.

2.1.1 Pressure fluctuation equation

Considering the divergence of the Navier-Stokes equations, we obtain the Poisson equation for the instantaneous pressure $\tilde{p}$:

$$\frac{1}{\rho}\nabla^2 p = -\frac{\partial U}{\partial x}\frac{\partial V}{\partial y}, \tag{2.19}$$

The Reynolds decomposition, $p = \overline{p} + p'$ of equation (2.19) leads to a Poisson equation for p with two differet source term:

$$\frac{1}{\rho}\nabla^2 p = -2\frac{\partial \overline{U}}{\partial y}\frac{\partial v}{\partial x} - \frac{\partial^2}{\partial x \partial y}(uv - \overline{uv}), \tag{2.20}$$

where $\overline{uv}$ denotes time averaged quantities. On the basis of this equation, the fluctuating pressure field ca be decomposed into three main contributions:

$$p = p^{(r)} + p^{(s)} + p^{(h)}. \tag{2.21}$$

The rapid pressure $p^{(r)}$ can be expressed as:

$$\frac{1}{\rho}\nabla^2 p = -2\frac{\partial \overline{U}}{\partial y}, \tag{2.22}$$

the slow pressure $p^{(s)}$ satisfies

$$\frac{1}{\rho}\nabla^2 p = \frac{\partial v}{\partial x} - \frac{\partial^2}{\partial x \partial y}(uv - \overline{uv}), \tag{2.23}$$

moreover, the harmonic pressure $p^{(h)}$ satisfies Laplace's equation $\nabla^2 p^{(h)} = 0$. The term "rapid pressure" refers to its immediate response to changes in the mean velocity gradient, dominating over the slow component in the rapid-distortion limit. The harmonic (or Stokes) component, in contrast, is generally negligible beyond the immediate vicinity of the wall and is often disregarded. The second term in equation (2.20) can also be written as $(\partial U/\partial y)(\partial V/\partial x)$. This term closely resembles the form of the instantaneous dissipation-rate term, leading to a strong correlation between regions of intense low pressure and thin vortical structures with high dissipation rates (see, for example, Cadot et al. (1995)).

2.2 Wall bounded turbulence scaling

Turbulence is typically classified into two main categories: free-shear flows, such as jets and wakes, and wall-bounded flows, including channel flow, boundary layers, and pipe flow. In free-shear flows, turbulence emerges from differences in velocity within the flow. In contrast, wall-bounded turbulence arises due to the influence of a solid surface, the viscosity of the fluid, and the no-slip condition, where the fluid velocity at the wall is effectively zero. This thesis concentrates on wall-bounded turbulence, with a specific focus on pipe flow. The presence of the wall introduces unique features and turbulent scales that require careful consideration. While the forthcoming analysis is broadly applicable to wall-bounded turbulent flows, for a more detailed understanding, readers are encouraged to consult Pope (2000).

According to classical analysis, wall-bounded turbulent flows can be divided into two regions: an inner region near the wall and an outer region farther from it. In the inner region, viscosity plays a major role, while the external geometry has little influence on the flow behavior. This implies that the near-wall behavior is similar across different flows, even under different external conditions. In the inner region, the dynamics of the flow are dominated by viscosity. The mean velocity U is influenced by wall friction τ_w, the wall-normal distance y, and the fluid's kinematic viscosity ν. The characteristic velocity scale in this region is the friction velocity u_τ, defined as:

$$u_\tau = \sqrt{\frac{\tau_w}{\rho}}, \tag{2.24}$$

where ρ is the fluid density. The characteristic length scale is the viscous length l^*, given by:

$$l^* = \frac{\nu}{u_\tau}. \tag{2.25}$$

From this, a viscous time scale can also be defined as:

$$t^* = \frac{l^*}{u_\tau} = \frac{\nu}{u_\tau^2}. \tag{2.26}$$

A characteristic Reynolds number for wall flows is the friction Reynolds number, which, for pipe flow, is the pipe radius normalized using inner variables:

$$Re_\tau = \frac{Ru_\tau}{\nu} = \frac{R}{l^*} = R^+. \tag{2.27}$$

In the inner region, dimensional analysis gives:

$$\frac{U}{u_\tau} = f\left(\frac{yu_\tau}{\nu}\right) = f\left(\frac{y}{l^*}\right). \tag{2.28}$$

By defining U^+ and y^+ as the mean velocity and wall-normal distance normalized using the inner variables u_τ and l^*, equation (5) becomes:

$$U^+ = f(y^+). \tag{2.29}$$

This is known as Prandtl's law of the wall, attributed to Prandtl (1926). In contrast, in the outer region of the flow (also called the core region for internal flows like pipe flow), viscosity becomes less significant. The relevant length scale is now determined by the external flow geometry, such as the channel half-height h, the boundary layer thickness δ, or the pipe radius R. The friction velocity u_τ remains the characteristic velocity scale, and the centerline velocity U_{cl} is introduced.

For the outer region of pipe flow, dimensional analysis yields:

$$\frac{U_{cl} - U}{u_\tau} = g\left(\frac{y}{R}\right). \tag{2.30}$$

This is known as von Kármán's velocity defect law, derived by von Karman (1930). The boundary between the inner and outer regions is not sharply defined; instead, there exists an overlap region where both inner and outer laws hold. This occurs when $l^* \ll y \ll R$, or equivalently, when u_τ or the friction Reynolds number Re_τ is large. In this overlap region:

$$f\left(\frac{yu_\tau}{\nu}\right) = g\left(\frac{y}{R}\right). \tag{2.31}$$

Following Millikan's (1938) derivation, differentiating equation (9) yields:

$$\frac{\partial}{\partial y}\left(\frac{U}{u_\tau}\right) = \frac{u_\tau}{\nu} f'\left(\frac{yu_\tau}{\nu}\right) = -\frac{1}{R} g'\left(\frac{y}{R}\right). \tag{2.32}$$

The only solution to this is when f' and g' are inversely proportional to y^+ and y/R, respectively. Integrating this leads to:

$$U^+ = \frac{1}{\kappa}\ln(y^+) + B; \tag{2.33}$$

$$U_{cl} - \frac{U}{u_\tau} = -\frac{1}{\kappa}\ln\left(\frac{y}{R}\right) + C. \tag{2.34}$$

Here, κ is the von Kármán constant, and B and C are additive constants. According to classical theory, these constants are universal for all wall-bounded flows. Equation (12) is

known as the logarithmic law of the wall or simply the log-law, originally derived by Prandtl using the concept of mixing length, although he arrived at the same conclusion.

2.3 Turbulence scales

One of the key features of turbulent flows is the existence of a wide range of eddy scales. The largest scales are typically associated with the macroscopic geometric characteristics of the flow: for a boundary layer, it is the boundary layer thickness δ; for a channel, it is the half-height $h/2$; and for pipe flow, it is the radius R. The concept of an energy cascade was introduced by Richardson (1922). Essentially, it states that turbulent kinetic energy is introduced into the flow at large scales via a production mechanism, then transferred in an inviscid manner to progressively smaller scales, until it is dissipated into heat at small scales by viscous forces. It follows that the dissipation rate ϵ at small scales must equal the rate at which energy is produced at large scales.

According to Richardson, eddies can be characterized by a length scale l, a velocity $u(l)$, and a time scale $\tau(l) = l/u(l)$. Large eddies have a characteristic length l_0 comparable to L, and a characteristic velocity u_0 comparable to the root mean square of turbulence intensity, which is comparable to U. Thus, the Reynolds number of the large eddies, $l_0 u_0/\nu$, is large, making viscous effects negligible.

Kolmogorov (1941) later theorized the smaller dissipative scales, now known as Kolmogorov scales. He observed that as l decreases, both $u(l)$ and $\tau(l)$ decrease. His theory can be summarized in three hypotheses:

- At sufficiently high Reynolds number, small-scale turbulence ($l \ll l_0$) becomes statistically isotropic.

This hypothesis is known as local isotropy. In other words, while large eddies are anisotropic (their statistics depend on the direction considered), small-scale turbulence "forgets" the information provided by the mean flow field and the boundary conditions. As a result, these statistics become universal:

- At sufficiently high Reynolds number, small-scale statistics have a universal form determined by ν and ϵ.

Here, ϵ is the mean rate of energy dissipation, and ν is the kinematic viscosity. Since dissipation of energy transferred from larger scales occurs at small scales via viscous processes, the characteristic length, velocity, and time scales of the dissipation range can be defined as:

$$\eta \equiv \left(\frac{\nu^3}{\epsilon}\right)^{1/4}; \tag{2.35}$$

$$u_\eta \equiv (\epsilon\nu)^{1/4}; \tag{2.36}$$

$$\tau_\eta \equiv \left(\frac{\nu}{\epsilon}\right)^{1/2}. \tag{2.37}$$

Here, η is known as the Kolmogorov length scale. Kolmogorov also derived the ratio between the size of the large eddies and the dissipative eddies (based on the relation $\epsilon \approx u_0^3/l_0$):

$$\frac{l_0}{\eta} \approx Re^{3/4}. \tag{2.38}$$

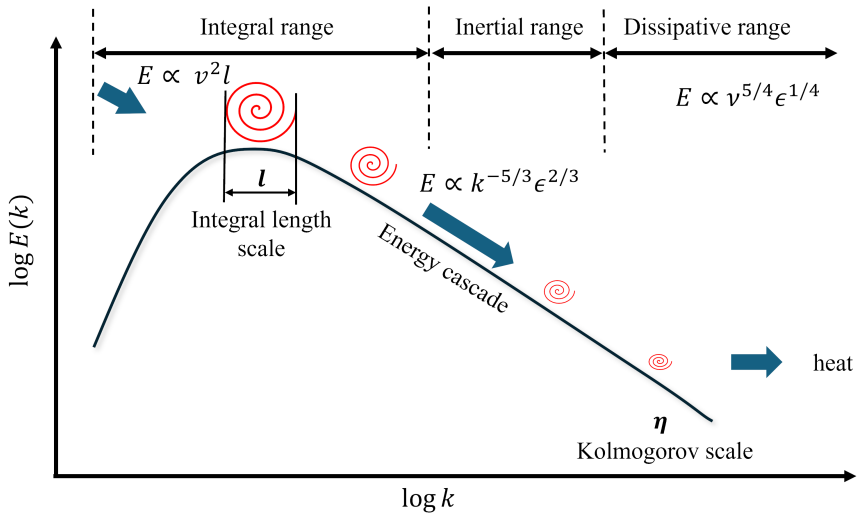

Fig. 2.1 Schematic of the energy cascade process

This shows that as the Reynolds number increases, the range of scales between l_0 and η also increases. At very high Reynolds numbers, there exists a range of scales that are much smaller than l_0 but still much larger than the Kolmogorov scale. This phenomenon, known as scale separation, implies that with increasing Reynolds number, the difference in physical dimensions between the large and dissipative scales increases nearly linearly. In practical terms, for a fixed external geometry (as in laboratory experiments), this means that η becomes progressively smaller. Kolmogorov's third and final hypothesis can be summarized as:

- At sufficiently high Reynolds number, the statistics for scales l (with $\eta \ll l \ll l_0$) have a universal form determined solely by ϵ and independent of ν.

This range of scales, known as the inertial sub-range, is only marginally affected by viscosity and depends almost exclusively on the energy transfer rate $T_e \approx \epsilon$. Consequently, its statistics are defined solely by the dissipation rate. Figure2.1 illustrates a schematic of the different scales and the energy cascade process.

2.4 Statistical tools

To study a chaotic process like turbulence, a statistical approach is essential because of the complexity of the phenomenon, which aligns more closely with the characteristics of a random process. This section offers a concise overview of the statistical concepts applied throughout the thesis.

2.4.1 Statistical moments

We can identify the *mean* as the first order statistical moment:

$$\langle U \rangle = \int_{-\infty}^{+\infty} U f(U) dU, \tag{2.39}$$

from the mean, the fluctuation can be determined:

$$u \equiv U - \langle U \rangle. \tag{2.40}$$

Since the mean value of fluctuations is always null, to further describe statistics of the process, higher-order moments need to be introduced. The second order moment is known as the *variance*:

$$\langle u^2 \rangle = \int_{-\infty}^{+\infty} u^2 f(U) dU. \tag{2.41}$$

The square root of the variance is typically known as the *standard deviation* or *root mean square*, that gives a measure of the typical fluctuations' magnitude:

$$\sigma_u = \sqrt{\langle u^2 \rangle}. \tag{2.42}$$

As defined above, other statistical moments can be now introduced, the n-th centered statistical moment of a random variable $u(t)$ is defined as:

$$\langle u^n \rangle = \int_{-\infty}^{+\infty} u^n f(U) dU, \tag{2.43}$$

we can identify of particular interest, related to the study of turbulence, the third- and fourth-order moments, also known as *skewness* and *flatness*. Often, they are normalized with the root mean square of appropriate order, giving the skewness and flatness factor:

$$S_u = \frac{\langle u^3 \rangle}{\sigma_u^3}; \; F_u = \frac{\langle u^4 \rangle}{\sigma_u^4} \tag{2.44}$$

The skewness and flatness factors are used to characterize specific properties of the probability density function (PDF). Skewness measures the asymmetry of the PDF, being zero for a perfectly symmetrical distribution. Flatness, on the other hand, indicates the relative peakedness or flatness of the distribution. For a Gaussian distribution, the skewness (S_u) is zero, while the flatness (F_u) is three.

2.4.2 Velocity averaging

In turbulence studies, the instantaneous velocity components, (U_i), are typically divided into their mean and fluctuating parts through a process known as Reynolds decomposition:

$$U_i = \langle U_i \rangle + u_i \tag{2.45}$$

where (U_i) represents the (i)-th component of the instantaneous velocity vector $(\mathbf{U})$, generally a function of time (t) and position $(\mathbf{x} = (x, y, z))$. $\langle U_i \rangle$ denotes the mean velocity component, while (u_i) is the fluctuating component. The mean value is most rigorously obtained through *ensemble averaging*. In experimental fluid dynamics, it is often not feasible to repeat the same experiment multiple times to calculate ensemble averages, especially for complex turbulent flows. Instead, we rely on the assumption that the flows being studied are statistically stationary and ergodic. The ensemble average, which is given by the equation:

$$\langle U_i \rangle (x,t) = \frac{1}{n} \sum_{j=1}^{n} U_{i,j}(x,t), \tag{2.46}$$

is theoretically the average taken over multiple realizations of the experiment, where $U_{i,j}(x,t)$ represents the i-th velocity component in the j-th realization. However, in practice, ensemble averaging is difficult or impractical due to limitations in conducting numerous identical experiments. For flows that are statistically stationary, their statistical properties do not change over time. This assumption allows the mean values to be calculated as a time average rather than an ensemble average. The temporal mean for a velocity component $_i(x,t)$ is then defined as:

$$\langle U_i \rangle(x) = \frac{1}{T} \int_0^T U_i(x,t)\, dt \tag{2.47}$$

where T is the total time of observation. This relationship implies that the time-averaged velocity at a point x will give the same statistical information as averaging over multiple realizations, a condition known as *ergodicity*.

2.4.3 Correlations

When the random variable is a function of time, the phenomenon is called a random process and will be indicated as $U(t)$. Even if the probability density function (PDF) is known at a certain location in the flow field, this does not provide information about existing statistical relations between two different points in the flow; indeed, very different statistical processes might have the same PDF. For this purpose, multi-time and multi-space statistical properties are used. The *auto-covariance* at the point x is defined as:

$$R(x,\tau) \equiv \langle u(x,t)u(x,t+\tau) \rangle \tag{2.48}$$

where τ is called the lag time. If the process is statistically stationary, the auto-covariance does not depend on t but only on τ. The auto-covariance gives an idea of the time that it takes for the process (the turbulent flow, in our case) to "forget" its past history at a particular point. From the auto-covariance, the correlation function can be defined as:

$$\rho(x,\tau) \equiv \frac{\langle u(x,t)u(x,t+\tau) \rangle}{\langle u(x,t)^2 \rangle} \tag{2.49}$$

It has the following properties:

1. $\rho(0) = 1$;
2. $|\rho(\tau)| \leq 1$.

In Figure XX, an example of the autocorrelation function for the streamwise velocity, $\rho_{uu}(\tau)$, is plotted against the lag time tau.

A time scale called the integral time scale can be defined as:

$$\Lambda_t \equiv \int_0^\infty \rho(\tau)\, d\tau. \tag{2.50}$$

Similar considerations on correlation can be made using space instead of time as the parameter. Covariance can be defined using fluctuations from different points in space but at

the same time, instead of the same point but different times. If this is the case, the covariance becomes a multi-space and single-time statistical property:

$$R_u(x,r) \equiv \langle u(x,t)u(x+r,t)\rangle. \tag{2.51}$$

From this, in the same manner as before, the spatial correlation function is defined as:

$$\rho_u \equiv \frac{\langle u(x,t)u(x+r,t)\rangle}{\langle u(x,t)^2\rangle}. \tag{2.52}$$

Here, r is the distance vector between the point x and the other point where fluctuations are measured. If the process is statistically stationary, both the covariance and the spatial correlation function are independent of the time t. Spatial correlation functions can be calculated in various ways, for example considering the spatial correlation of a velocity component u_i with itself (called spatial autocorrelation) or two different velocity components, referred to as cross-correlation. The autocorrelation can be longitudinal if r is parallel to u_i or transverse if it is perpendicular. Just like the temporal correlation, an integral scale can be defined. The integral length scale is:

$$\Lambda_l \equiv \int_0^\infty \rho_u(r)\, dr. \tag{2.53}$$

As can be seen in the integral for Λ_l, integration should ideally be applied over an infinite domain. That's obviously not feasible, both in experimental and numerical studies. To overcome this problem, the spatial correlation function is usually integrated up to its first zero value or, if there is one, to its minimum negative value.

2.4.4 Taylor's hypotesis

Although temporal and spatial correlations of a variable are theoretically and experimentally distinct (the former can be assessed using single-point measurements, while the latter necessitates multiple points), a question arises regarding any potential connection between the two. Specifically, when we obtain one type of correlation, can we infer anything about the other? Typically, it is more straightforward to conduct measurements at a single location over time rather than simultaneously across several points.

Taylor (1938) proposed a straightforward hypothesis suggesting that the time and spatial behaviors of a fluid-mechanics variable k along the mean flow direction are linked by the convection velocity U_c:

$$\frac{\partial k}{\partial t} \approx -U_c \frac{\partial k}{\partial x_1}. \tag{2.54}$$

This equation implies that the diffusion of quantity k and its transport in directions perpendicular to the mean flow are neglected. Although this may appear to be a simplistic approximation, experimental evidence supports its effectiveness in many conditions, with the convection velocity U_c being a critical factor. This hypothesis is commonly referred to as *frozen turbulence*, as Taylor's initial formulation assumes $U_c = U$ for all scales, indicating that the flow structures are "frozen" and are solely transported by the local mean velocity field. When analyzing spectral functions, Taylor's hypothesis permits the substitution of frequency along the mean flow direction with wavenumber.

However, experiments have shown that this simplification does not always hold true. For a more accurate application of the hypothesis, it is necessary to consider convection velocities that differ from the mean velocity. Studies by Romano (1995) and Del Alamo and Jiménez (2009) in wall turbulence indicated that a convection velocity lower than the local mean should be applied when close to the wall. It is generally accepted that while larger scales are conveyed by the mean flow velocity, smaller scales are transported at significantly lower velocities, which are influenced by the Reynolds number and the specific characteristics of the flow.

2.4.5 Power spectral density

The complete characterization of a random process cannot be derived solely from its probability density function (PDF). While correlations provide additional insights into the temporal and spatial evolution of the process, the spectral analysis describes how the energy of the random process is distributed across different frequencies. By presenting turbulence in the frequency domain, we can analyze how the energy of turbulent fluctuations is allocated among various frequencies and, using Taylor's hypothesis, associated scales.

To facilitate this analysis, the Fourier transform F can be utilized. The Fourier transform converts a time-domain function $f(t)$ into a new function, denoted $F(\omega)$, where the argument represents angular frequency ($\omega = 2\pi f$). The functions $f(t)$ and $F(\omega)$ are known as the time-domain and frequency-domain representations of the same event, respectively:

$$F(\omega) = \frac{1}{2\pi} \int_{-\infty}^{+\infty} e^{-i\omega t} f(t) dt. \tag{2.55}$$

For continuous signals, such as those typically encountered in experimental measurements, it is more practical to define a power spectral density (PSD), which indicates how the power of a signal or time series is distributed across various frequencies. The power P of a signal $u(t)$ can be expressed as:

$$P = \lim_{T\to\infty} \frac{1}{T} \int_0^{+\infty} u(t)dt; \tag{2.56}$$

however, for many signals of interest, the Fourier transform may not exist. Consequently, it is advantageous to work with a truncated Fourier transform $FT(\omega)$, in which the signal is integrated only over a finite interval:

$$F_T(\omega) = \frac{1}{\sqrt{T}} \int_0^{+\infty} u(t)e^{-i\omega t}dt. \tag{2.57}$$

The power spectral density can then be defined as:

$$S_{uu}(\omega) = \lim_{T\to\infty} \langle FT(\omega)\rangle; \tag{2.58}$$

a crucial property of the PSD is that for a statistically stationary process, it forms a Fourier transform pair with the autocovariance function $R(\tau)$:

$$S_{uu}(\omega) = \frac{1}{2\pi} \int_{-\infty}^{+\infty} e^{-i\omega\tau} R(\tau)d\tau, \tag{2.59}$$

the inverse transform is given by:

$$R(\tau) = \int_{-\infty}^{+\infty} e^{i\omega\tau} S_{uu}(\omega)d\omega; \tag{2.60}$$

for $\tau = 0$, this becomes:

$$u^2 = \int_{-\infty}^{+\infty} S_{uu}(\omega)d\omega. \tag{2.61}$$

Thus, $S_{uu}(\omega)$ can be interpreted as the variance (or turbulent energy) present within the frequency band of width $d\omega$ centered at ω . It is important to note that the power spectral density is an even function, i.e., $S_{uu}(\omega) = S_{uu}(-\omega)$. For our application, we will focus solely on positive frequencies; hence, we can define:

$$P_{uu}(\omega) = \begin{cases} 2S_{uu}(\omega) & \text{if } \omega > 0 \\ 0 & \text{if } \omega \leq 0, \end{cases} \tag{2.62}$$

typically, the frequency f is used instead of the angular frequency ω when representing the PSD in the frequency domain.

2.4.6 Spectral density estimation

When conducting spectral analysis on experimental data, we aim to estimate the spectral density of a random signal $u(t)$ from a finite set of time samples. The most straightforward approach is to apply a discrete Fourier transform (DFT) to the entire dataset, commonly known as the periodgram method. However, this approach introduces several issues. One primary issue is spectral bias caused by the abrupt truncation of the data, as a finite dataset can be viewed as a signal multiplied by a rectangular window function. Additionally, this method often results in a scattered and noisy spectrum.

To mitigate these issues, a window function that provides a more gradual truncation of the dataset is typically employed. The downside of using a window is that it introduces a loss factor since part of the data is artificially attenuated. To reduce random errors and achieve a more accurate spectral density estimate, the signal is divided into multiple segments, and the DFT is computed separately for each segment, with the results then averaged. This method yields a smoother and more accurate power spectral density (PSD) estimate, though at the expense of a reduced frequency range. The lower frequency limit is determined by the length of each individual segment.

For current measurements, the method proposed by Welch (1967) was used. Welch's method provides a smoother PSD estimate by calculating the DFT for different segments of data and then averaging them. It also minimizes the loss of information due to windowing by overlapping these segments. The method can be summarized as follows:

1. The sampled data $u(t)$, consisting of n points, is divided into N segments, each of length D, with each segment overlapping the next by $D/2$ points (50% overlap in this case).

2. A window function $w(t)$, such as a simple Hanning window, is applied to each segment in the time domain to reduce bias.

3. The DFT is computed for each windowed segment $u(t)w(t)$, and the square magnitude is calculated to obtain N spectral estimates.

4. These N spectral estimates are then averaged to produce the final PSD estimate.

Using this method, the PSD estimate $P_{uu}(f)$ is obtained. In some cases, the wavenumber spectrum is preferred over the frequency spectrum. To convert from frequency to wavenumber, Taylor's hypothesis is applied:

$$k = \frac{2\pi f}{U}, \tag{2.63}$$

where U is the local mean velocity. The wavenumber spectrum $\Phi_{uu}(k)$ can be derived from the PSD $P_{uu}(f)$ as follows:

$$\Phi_{uu}(k) = \frac{P_{uu}(f) \cdot U}{2\pi}. \tag{2.64}$$

Thus, by integrating the wavenumber spectrum over all wavenumbers, the variance of the signal is obtained:

$$u^2 = \int_0^\infty \Phi_{uu}(k) dk. \tag{2.65}$$

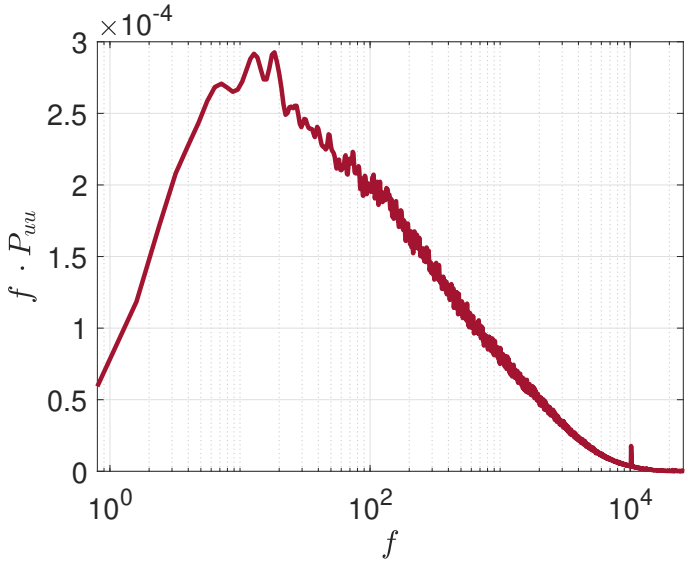

Fig. 2.2 Pre-multiplied power spectral density, P_{uu}, of a single hot wire probe measurement.

2.5 Filtering procedures

Here, we will present the fundamentals of the conventional POD, the harmonic POD and a spectral decomposition technique that offers a complementary framework for analyzing complex systems by decomposing the data into its constituent frequency components. To validate the effectiveness of these filtering procedures, we generate a synthetic signal comprising multiple sinusoidal components with added Gaussian noise, simulating the 6 different microphones we employed in the actual experimental campaign (see Fig. 6.2). The signal composition allows for a controlled analysis of each method's ability to extract the underlying sinusoidal components and perform noise-removal. We will apply conventional and harmonic POD following the terminology of Tinney et al. (2019), whereas the spectral sub-

traction methodology is based on the work of Richardson et al. (2023). Upon application of the algorithms to the proposed synthetic signal, we will compare the filtered results with the original, noise-free data.

2.5.1 Synthetic signals setup

A synthetic signal generator was implemented to create artificial signals that can be employed to test the filtering procedures before their applications on the actual sparse measurements of wall-pressure fluctuations from the CICLoPE facility. As will later be explained in Chapter 5, four unsteady wall-pressure sensors were employed, together with a fifth sensor, mounted on the centerline of the pipe, that monitored facility (acoustic) noise (see Fig. 6.2). Facility noise, caused by operation of the fan and mechanical vibrations of the pipe, propagates through the duct travelling at the speed of sound and maintaining high coherence at the locations of all five sensors employed. Turbulence-induced hydrodynamic wall-pressure fluctuations, instead, given the length scales of typical wall-pressure structures, retain very low correlation when convecting with the mean shear.

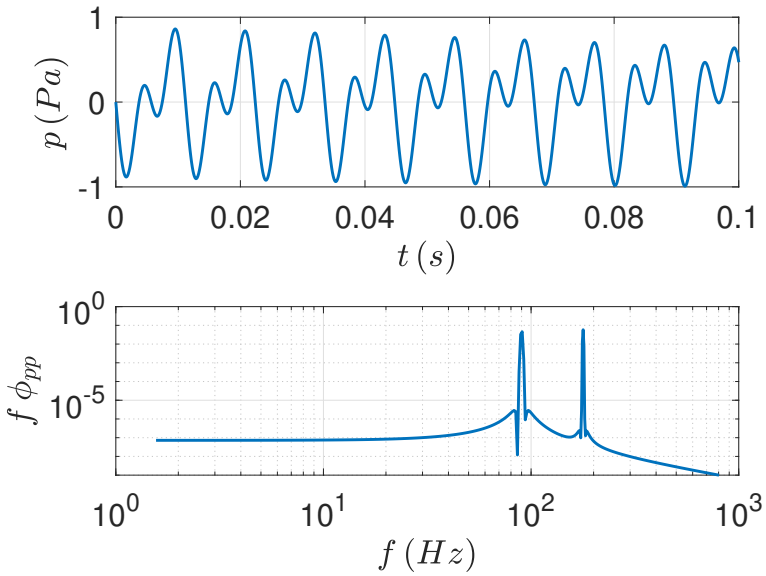

Fig. 2.3 Tonal peaks generated at 90 Hz and 190 Hz along with Power spectral density of the synthetic time series generated.

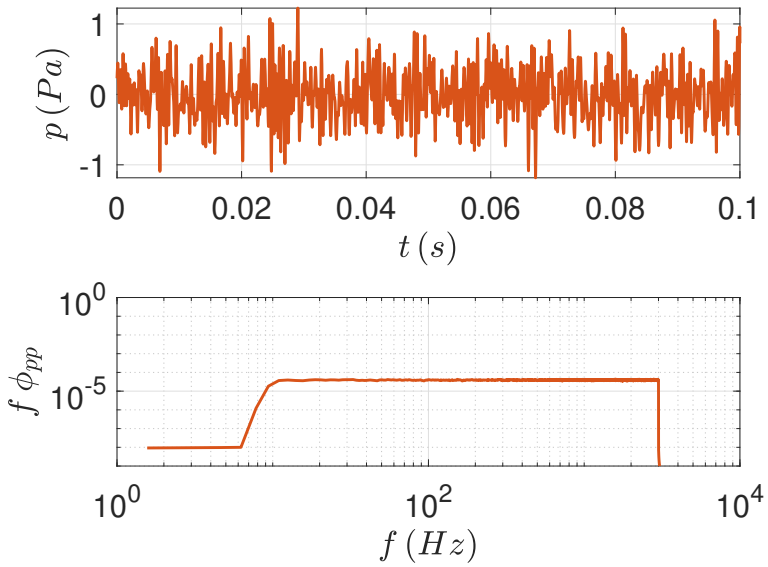

Fig. 2.4 Low SNR turbulence noise modeled as a broadband white noise. PSD of the noise.

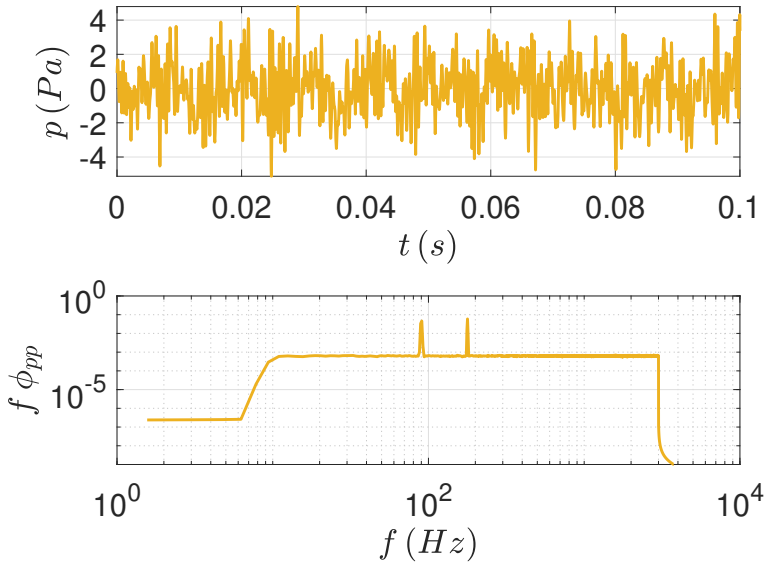

Fig. 2.5 Combined synthetic signal along with the power spectral density.

Given these characteristics, the synthetic signal simulates the acoustic noise by incorporating two arbitrary high-amplitude tones as can be seen from Fig.2.3 (at $f = 90$ Hz and at $f = 190$ Hz). Turbulence, instead, is modeled as broadband white noise in the band $10\,\text{Hz} < f < 2\,500\,\text{Hz}$ (see Fig.2.4). The four wall-pressure sensors are fed a signal resulting from the linear superposition of the two components (acoustic and turbulence-induced, see

Fig.2.5), with the amplitude of the acoustic tones being $\approx 50\times$ higher than the background turbulence-induced noise. The centerline microphone, instead, by design, does not measure wall-pressure fluctuations, but only records acoustic noise. By simulating such conditions, one can evaluate the effectiveness of the filtering techniques, such as POD, harmonic POD, or spectral analysis, to ensure that the final processed signal is free of undesired noise sources. Successfully filtering out these components allows for a more accurate representation of the desired flow information, ensuring more reliable data.

2.5.2 Proper Orthogonal Decomposition (POD)

Proper Orthogonal Decomposition (POD) calls for the definition of a kernel constructed by Hilbert-Schmidt's theory of integral equations with symmetric kernels. The general form for this kernel is written as follows:

$$R(\overrightarrow{x},\overrightarrow{x}') = \langle p(\overrightarrow{x},t)p^*(\overrightarrow{x}',t)\rangle. \tag{2.66}$$

Here, brackets $\langle\rangle$ denote ensemble averaging, $\overrightarrow{x}$ is a three-dimensional spatial vector, and $*$ denote the complex conjugate. Whether we choose to apply scalar or vector form of the technique will have a deep effect on both the size of the kernel and the number of times it is constructed. The integral eigenvalue problem thus becomes:

$$\int_0^L R(\overrightarrow{x},\overrightarrow{x}')\phi^{(n)}(\overrightarrow{x}')d\overrightarrow{x}' = \lambda^{(n)}\phi^{(n)}(\overrightarrow{x}'), \tag{2.67}$$

from which eigenvalues (λ) and eigenfunctions (ϕ) are obtained. It is clear from the formulation above that there is a unique kernel for each solution, thus implying that there is a unique (ϕ) for each mode. To generate a reduced order model, one must create the expansion coefficients by projecting the raw data onto the 'eigen modes':

$$a^{(n)}(t) = \int_0^L p(\overrightarrow{x},t)\phi^{(n)}(\overrightarrow{x})d\overrightarrow{x}. \tag{2.68}$$

They are both orthogonal and time varying. The model is then built as follows:

$$p^m(\overrightarrow{x},t) = \sum^m a^{(n)}(t)\phi^{(n)}(\overrightarrow{x}). \tag{2.69}$$

The sum is performed over POD modes defined in the range $m = n_1 : n_n$, or any unique combination of modes, for example $m = [n1, n4, n5]$. If all modes are retained in the construction of the reduced-order model, the starting signal will be obtained.

An application of classical spatial POD will be presented here using a synthetic signals to prove the effectiveness of the algorithm. POD eigenmodes as function of mode number and senor are depicted in Fig.2.6, where we can observe that modes 2,3, 4 and 5 contain significant information related to the signal, while mode 1 seem to be constant ad 'off' throughout every sensor. Figure 2.7 depicts the pre-multiplied power spectral densities of the denoised (blue) and original (green) signals. Upon inspection of the plots, one can immediately perceive how the tonal peaks of the synthetic signal are attenuated almost completely with respect to the original signal, while the broadband noise appears unaltered.

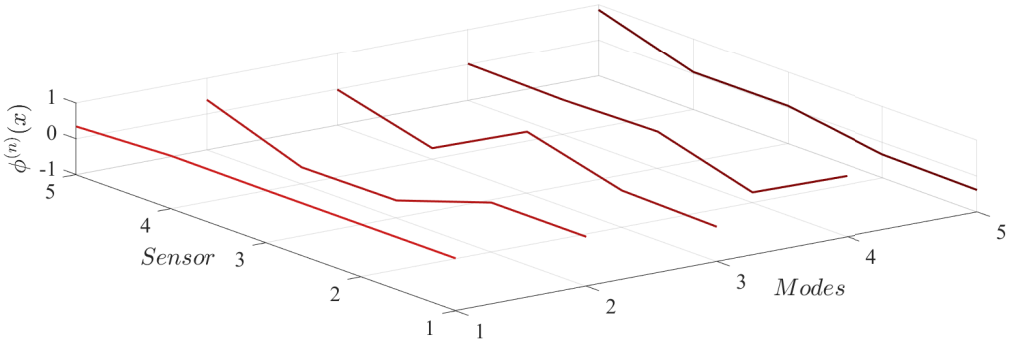

Fig. 2.6 $\phi^{(n)}(x)$ plotted as function of modes and considered sensors

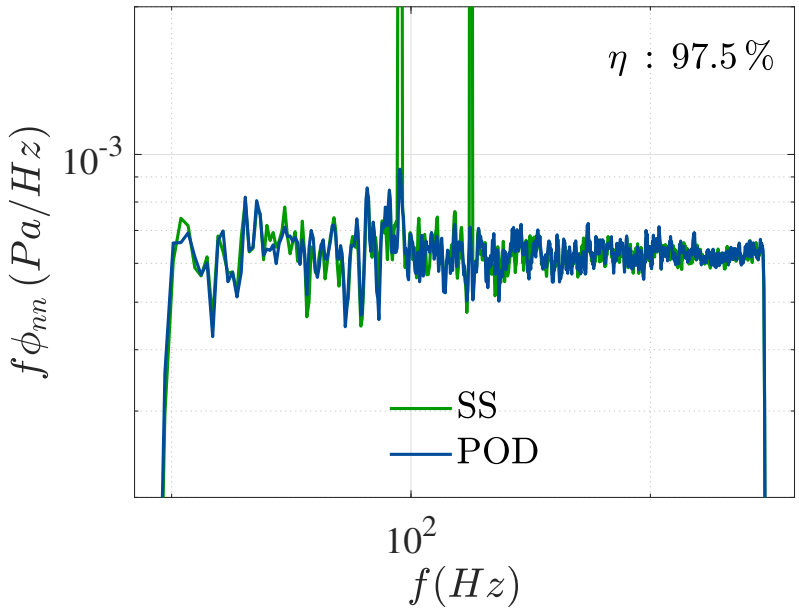

Fig. 2.7 Pre-multiplied power spectral density of the original synthetic signal (green) and the reconstructed synthetic signal using only POD modes 2, 3, 4, and 5 (blue line).

2.5.3 Harmonic Proper Orthogonal Decomposition (hPOD)

Applying a spectral-based kernel to tackle the POD eigenvalue problem resembles solving Eq.(2.67). In each scenario, the formulations condense any stationary, periodic, or homogeneous field direction (in space or time) into a collection of harmonic modes. The new kernel will then be defined as follows:

$$\check{R}(\overrightarrow{x},\overrightarrow{x}';f)=\frac{1}{2\pi}\int_{-\infty}^{+\infty}\langle p(\overrightarrow{x},t)p^{*}(\overrightarrow{x}',t+\tau)\rangle e^{-i2\pi f\tau}d\tau. \tag{2.70}$$

Such kernel can be used to solve the eigenvalue problem:

$$\int_{0}^{L}\check{R}(\overrightarrow{x},\overrightarrow{x}';f)\check{\phi}^{(n)}(\overrightarrow{x}';f)d\overrightarrow{x}'=\lambda^{(n)}(f)\check{\phi}^{(n)}(\overrightarrow{x};f). \tag{2.71}$$

We will then obtain random orthogonal expansion coefficients:

$$\check{a}(f)=\int_{0}^{L}\check{p}(\overrightarrow{x};f)\check{\phi}^{(n)*}(\overrightarrow{x};f)d\overrightarrow{x}. \tag{2.72}$$

Harmonic POD modes are arranged arbitrarily, and the system is then reconstructed at a given frequency, following the same procedure as for classical POD:

$$p^{m}(\overrightarrow{x};f)=\sum^{m}\check{a}^{(n)}(f)\check{\phi}^{(n)}(\overrightarrow{x};f). \tag{2.73}$$

The application of Harmonic Proper Orthogonal Decomposition (hPOD) to a set of five synthetic signals demonstrated effective signal decomposition and filtering. An analysis was performed by examining the dominant mode as a function of sensor position and frequency, revealing key insights into the behavior of the signals. To further validate the effectiveness of hPOD, pre-multiplied power spectral densities were compared between the original synthetic signals and the hPOD-filtered output (see Fig.2.8). This comparison highlighted a successful attenuation of two significant tonal peaks by 98.1% and 94.9%, respectively, indicating a reduction in unwanted frequency components. The parameter η was used to assess the filtering performance, representing the capability of the filtered signal to accurately reconstruct the original synthetic signal while effectively eliminating the tonal peaks. Notably, only the first mode, which is highlighted in the figure 2.9, was discarded during the reconstruction process to achieve a noise-free signal, highlighting the precision of hPOD in targeting specific frequency contributions while preserving the integrity of the signal.

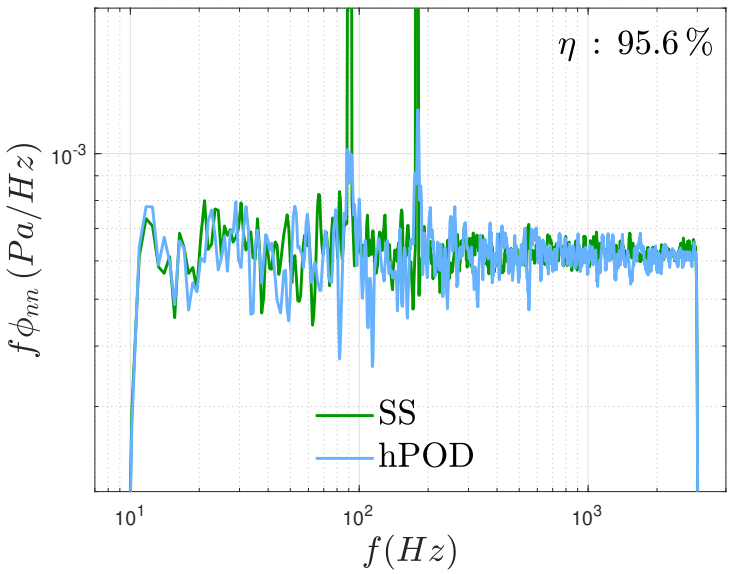

Fig. 2.8 Pre-multiplied power spectral densities of the raw synthetic data (highlighted in green) and reconstructed data using the harmonic POD technique (light blue), retaining only modes 2, 3, 4, and 5.

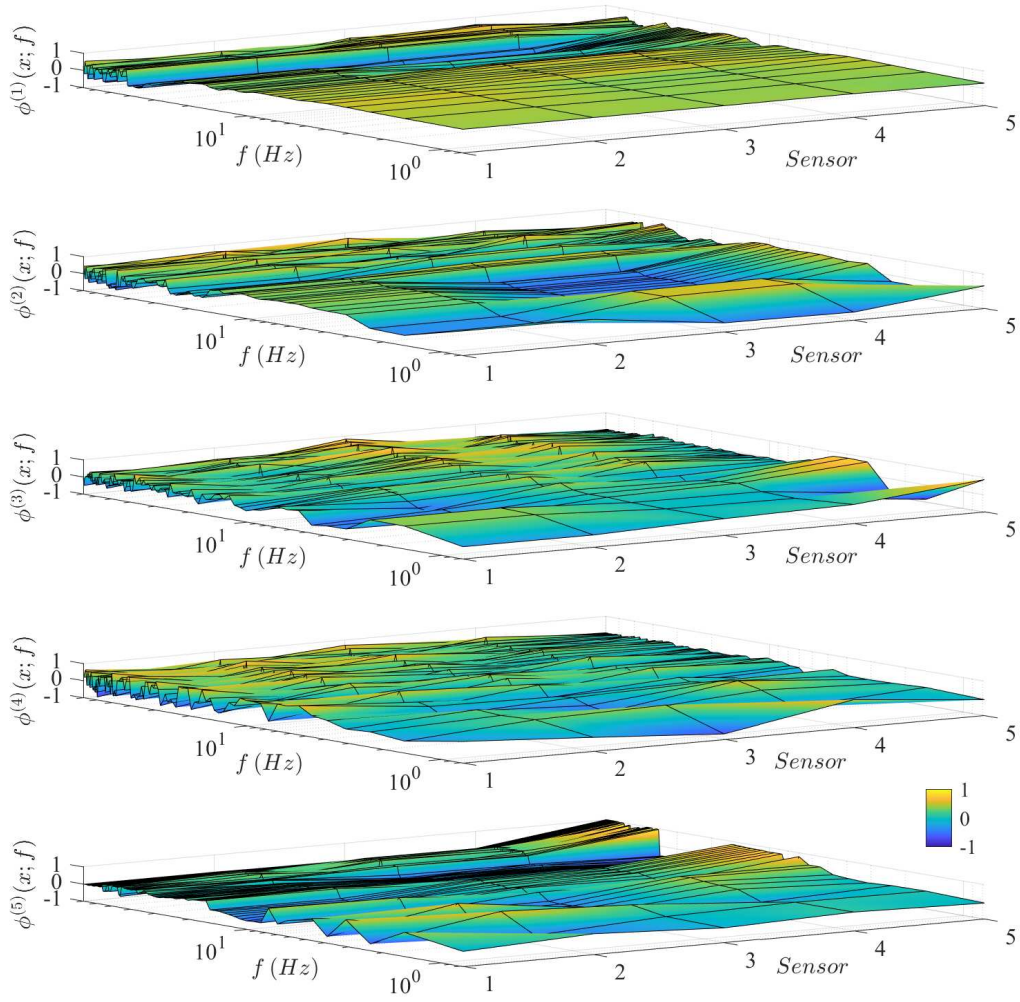

Fig. 2.9 $\phi^{(n)(x;f)}$, $n = 1:5$, plotted as a function of frequency and sensors.

2.5.4 Conditional Spectral Analysis (CSA)

Conditional spectra analysis is helpful when dealing with several noise sources and sensors. Richardson et al. (2023) proposed such a technique to remove facility noise adopting a multiple-input, multiple-output approach. Here, we implement the same methodology, only considering four contaminant signals.

Assume a linear relationship between a complex column vector of s measured partially coherent input contamination signal $C = \mathcal{F}(c)$, where C is defined as the Fourier transform

of the contamination signals c expressed as time series, and a corrupted column vector q of output signals $D = \mathcal{F}(d)$. The input contamination signals are individually filtered using an unknown complex matrix $H \in \mathbb{C}^{q \times s}$ and superimposed with the desired, yet unknown, considered signals $P = \mathcal{F}(p)$. The values of H are assumed not to be correlated with C and produce contaminated pressure signals D. The model is given by:

$$\underset{q\times 1}{D} = \underset{q\times s}{H}\ \underset{s\times 1}{C} + \underset{q\times 1}{P} \tag{2.74}$$

Multiplying by the complex conjugate transpose C^*, computing the spectral densities and considering that C and P are uncorrelated:

$$\underset{q\times s}{G_{cd}} = \underset{q\times s}{H}\ \underset{s\times s}{G_{c_k c_l}}. \tag{2.75}$$

The matrices G_{cd} and $G_{c_k c_l}$ represent, respectively, the cross-spectral densities between inputs and outputs and the auto-spectral densities of the inputs. We can solve the previous equation by matrix inversion provided that $G_{c_k c_l}$ is not singular:

$$H = G_{cd} G_{c_k c_l}^{-1}. \tag{2.76}$$

Our final goal is to obtain the cross-spectral densities of the raw pressure signals, so we isolate P:

$$\underset{q\times s}{P} = \underset{q\times 1}{D} - \underset{q\times s}{H}\ \underset{s\times 1}{C} \tag{2.77}$$

$$G_{p_k p_l} = G_{d_k d_l} - G_{cd}H' - HG_{dc} + G_{cd}G_{c_k c_l}^{-1}G_{c_k c_l}H' \tag{2.78}$$

$$= G_{d_k d_l} - HG_{dc} \tag{2.79}$$

$$= G_{d_k d_l} - G_{cd}G_{c_k c_l}^{-1}G_{dc}. \tag{2.80}$$

The diagonal and off-diagonal terms of $G_{p_k p_l}$ provide the denoised auto-spectral densities and cross-spectral densities, respectively. Figure 2.10 demonstrates the impact of the CSA filter on five synthetic signals. One served as the unknown pressure signal, while the other four acted as contamination sources. The pre-multiplied power spectral densities of the raw (green line) and de-noised (orange line) signals are displayed. The two peaks are clearly identified and attenuated: the second peak is fully filtered, while the first peak remains with an almost negligible intensity, as highlighted in the inset.

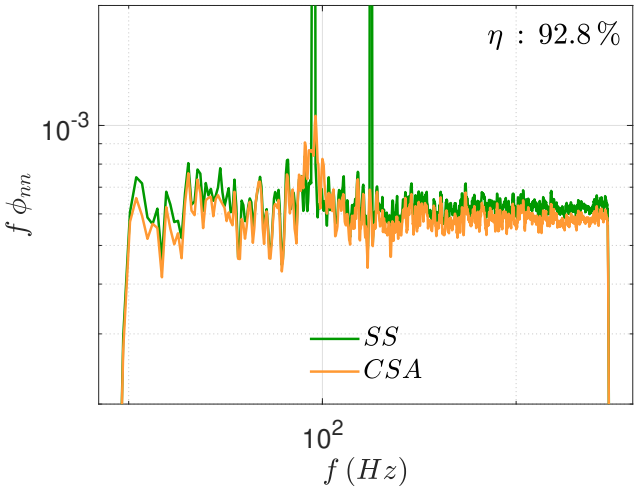

Fig. 2.10 Pre-multiplied power spectral density of the unfiltered synthetic signal (green) and the filtered signal using CSA (orange).

The application of three different filtering techniques: POD, hPOD, and CSA, to retain hydrodynamic fluctuations in synthetic signals with tonal peaks at 90 Hz and 190 Hz demonstrated that all techniques effectively detected and filtered out the tonal peaks. However, CSA partially retained the low-frequency peak (2.2%), while hPOD retained only 1.9% and 6.1% of the two tonal peaks, respectively. The effectiveness of the filtering methods was evaluated by the capacity to reconstruct the original signal, with reconstruction quality quantified through the integral of the pre-multiplied power spectra. All techniques achieved high-quality results, with reconstruction levels exceeding 90% of the original noise-free signal.

Figure 2.11 illustrates the differences between the pre-multiplied power spectral densities of the original synthetic signal (SS) and three filtering techniques, with each curve offset by two units to improve clarity. Instead of evaluating the overall reconstruction accuracy using integral differences between the SS and filtered signals, the focus here is on the normalized results, emphasizing the frequency content of the filtered signal. This approach allows us to identify local deviations or imperfections in the filtering process. The figure shows that both POD and hPOD effectively capture the original behavior of the synthetic signal, whereas CSA struggles to match the SS values, likely due to the low SNR of the synthetic data. Although POD and hPOD deliver more accurate reconstructions, they require careful mode selection to achieve optimal results. In contrast, CSA, despite its lower reconstruction accuracy—potentially due to the sparse configuration used—offers a simpler approach, as it does not require detailed consideration of mode shapes during processing. Additionally,

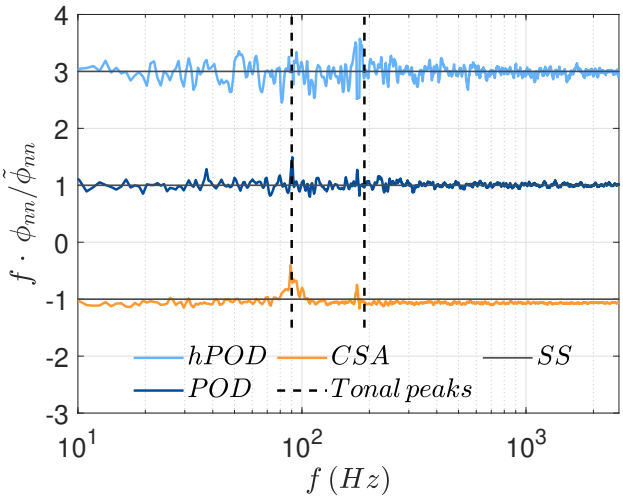

Fig. 2.11 difference between pre-multiplied power spectral densities of the filtered signal and original, noise-free, signal. light blue line refers to hPOD results, dark blue line highlight POD data while orange line depicts CSA filtering operation. The results are offset by 2 unit to enhance the accessibility of the figure. Black dashed line reports the location of the two tonal peaks respectively at $90\,Hz$ and $190\,Hz$. The three solid black lines presents the reference of the synthetic signal.

table 2.1 summarizes identification of tonal peaks, their effective attenuation, and each method's ability to reconstruct the original noise-free *SS*.

Filtering technique	Tonal peak $90\,Hz$	Tonal peak $190\,Hz$	$\eta\,(\%)$
POD	D/R	D/R	97.5 %
hPOD	$D/\approx R$	$D/\approx R$	95.6 %
CSA	$D/\approx R$	D/R	93.8 %

Table 2.1 Results of different filtering techniques applied to the synthetic signal. 'D' indicates the detection of the tonal peak, while 'R' denotes the successful removal of the peak. The percentage, η, represents the effectiveness in reconstructing the original noise-free signal.

Chapter 3

Facility and experimental Methods

3.1 CICLoPE "Long Pipe"

3.1.1 The need for a high *Re* facility

The idea behind the construction of the CICLoPE laboratory, and in particular the design of the Long Pipe, is to address critical research issues related to wall-bounded turbulence at high Reynolds numbers, combining for the first time well-established sensors with high accuracy. Despite the fact that high Reynolds number turbulence appears in numerous practical industrial and environmental applications, its richness and complexity challenge both numerical and experimental approaches. On one hand, current computational power is insufficient to obtain good statistics, and on the other, spatial resolution becomes a severe hindrance when opting for an experimental approach to investigate high Reynolds number regimes. The Long Pipe at CICLoPE was designed to enable fully resolved measurements using traditional instruments, something not possible in any other facility worldwide. The first requirement is to define the operational Reynolds number range, which must account for two fundamental features of high Reynolds number wall-bounded turbulence: a well-developed overlap region of the mean flow and a well-developed $k^{-5/3}$ region.

In wall-bounded turbulent flows, it is well-known that there is an overlap region where the mean flow is described by a logarithmic law (eq.2.33). The extent of this region is commonly accepted to be $200 < y^+ < 0.15R$, and to ensure sufficient spatial resolution, this region must extend for at least a decade, i.e., up to $y^+ \approx 2000$. Defining $y^+ = 2000l^*$, the constraint on the upper bound becomes:

$$2000l^* < 0.15R. \tag{3.1}$$

This leads to a lower bound on the operational Reynolds number ($Re_\tau = Ru_\tau/\nu = R/l^*$), giving:

$$Re_\tau > 1.33 \times 10^4. \tag{3.2}$$

To draw conclusions on the scaling behavior of turbulent flows, a factor of 3 is applied, leading to a minimum highest Reynolds number of 4×10^4. For the appearance of the $k^{-5/3}$ region in the spectra, according to Kolmogorov theory (confirmed by numerical and experimental results), sufficient separation between the Kolmogorov scale η and the energy-containing scales l_0 must be guaranteed. In pipe flow, the energy-containing scale is the pipe diameter R. Physically, this means that the $k^{-5/3}$ region should end at around a tenth of the wavenumber corresponding to the Kolmogorov scale, stretching for one order of magnitude in the wavenumber space, extending down to wavenumbers an order of magnitude smaller than the energy-containing scales D. Using a numerical dataset, for $Re_\tau = 14000$, the Kolmogorov scale at the centerline is $\eta_{CL} \approx 10.6 l^*$. For the constraints mentioned, the $k^{-5/3}$ region starts at approximately $10^6 l^*$ and extends for a decade until $10^6 l^*$, according to:

$$1060 l^* < 0.1 D. \tag{3.3}$$

In terms of Re_τ, this implies:

$$Re_\tau > 5.3 \times 10^3. \tag{3.4}$$

This condition is satisfied by the fully developed overlap region constraint, setting the operational range to $1.3 \times 10^4 < Re_\tau < 4 \times 10^4$. The next step is designing the facility to reach these high Reynolds numbers. Starting from the Reynolds number definition:

$$Re = \frac{\rho U L}{\mu}. \tag{3.5}$$

Several options exist to increase the Reynolds number. The most direct approach is to increase the velocity U, but this has two main drawbacks: it increases power demand significantly, and the velocity increment is limited by the onset of compressibility effects. Another approach is to decrease the viscosity μ, as done in cryogenic facilities. Alternatively, one could pressurize the facility to increase density, as is done in the SuperPipe at Princeton, where the pressure at the test section can reach up to 187 atm, achieving a maximum $Re_\tau \approx 10^5$. The strategy adopted in the large-scale CICLoPE facility is to increase the characteristic length L, which, in the case of pipe flow, corresponds to the radius R. This method preserves spatial resolution, unlike the previous methods. Considering the definition

of friction Reynolds number Re_τ, the size of the small scales can be linked to the characteristic size of the facility, R:

$$l^* = \frac{R}{Re_\tau}. \tag{3.6}$$

For a fixed outer dimension, increasing the Reynolds number inevitably decreases the size of small scales, leading to poor spatial resolution. This trend can be counterbalanced by increasing the size of the facility to ensure a minimum l^* that can still be measured by traditional methods. Standard single hot-wire probes can be manufactured with a sensing length as short as $120\,\mu m$, up to a maximum of $10l^*$ to avoid spatial averaging. This sets a lower limit to the viscous length scale l^* at $12\,\mu m$. Using eq.3.6 and recalling that the facility needs to reach $Re_\tau \approx 4\times10^4$, we find that the radius of the Long Pipe should be $0.48\,m$.

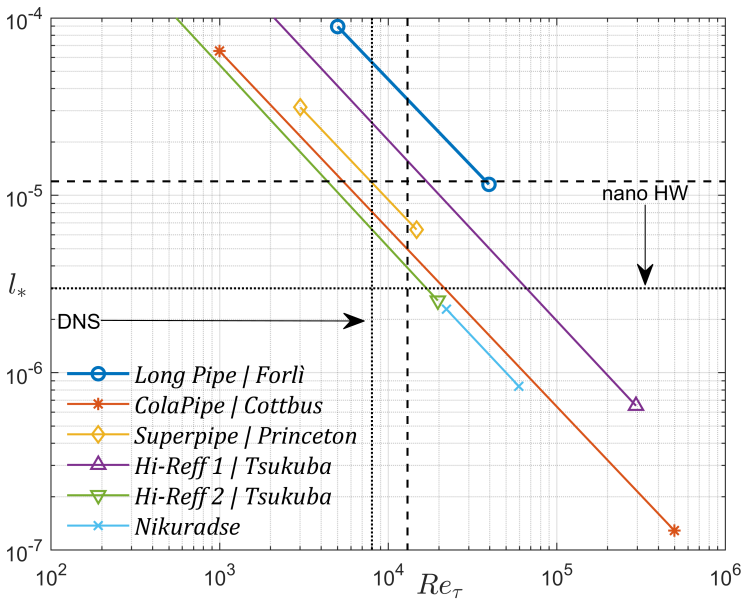

Fig. 3.1 Range of Reynolds numbers vs. viscous length scales for different pipe flow experiments. The vertical dashed line marks the lower bound of the high-Reynolds number region ($Re_\tau \approx 13,300$). The horizontal dashed line represents the $l^* > 10\,\mu m$ limit for sufficient spatial resolution. CICLoPE operates within this region. The vertical dotted line indicates the highest DNS of pipe flow ($Re_\tau = 6000$, Pirozzoli et al. (2021)), and the horizontal dotted line marks the fully resolved measurements using NSTAP sensors ($30\,\mu m$, Bailey et al. (2010)).

The pipe's radius is also subject to another constraint: the length-to-diameter ratio (L/D), a key feature in pipe flow experiments. According to Zagarola et al. (1996), this parameter depends on two conditions: the length the boundary layer needs to grow to reach the center

of the pipe and the length required for turbulence to fully develop. Both lengths increase with Reynolds number. Zagarola et al. (1996) determined that a length of $100D$ (about 100 meters) is necessary to satisfy both conditions in the investigated regimes. Fig. 3.1 illustrates the need for a large-scale experiment like CICLoPE to reach high Reynolds numbers without lowering fluid viscosity.

3.1.2 Wind tunnel layout

The requirements discussed in the previous section led to the design of the Long Pipe. This facility consists of a closed-loop wind tunnel, with a test section that is a 111.5 m-long circular pipe. The facility is housed within one of the two 130 m underground tunnels at the former Industrie Caproni, one of Italy's leading aircraft manufacturers from 1930 to 1943, located in Predappio. These tunnels were excavated beneath the mountains before World War II to allow aircraft assembly during bombing raids. The closed-loop design ensures stable flow conditions with low turbulence levels. It includes a heat exchanger to maintain temperature control within a range of $\pm 0.1^{\circ}C$ and a flow-conditioning system comprising honeycomb structures, four screens, a settling chamber and a convergence with a contraction ratio of $CR = 4$ the maximum achievable within the dimensional constraints of the site. Figures 3.3 and 3.4 provide a schematic of the wind tunnel, outlining its key components.

The primary component of the flow loop, responsible for 60% of the total pressure losses, is a round pipe of constant cross-section. Figure 3.2 illustrates key details of this pipe. It measures 111.5 m in length with an inner diameter of 900 mm, resulting in a L/D ratio of approximately 123. The pipe is constructed from twenty-two 5 m long carbon-fiber sections, plus a final 1.5 m long section, all produced using filament-winding technology. This method achieves a surface roughness of $k_{rms} < 0.2$ μm ($k^+ < 0.02$) and a diameter tolerance of 900 ± 0.2 mm. Each pipe section is fitted with four axially spaced static pressure taps and four radially distributed access ports of 150 mm in diameter, providing access to the pipe. The aluminum access ports are machined to sit flush with the inner surface of the pipe, as shown in Fig.3.2d.

The test section connects to the return circuit located one floor below through a removable shape converter and a series of diffusers and corners. Uniquely, this wind tunnel features six corners (instead of the typical four) to allow the return duct to run beneath the main laboratory floor, providing access for vehicles, before rising above the main tunnel floor via two expanding corners placed before the heat exchanger. The circuit comprises four rectangular expanding corners and two non-expanding circular corners, all equipped with turning vanes. The fan system is designed to provide a pressure rise of 6500 Pa at a volume flow rate of 38 m^3/s, corresponding to a velocity of 60 m/s in the test section. It consists

Fig. 3.2 Elements of the Long pipe facility: a) Heat exchanger and return circuit of the Long Pipe. (b) Settling chamber, Honeycomb, screens and contraction at the inlet on the Long Pipe c) View of the pipe. c) Opening at the final pipe section of 1.5 m along with the diffuser and shape converter placed downstream the Long Pipe.

of two, two-stage counter-rotating axial fans mounted in series. Each axial fan has two propellers on a shared motor, powered by a dedicated inverter. The fan diameter is 1.8 m, with a total length of 4.2 m, and the system's maximum power consumption is 340 kW. For noise reduction, straight cylindrical sections 20 m upstream and downstream of the fans are lined with sound-absorbing material. Temperature and humidity are controlled separately for the main tunnel and the laboratory housing the smaller 1.5 m section, using two external air conditioning systems. Both the wind tunnel airflow and the fan motors are liquid-cooled via a refrigerating circuit connected to an evaporative tower outside the facility.

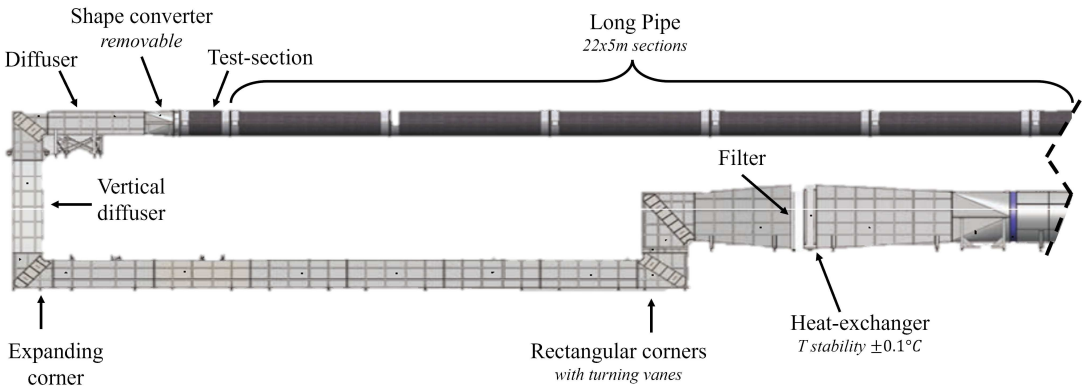

Fig. 3.3 Schematic view of the "Long Pipe".

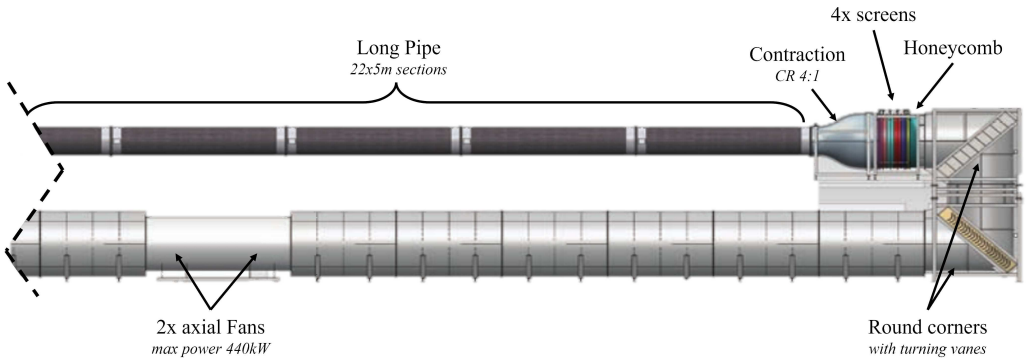

Fig. 3.4 Schematic view of the "Long Pipe".

3.2 Hot wire anemometry

Hot-wire anemometry (HWA) remains one of the most widely used techniques for velocity measurements in turbulence research, even many years after its initial introduction by King (1914). The enduring popularity of HWA is largely due to its exceptional performance in terms of spatial and temporal resolution, while being significantly less expensive than optical measurement techniques. However, its disadvantages include the intrusive nature of the measurement and the fact that a single wire sensor can only measure one velocity component at a point. The fundamental principle behind HWA is that a heated wire experiences a cooling effect due to the flow. This cooling is mainly driven by forced convection, which is highly dependent on the flow velocity. If this heat loss can be accurately quantified, it is possible to determine the flow velocity through calibration, based on the cooling rate of the wire. Unlike pressure-based systems such as Pitot or Prandtl tubes, the cooling effect in HWA occurs rapidly due to the small size of the sensing element, providing a very high frequency response.

Modern hot-wire systems typically operate in constant temperature mode (CTA), where the anemometer maintains the wire at a constant temperature and measures the electrical current required to do so. This section will provide a general overview of HWA and its main features. For more detailed information, readers are directed to the extensive literature on the subject, including works by Bruun (1996) and Tropea et al. (2007). An analysis of heat generation and transfer in a hot-wire follows. In the most general case of an unsteady wire temperature T_w, the heat balance can be written as:

$$m_w c_w \frac{dT_w}{dt} = W - Q. \tag{3.7}$$

The left-hand side represents the rate of change in the thermal energy stored in the wire, where T_w is the wire's temperature, m_w is its mass, and c_w is the specific heat of the wire's material. On the right-hand side, W is the thermal power supplied to the wire, and Q represents the heat lost from the wire. In hot-wire anemometry, the heating is provided by the Joule effect: a current I_w is passed through a wire with resistance R_w:

$$W = I_w^2 R_w. \tag{3.8}$$

Neglecting other forms of heat loss, the heat loss per second due to forced convection (the dominant mechanism in most flow conditions) is given by:

$$Q = (T_w - T_a) A h(U), \tag{3.9}$$

where T_a is the fluid temperature in contact with the wire, A is the surface area of the wire, and $h(U)$ is the heat transfer coefficient, which depends on the flow velocity U. For steady-state conditions ($T_w \approx$ const), as is the case in CTA operation, equation 3.7 becomes:

$$I_w^2 R_w = (T_w - T_a) A h(U). \tag{3.10}$$

For metals, R_w can be expressed as a function of T_w using a linear approximation around a reference temperature T_0:

$$R_w = R_0[1 + \alpha_0(T_w - T_0)], \tag{3.11}$$

where R_0 is the resistance at T_0, and α_0 is the resistivity coefficient of the wire material. For metals, α_0 is positive, meaning resistance increases with temperature. If we take the ambient temperature T_a as the reference, we can derive:

$$T_w - T_a = \frac{R_w - R_a}{\alpha_0 R_a}. \tag{3.12}$$

For a cylindrical body, the forced convection coefficient h can be expressed as:

$$h = \frac{\mathrm{Nu} k_f}{d_w}, \tag{3.13}$$

where k_f is the thermal conductivity of the fluid, d_w is the diameter of the wire, and Nu is the Nusselt number. In subsonic flow, neglecting natural convection:

$$\mathrm{Nu} = \mathrm{Nu}(Re_w, \frac{T_w - T_a}{T_a}), \tag{3.14}$$

where Re_w is the Reynolds number based on wire diameter d_w. Typically, $2 < Re_w < 40$ in hot-wire measurements, which is before vortex shedding occurs. A common correlation for the Nusselt number is:

$$\mathrm{Nu} = A_1 + B_1 Re_w^n, \tag{3.15}$$

where A_1, B_1, and n (often taken as 0.5) are constants. For a given wire diameter, Re_w depends only on velocity U, and we can rewrite:

$$\mathrm{Nu} = A_2 + B_2 U^n. \tag{3.16}$$

Combining equations 3.10, 3.12, and 3.16, we obtain King's law:

$$\frac{I_w^2 R_w}{R_w - R_a} = A + B U^n. \tag{3.17}$$

Introducing the voltage across the hot-wire $E_w = I_w R_w$, and using relation 3.12, equation 3.17 becomes:

$$\frac{E_w^2}{R_w} = (A + BU^n)(T_w - T_a). \tag{3.18}$$

In CTA mode, where T_w and T_a are constant, both R_w and $T_w - T_a$ are constants and can be absorbed into A and B, yielding:

$$E_w^2 = A + BU^n. \tag{3.19}$$

This expression 3.19 can be fitted to calibration data to determine the values of A, B, and n.

3.2.1 Hot-wire limitations

Although hot-wires offer excellent spatial resolution, in wall-bounded flows at higher Reynolds numbers, the smallest turbulent structures can be smaller than the size of the sensing element. This limits the sensor's ability to capture all velocity fluctuations, as illustrated in Fig.3.5, where the wire is unable to resolve the smaller velocity variations.

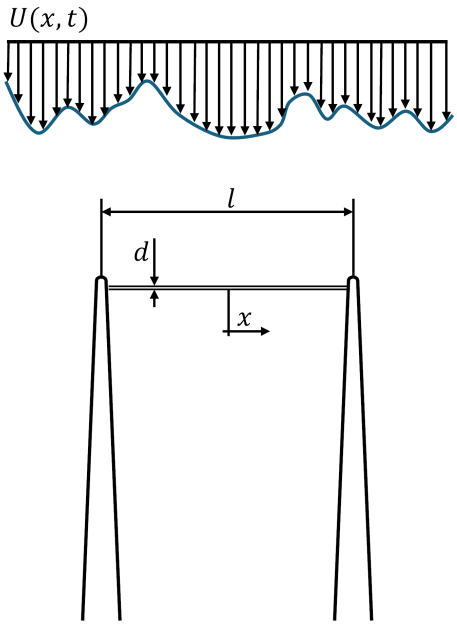

Fig. 3.5 A hot-wire sensor with a non-uniform istantaneous incident velocity$U(x,t)$

Assuming that the cooling is caused exclusively by forced convection due to the normal velocity component U, and neglecting contributions from tangential and bi-normal velocity components, the effective cooling velocity sensed by the wire is approximately the normal component, i.e., $U_{\text{eff}} \approx U$. If the normal velocity distribution along the wire varies, the instantaneous velocity reading will represent a form of spatial averaging over the wire's

length. However, this is not a true spatial average because the heat transfer is not linearly dependent on the effective velocity. Using King's law as an example:

$$\dot{Q} \propto A + BU^n. \tag{3.20}$$

The "filtered" instantaneous velocity reading then becomes:

$$u_m(t) = \left(\frac{1}{L} \int_{-L/2}^{L/2} U^n(s,t) ds \right)^{1/n}, \tag{3.21}$$

where L is the wire's length, and s is the position along the wire, with the origin at the midpoint. The term n accounts for the non-linear relationship between the heat transfer and velocity. The primary impact on the measured quantities is an attenuation of the observed velocity variance. Wyngaard (1968) explored how incomplete spatial resolution affects velocity spectra using the local isotropy assumption. Many experimental studies focus on wall-bounded flows, where spatial resolution limitations are most prominent. Ligrani and Bradshaw (1987) studied the impact of wire length on velocity statistics in the near-wall region of a boundary layer, identifying the wire's length in viscous units, $L^+ = L/l^*$, as a key parameter in spatial filtering. More recent studies, such as those by Hutchins et al. (2009), have also examined this issue. Segalini et al. (2011),Monkewitz et al. (2010), and Smits et al. (2011a) proposed different correction methods for addressing spatial resolution errors.

From previous considerations on spatial resolution, one might assume that using a shorter wire would improve measurements. However, this is not always the case, as there are limitations on the minimum allowable wire length. Not all the heat is transferred from the wire by forced convection. While radiation heat transfer is typically negligible, and natural convection becomes significant only at very low velocities, a portion of the heat is transferred from the wire to its support via conduction. This is an undesirable side effect that should be minimized. The heat transfer due to forced convection is proportional to the surface area of the wire exposed to the flow, i.e.,

$$Q_{fc} \propto \pi r_w^2 L, \tag{3.22}$$

where r_w is the radius of the wire and L its length. On the other hand, the conduction heat transfer is proportional to the cross-sectional area of the wire:

$$Q_c \propto \pi r_w^2. \tag{3.23}$$

Thus, the ratio between forced convection and conduction scales as L/d_w, where d_w is the wire diameter. Ligrani and Bradshaw (1987) also examined the effect of the wire's aspect ratio on measured turbulence intensity. Their findings indicated that an aspect ratio of

$$\frac{L}{d} > 200; \tag{3.24}$$

is required to avoid attenuation effects.

3.2.2 Hot-wire calibration

Hot-wire velocity calibration is conducted ex-situ in a planar jet facility, covering a velocity range of 0.5 – 50 m/s. During the calibration process, the hot-wire voltage E, flow velocity U, and flow temperature T are recorded for each calibration point. The flow velocity is measured using a Pitot tube placed in the jet core near the hot-wire sensor, while the jet temperature is obtained via a PT100 thermistor. A reference calibration temperature, T_{ref}, is calculated as the average temperature of all calibration points. The voltage for each calibration point is then corrected with respect to its mean temperature T_i, using the expression from Bruun (1996):

$$E(T_{\text{ref}}) = E(T_i)\left(1 - \frac{T_i - T_{\text{ref}}}{a_w/\alpha_{\text{el}}}\right)^{-\frac{1}{2}} \tag{3.25}$$

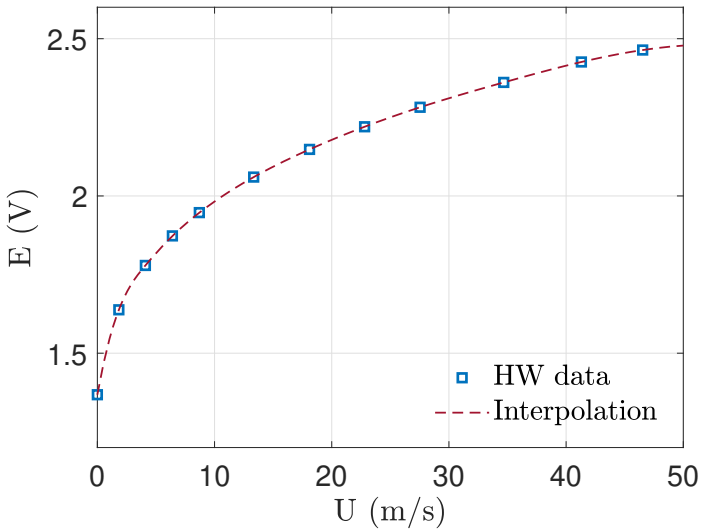

Fig. 3.6 Calibration curve for a single wire probe, blue square refers to HW data points while dashed red curve highlights the interpolation curve using a 4^{th}-order polynomial

For single-wire probes, the calibration procedure involves acquiring around 15 calibration points across the velocity range of the wind tunnel. A calibration curve is fitted to the data points using a fourth-order polynomial:

$$U = C_0 + C_1 E + C_2 E^2 + C_3 E^3 + C_4 E^4 \tag{3.26}$$

Here, C_0 to C_4 are coefficients obtained via least squares fitting. An example calibration curve for a single-wire sensor is shown in Fig.3.6 where dashed red line highlights the polynomial interpolation curve while blue square depicts the HW acquired throughout the calibration procedure.

3.2.3 X-wire calibration

Typically, two-wire probe are calibrated ex-situ in a planar jet wind tunnel (PAT) that allows multiple x-wire calibration at a time. The probe is subjected to a series of controlled airflow condition varying both flow speed and angle relative to the wire orientation (Burattini and Antonia, 2004). Fig.3.7 shows a typical calibration map of an X-wire where blue empty square refers to the data acquired during the calibration procedure. In addition to the voltage of the two wires (E_1, E_2), obtained as a mean quantity over an acquisition time, velocity is measured by means of a pitot probe. Temperature is also monitored to account for voltage drift during the procedures using PT100 thermistor. The probe is then shifted at different angles using a stepper motor.

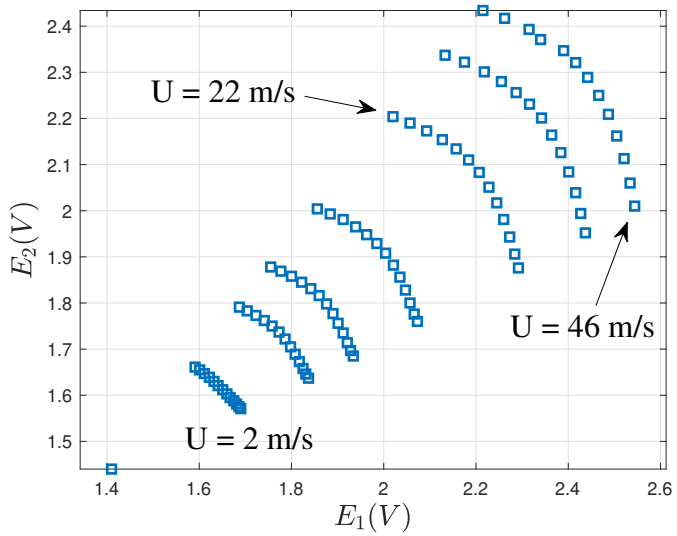

Fig. 3.7 Calibration curve for a two-wire probe, blue square refers to XW-data points at different velocity values

The look-up-table calibration was conducted by systematically exposing the x-wire probe to a range of precisely controlled flow conditions. Specifically, eight different flow velocities were tested to cover the entire operational range expected in the experiment, ensuring that the calibration captures the probe's response across various flow intensities. Alongside each velocity setting, the probe was also subjected to 13 distinct flow angles, varying incrementally up to ±27°, to account for any directional dependence in the probe's voltage response.

For each combination of velocity and angle, the voltages from both wires in the x-wire probe were recorded. These voltages were then associated with their respective flow velocities and angles, forming a comprehensive two-dimensional look-up table. This table effectively maps the relationship between the probe's voltage signals and the actual flow conditions. This meticulous calibration setup allows for interpolation during actual measurements, enabling accurate calculation of streamwise and wall-normal velocity components based on the measured voltages. The inclusion of multiple velocities and angles up to ±27° ensures that the look-up table is robust and capable of handling complex flow dynamics. Fig. 3.8 shows the two calibration maps created to convert voltages combinations of wire 1 and 2 into velocity components, in our case, u and v.

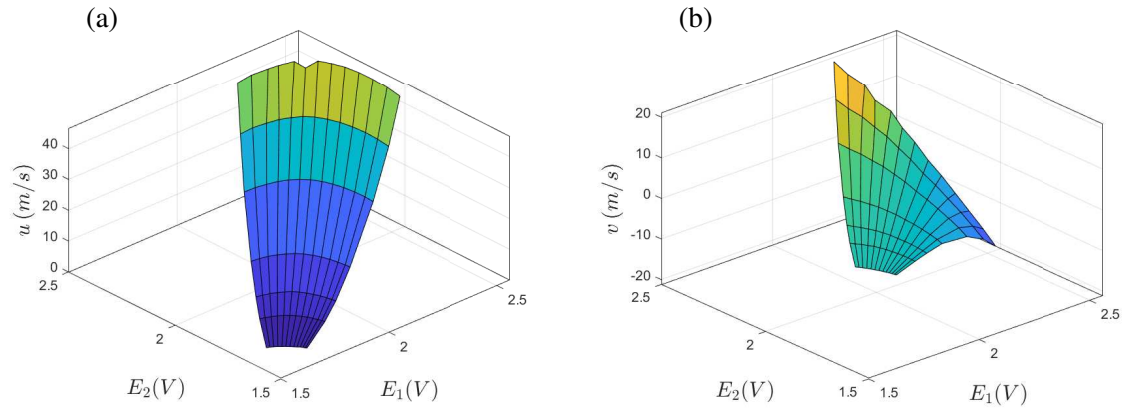

Fig. 3.8 Contour plots of the velocity components for the X-wire calibration procedure. (a) u component; (b) v component.

To evaluate the effectiveness of the x-wire calibration, power spectral density (PSD) measurements of the streamwise velocity were compared against those obtained from a calibrated hot-wire probe placed at the same location in the flow. The PSD serves as a diagnostic tool to assess the accuracy and reliability of the x-wire in capturing velocity fluctuations across various frequencies. By comparing the spectral content from both probes, it was possible to determine if the x-wire accurately reproduced the turbulent energy distribution and flow characteristics at that point. Agreement between the PSD profiles of the x-wire and hot-wire

would confirm that the x-wire's look-up table calibration effectively captured the true velocity components, validating the probe's calibration over a broad range of frequencies relevant to turbulent flow studies as can be seen in Fig.3.9 where PSD of the X-wire is reported showing u component of the velocity in orange and v component of the flow velocity in blue. Yellow curve reports data obtained from single wire measurements at the same wall-normal distance in the Long Pipe.

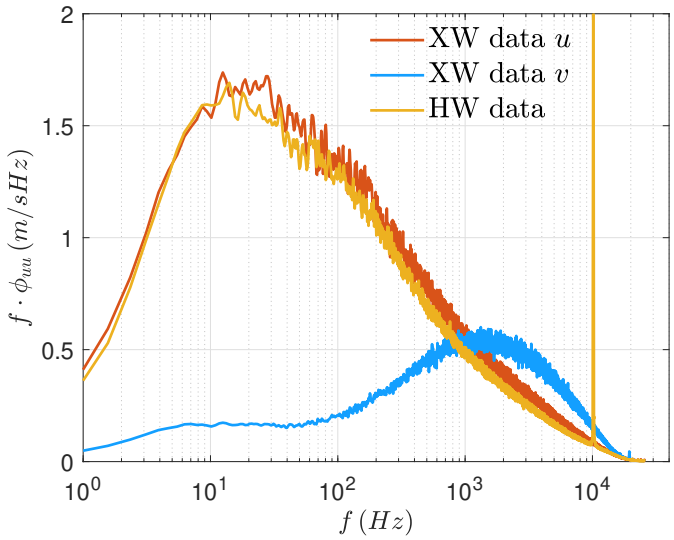

Fig. 3.9 Pre-multiplied power spectral densities of X-wire data, Orange line refers to u component of the velocity, blu line refers to v component of the velocity. Yellow line depicts the single wire data obtained in the same location of the 2-wire probe.

3.3 Pressure measurements

Measuring steady pressure in fluid flow can be essential for determining thermodynamic properties, calculating forces on a body from the pressure distribution, or determining dynamic head and flow velocity. Pressure represents molecular activity and reflects the non-directional motions of molecules, meaning it must, by definition, be measured by a device stationary relative to the flow. Although it is customary in fluid mechanics to denote this as 'static' pressure, this terminology is inherently redundant. In practical applications, pressure is commonly measured both at wall surfaces and in the free-stream using the types of measurement devices shown in Fig.3.10 which are connected to a transducer with appropriate sensitivity and range. A small wall tapping orifice provides a straightforward method to capture the pressure exerted on the wall by the external flow. Similarly, 'static

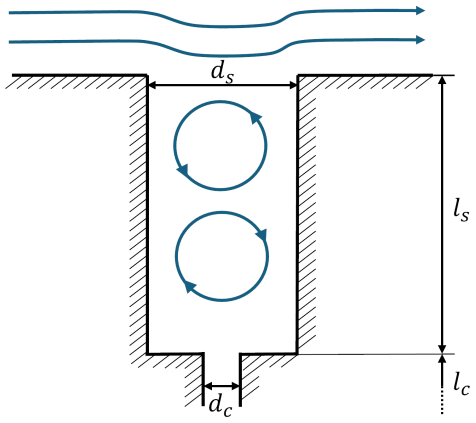

Fig. 3.10 Schematic view of the wall tapping technique.

pressure' tubes can approximate the local pressure in the free-stream, provided that any disturbance they introduce to the flow can either be corrected for or remains minimal.

3.3.1 Measurement of pressure with Wall Tappings

A wall tapping, or piezometer, provides a straightforward method for measuring the wall pressure, p_w, in a wall-bounded flow. However, it requires careful consideration in many flows. The finite size of tappings that can be manufactured with smoothness and reliability may be large enough to introduce an error, resulting in a measured pressure $p_{wm} = p_w + \Delta p_w$. Dimensional analysis shows that for a pressure tapping of a given geometry in a zero-pressure-gradient flow (or where the tapping diameter is small relative to the pressure variation scale), the non-dimensionalized pressure error, $\Pi = \frac{\Delta p}{\tau_w}$, depends on the following parameters:

$$\Pi = f\left(\frac{d_s u_\tau}{\nu}, \frac{d_s}{D}, M, \frac{l_s}{d_s}, \frac{d_c}{d_s}\right), \tag{3.27}$$

where each variable corresponds to flow and geometry characteristics. Additionally, the wall-bounded flow condition (whether laminar or turbulent) affects the pressure measurement. Here, d_s is the tapping (orifice) diameter, $u_\tau = \sqrt{\tau_w/\rho}$ is the friction velocity, D is the characteristic flow length scale, M is the Mach number (the ratio of local velocity to the speed of sound), l_s is the orifice depth, d_c is the diameter of the cavity behind the orifice, η is the root-mean-square height of burrs on the tapping orifice edge, ρ is the fluid density, and ν is the kinematic viscosity (Fig. 3.10). The actual wall pressure, p_w, can be found using

$$p_w = p_{mw} - \Pi \tau_w. \tag{3.28}$$

The complex flow near the tapping makes it challenging to obtain analytical or numerical solutions for the pressure error, which are currently available only for very low Reynolds numbers and/or two-dimensional geometries. Most experimental data pertains to turbulent flow over the orifice, and comparisons of experiments show considerable scatter in results. This variation likely arises from the inherent difficulty of these experiments (with pressure errors close to the experimental uncertainty) and the challenges in accurately extrapolating the true pressure to quantify the error.

Researchers have explored various orifice shapes beyond the traditional straight-edged, circular cylinder, which is drilled perpendicularly to the wall. Alternatives include slot-type, angled, and radiused or chamfered-edge circular tappings, with varying connector geometries between the tapping and transducer to accommodate experimental constraints or manufacturing techniques. Although these designs aim to reduce pressure error, findings—such as those by Allen and Hooper, who examined geometries like recessed and countersunk orifices—indicate trends but remain inconclusive on a universal standard for minimizing errors. Differences between cylindrical and slot-type tappings at supersonic speeds, as reported by Chue (1975), demonstrate about ±1% variation in measured pressure, highlighting correction needs for out-of-round tappings.

Tapping alignment and shape also play significant roles in measurement accuracy. For example, Rayle (1949) studies show minimal error when the tapping centerline is angled 30° downstream relative to the outward wall normal, with deviations as the angle shifts upstream or downstream. Surface curvature around the tapping, especially when the ratio of orifice diameter to curvature radius approaches unity, influences results and suggests that flat and curved surfaces may require different scaling laws. Additionally, below-surface geometry, such as the ratio of orifice diameter to cavity diameter, affects results, as shown in comparisons between Livesey et al. (1962) and Shaw (1960) experimental designs. Given the variability associated with non-standard geometries, in situ calibration across the expected flow conditions is recommended to ensure reliable wall pressure measurements.

3.3.2 Effect of cavity dimension

For deep tappings with smooth edges, the finite diameter induces local curvature of streamlines and vortex formation within the cavity, which affects the measured static pressure. The error in pressure measurement, Π, depends on both the ratios $d_s^+ = d_s u_\tau / \nu$ (tapping diameter to viscous scale) and d_s/D (tapping diameter to flow lengthscale), expressed as

$$\Pi = f(d_s^+, d_s/D) \tag{3.29}$$

(see Eq.(3.29)). However, accurately measuring Π is challenging due to small pressure differences, sensitivity to manufacturing variations, and the need to isolate individual parameters like d_s^+ and d_s/D. Studies by Ray (1956), Franklin and Wallace (1970), and others have examined the static hole error in boundary layers and channels, but variations in tapping geometries lead to scattered results. Shaw's experiments in pipes, often considered a standard for deep hole tappings, demonstrated that for small d_s/D and d_s^+ in the range of 25–800, pressure error varies with diameter. McKeon and Smits (2002) extended Shaw (1960) work across higher Reynolds numbers, finding that pressure error depends on tapping Reynolds number alone at low d_s^+, while d_s/D becomes increasingly influential as d_s^+ rises. Livesey et al. (1962) model, based on streamline deflection, yielded curves similar to McKeon and Smits' data, shown in Fig. 4.2 (reprinted). For larger tappings and high tapping Reynolds numbers, pressure error is better represented by the pressure coefficient

$$C_{ps} = \frac{\Delta p}{\frac{1}{2}\rho U^2} \tag{3.30}$$

as a function of d_s/D. This is especially relevant in compressible, high-Reynolds-number flows, where smooth, small tappings are challenging to manufacture.

In summary, pressure measurement error for tappings in turbulent flow increases with d_s^+ for a given d_s/D and decreases as d_s/D grows for a given d_s^+. This error averages out in steady internal flows but may impact boundary layer pressure gradients significantly. For large tappings in laminar flow, as Rainbird (1967) noted, the error does not asymptote at high Reynolds numbers and can reach $O(50)$. Additionally, large tappings in regions of rapid pressure variation may introduce spatial averaging errors, especially if the tapping is larger than the characteristic pressure variation length-scale. For more details about pressure measurements, the reader is redirected to Tropea et al. (2007).

3.4 Static pressure drop

In the Long Pipe facility, the wall shear stress τ_w is measured indirectly via static pressure drop along the pipe. For a pipe flow, the equilibrium forces acting on a volume of fluid contained ina pipe section of length dx is:

$$dp\pi R^2 = \tau_w 2\pi R dx, \tag{3.31}$$

which leads to:

$$\tau_w = \frac{dp}{dx}\frac{R}{2}. \tag{3.32}$$

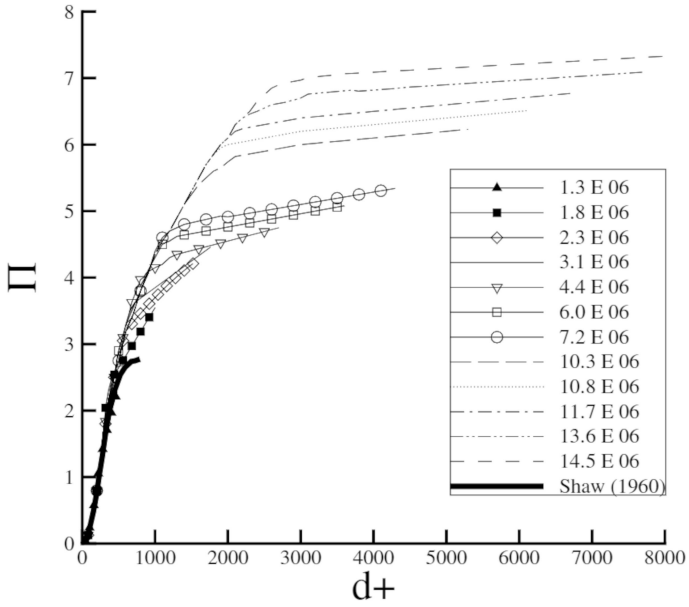

Fig. 3.11 Variation of non-dimensional pressure error, Π, for different pipe Reynolds number Re_D, reprinted from McKeon and Smits (2002)

The pressure gradient directly links to the wall friction, allowing the calculation of the friction velocity $u_\tau = \sqrt{\tau_w/\rho}$, which, according to classical wall-turbulence theory, serves as the relevant velocity scale in both the inner and outer regions of the flow. Accurately estimating the pressure drop is crucial for obtaining precise normalized flow statistics, as shown by Örlü et al. (2010), where an error in u_τ significantly impacts the inner-scaled mean velocity profile.

Static pressure measurements are taken along the pipe, spanning approximately 70 meters upstream from the test section, using 1 mm diameter wall pressure taps. These measurements are performed across different flow regimes by adjusting the rotational speed of the two axial fans. Meanwhile, the centerline velocity U_{cl}, ambient pressure p_{amb}, and temperature are monitored within the test section.

3.5 Oil Film Interferometry (OFI)

Wall shear stress, as expressed before, represents a key quantity that needs to be carefully measured in wall bounded turbulent flows. Although the pressure drop represents a solid solution for every flow condition, it suffers at low Re_τ due to small differences between ambient pressure and static pressure inside the pipe and gives us a "global" quantity related to the entire pipe section considered. Within this, Oil Film Interferometry (OFI) represents

a robust alternative to wall shear stress measurements. To make measurements using OFI techniques, oil is applied to the body. As fluid passes over the model or the considered surface, the oil thins as shown in Fig.3.12. To quantify the thinning rate of the oil, the oil thickness h is measured, normally via interferometry. With a measurement of the oil thickness at one or more instants in time, the local skin friction may be computed using a form of the thin-oil-film equation.

Squire (1961) and Tanner and Blows (1976) where among the first to investigate the possibility of using OFI in turbulence research aiming at measuring skin friction. Although the oil moves under the effects of many parameters, the dominant contribution is caused by tangential stress at the wall. Under this hypothesis, it is possible to link the evolution of oil thickness, h_{oil}, to wall shear stress, τ_w, taking advantage of the thin oil film equation:

$$\frac{\partial h_{oil}}{\partial t} + \frac{\partial}{\partial x}\left(\frac{\tau_w h_{oil}^2}{2\mu_{oil}}\right) = 0, \tag{3.33}$$

Being that the flow develops mainly in one direction, we can neglect the $v\,and\,w$ component of the flow velocity and so consider that the oil film is mono-dimensional and aligned with the direction of the flow. oil drop deformation will be a function of time and of only one space component. we can integrate (3.33) through h_{oil} obtaining:

$$h_{oil} = \frac{\mu_{oil}}{\tau_w}\frac{x}{t} \Rightarrow \frac{\partial h_{oil}}{\partial x} = \frac{\mu_{oil}}{t \cdot \tau_w} \tag{3.34}$$

As indicated above, the oil-film thickness h is required to determine the surface shear-stress. Fig.3.12 shows how amplitude slitting, or Fizeau, interferometry works in this application. The light of wavelength λ emitted from a source strikes the film at an angle θ_i and a part is reflected from the oil/air surface. Another part of that light will be refracted into the film, and as it reaches the solid surface it will be reflected away travelling back through the oil film. When focused by a lens, these two beams are combined together and interfere constructively or destructively with each other depending on the phase difference ϕ between them as they reached the oil surface.

Figure3.13 helps us to calculate the optical path difference (OPD) between two different reflected waves. It corresponds to segment $\overline{CD}$ in Fig.3.13. From the geometry, we can observe:

$$\overline{AB} = \overline{BC} = \frac{h_{oil}}{\cos\Omega_2}; \tag{3.35}$$

while $\overline{AC} = 2 \cdot h_{oil} \cdot \tan\Omega_2$ we will have:

$$\overline{AD} = 2 \cdot h_{oil} \cdot \tan\Omega_2 \cdot \sin\Omega_1. \tag{3.36}$$

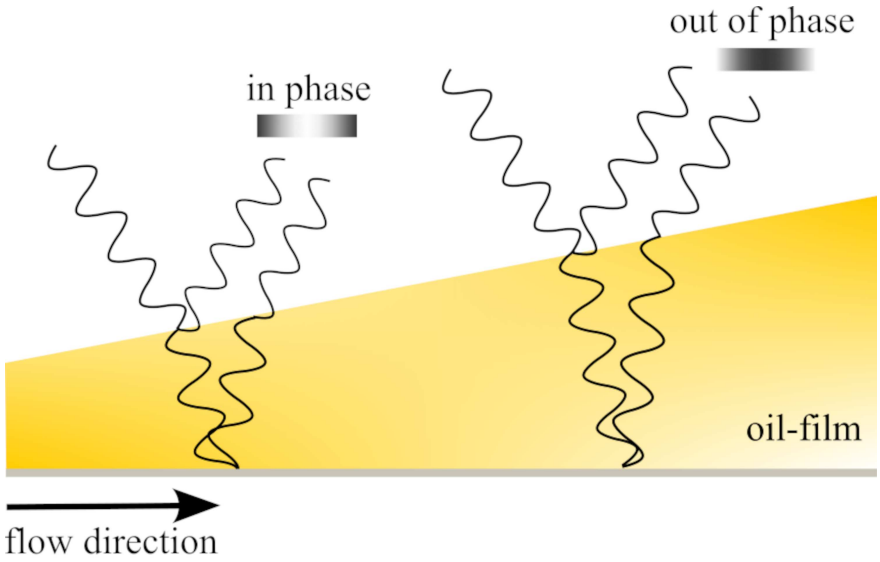

Fig. 3.12 interference fringes produced by Fizeau Interferometry: first light source produces constructive interference resulting in bright bands, whereas second light source produces destructive interference and dark bands.

Being:

$$OPD = \left(\overline{AB} + \overline{BC}\right) \cdot n_{oil} - \overline{AD} \cdot n_{air}, \tag{3.37}$$

then:

$$OPD = n_{\text{oil}} \left(\frac{2 \cdot h_{\text{oil}}}{\cos(\Omega_2)}\right) - 2 \cdot h_{\text{oil}} \cdot \tan(\Omega_2) \cdot \sin(\Omega_1) \cdot n_{\text{air}}. \tag{3.38}$$

From Snell law (Hecht, 2002) $(n_{air} \cdot \sin\Omega_1) = (n_{oil} \cdot \sin\Omega_2)$ we will have:

$$OPD = n_{\text{oil}} \left(\frac{2 \cdot h_{\text{oil}}}{\cos(\Omega_2)}\right) - 2 \cdot h_{\text{oil}} \cdot \tan(\Omega_2) \cdot h_{\text{oil}} \cdot \sin(\Omega_2) \cdot n_{\text{oil}}. \tag{3.39}$$

which will get us to:

$$OPD = 2 \cdot n_{\text{oil}} \cdot h_{\text{oil}} \cdot \left(\frac{1 - \sin^2(\Omega_2)}{\cos(\Omega_2)}\right). \tag{3.40}$$

In conclusion:

$$OPD = 2 \cdot n_{oil} \cdot h_{oil} \cdot \cos\Omega_2. \tag{3.41}$$

It is evident that interference is constructive if and only if OPD is a multiple of the wavelength (λ_L) of the light source, hence:

$$OPD = m \cdot \lambda_L \quad m \in \mathbb{N}. \tag{3.42}$$

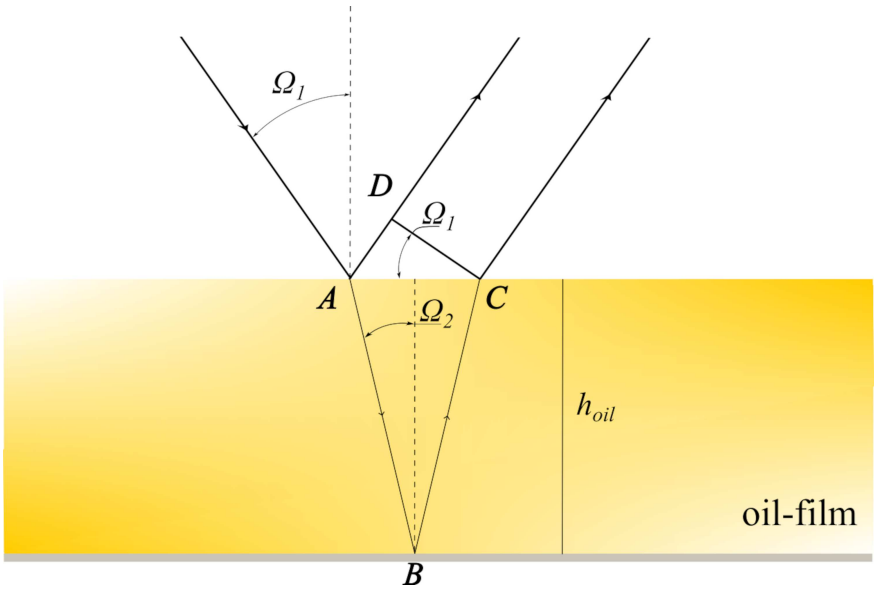

Fig. 3.13 wave reflection in OFI application

The difference in thickness between two successive fringes ($\Delta h_{\text{oil}} = h_{\text{oil2}} - h_{\text{oil1}}$) can be derived from the difference in OPD between two successive fringes:

$$\Delta OPD = 2 \cdot n_{\text{oil}} \cdot (\Delta h_{\text{oil}}) \cdot \cos(\Omega_2) = m \cdot \lambda_L - (m-1) \cdot \lambda_L; \tag{3.43}$$

finally:

$$\Delta h_{\text{oil}} = \frac{\lambda_L}{2 \cdot n_{\text{oil}} \cdot \cos(\Omega_2)}. \tag{3.44}$$

Reformulating, taking into account Snell's law and fundamental trigonometric relationships, we obtain:

$$\Delta h_{\text{oil}} = \frac{\lambda_L}{2 \cdot \sqrt{n_{\text{oil}}^2 - n_{\text{air}}^2 \cdot \sin^2(\Omega_1)}}. \tag{3.45}$$

Formulation 3.45 allows us to calculate the variation in the thickness of the oil film corresponding to two successive white fringes (constructive interference); since (Δh_{oil}) between them is constant over time but (Δx) is not, the drop deforms over time; specifically, as (Δx) increases over time, the film becomes progressively thinner. Having determined the difference in thickness between two successive fringes, we now aim to relate this result to the slope of the oil film, in order to uniquely describe its deformation.

In Fig.3.14, it can be observed that the distance between two successive fringes at a given time (t) is:

$$\Delta x = \Delta h_{\text{oil}} \cdot \tan^{-1} \phi; \tag{3.46}$$

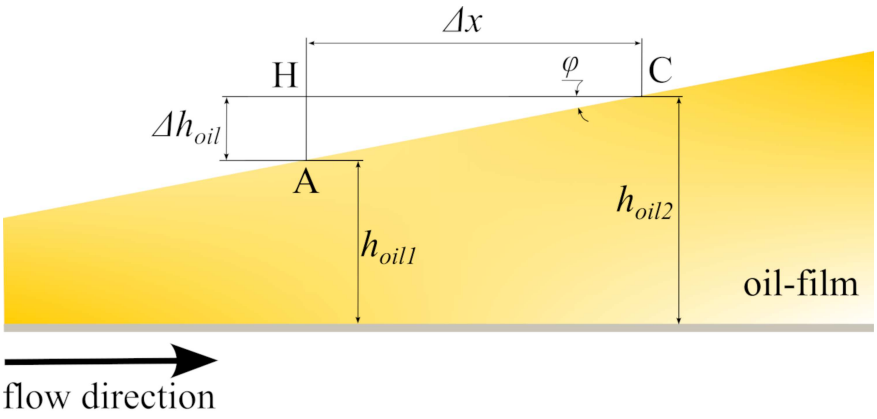

Fig. 3.14 wave reflection in OFI application

it is possible to note that the slope $\tan\phi = \frac{\partial h_{\text{oil}}}{\partial x}$, therefore:

$$\Delta x = \Delta h_{\text{oil}} \cdot \left(\frac{\partial h_{\text{oil}}}{\partial x} \right)^{-1}. \tag{3.47}$$

By combining the various described equations, in particular equation (3.34) with (3.47), we obtain:

$$\Delta x = \Delta h_{\text{oil}} \cdot \frac{\tau_w t}{\mu_{\text{oil}}}, \tag{3.48}$$

and thus:

$$\tau_w = \frac{\mu_{\text{oil}} \Delta x}{\Delta h_{\text{oil}} t}. \tag{3.49}$$

Taking the limit as $(t \to 0)$, we obtain the local (τ_w):

$$\tau_w = \frac{\mu_{\text{oil}}}{\Delta h_{\text{oil}}} \frac{\partial x}{\partial t}. \tag{3.50}$$

In summary, the described method allows us to determine the wall shear stress from the study of oil drop deformation; specifically, it is possible to calculate the aerodynamic friction by measuring the fringe evolution speed $(\frac{\partial x}{\partial t})$ and observing how quickly the distance between them increases. In fact, since the other parameters (μ_{oil} and Δh_{oil}) are known beforehand and remain constant, the wall shear stress is uniquely determined by equation 3.50. To calculate the term $(\frac{\partial x}{\partial t})$, it is sufficient to take (n) photographs at equal time intervals and extract from each one the mean or median distance between successive fringes; an example of photographs taken at different times is shown in Fig. 3.15.

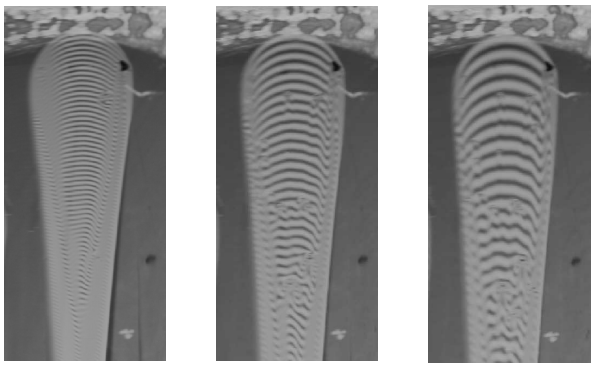

Fig. 3.15 snapshots of the OFI with Fizeau fringes at different instant of time.

3.5.1 OFI processing

Here we briefly present the procedure used while processing the OFI data acquired using a canonical setup that comprises: a Camera, a monochromatic light source and a glass surface with a black background to enhance the reflection of the light into the camera. The process is commonly divided into three main parts: calibration of the experimental setup, acquisition and correction of every acquired image, calculation of τ_w from the set of OFI images.

Calibration of the setup

Accurate calibration is a critical component of the oil film interferometry (OFI) process, as it ensures precise measurements of wall shear stress. The calibration procedure begins with placing a reference grid inside the test section, which is photographed at the start of each measurement. This grid, shown in Figure 3.16, provides a geometric reference with a regular pattern, allowing for the determination of the pixel-to-millimeter conversion factor. The conversion factor is essential for accurately scaling pixel measurements into real-world units, which is crucial for analyzing the dimensions of the fringes generated during oil film experiments.

Once the grid is photographed, the next step involves processing the image to correct any camera inclination or misalignment. Even slight deviations from a perfectly perpendicular view can introduce distortions into the measurement. In Figure 3.17, the left image shows the identification of four key corner points on the grid. These points are used to correct

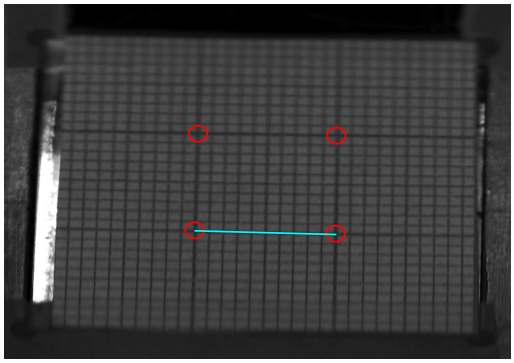

Fig. 3.16 Calibration grid used as a reference, photographed before each measurement to establish a pixel-to-millimeter scale.

the inclination, ensuring that the grid is properly aligned. After this correction, a pixel-to-millimeter conversion factor is calculated, as shown in the right image. This factor is applied in subsequent steps to determine the precise size of the fringes observed in the oil film during experiments.

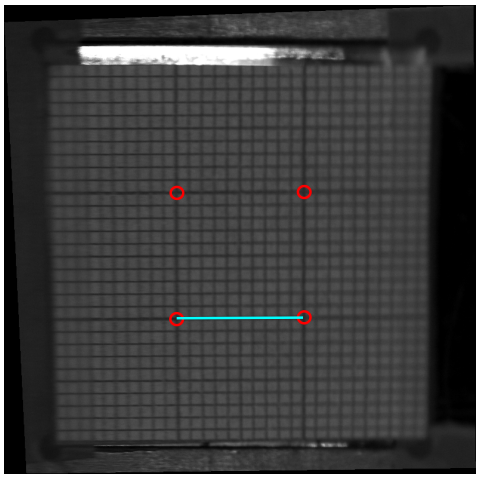

Fig. 3.17 Correction for inclination using four grid points (left), followed by the pixel-to-millimeter factor calculation (right) for accurate fringe size measurement.

The calculated pixel-to-millimeter factor is crucial for determining the exact dimensions of the interferometric fringes. These fringes are directly related to the local wall shear stress, making accurate fringe measurement essential to obtain reliable data from OFI experiments. By establishing a precise calibration setup, the overall accuracy of the shear stress measurements is enhanced, ensuring that the experimental results are valid and reproducible.

Acquisition and correction

It is quite important from now on to keep the setup as fixed as possible, in fact every movement will result in an error caused by the mispositioning of the camera with respect to the oil while converting pixel to metres the acquired images. Every acquired picture will then be re-oriented as it is taken completely orthogonal to the camera. After such a correction, a calibration factor ($\frac{meters}{pixels}$) and a transformation matrix will be obtained. Such packed images will represents the entire dataset for each acquisition.

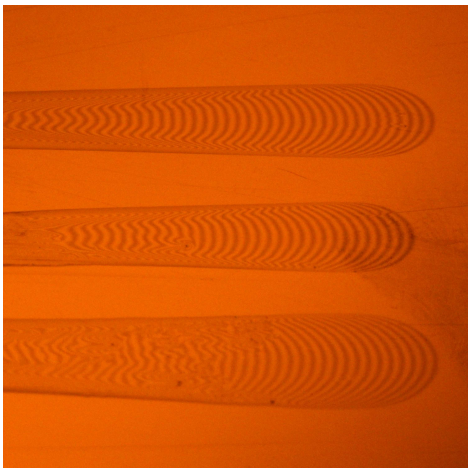

Fig. 3.18 Sample Oil Film snapshot

Since every acquisition corresponds to three different oil drops placed at the bottom of the test section, the data sets will be split into three different parts. Within every images an interrogation area will be selected as Fig.3.19 depicts where (a) highlights the selection of the interrogation area with the red rectangle and (b) shows the cropped image. Figure3.19(b) clearly shows that the interferometry pattern will vary mainly along the longitudinal direction x. Thanks to this it is possible the extraction of a mono-dimensional signal representing the light intensity along x for each acquired image as can be seen in Fig. 3.20.

Once the n signals are obtained, corresponding to the number of frames extrapolated in phase 1, the procedure to calculate the wavelength Δx in meters for each of them is described. It should be recalled that the ultimate goal for estimating aerodynamic friction is to determine the evolution speed of the interferometric fringes $\partial x/\partial t$, i.e., to calculate the temporal variation of Δx between successive fringes. Thus, for each signal, Δx is estimated, and since each signal is associated with a frame at a specific time instant, and given that the time interval Δt between two successive frames is known, it is possible to determine $\Delta x/\Delta t$, which represents the speed of the fringes.

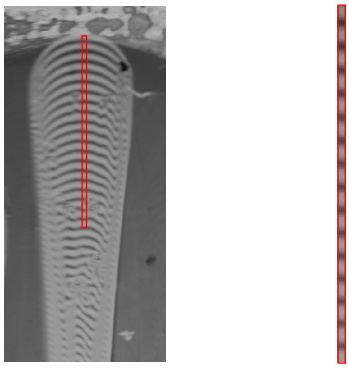

Fig. 3.19 interrogation area selection.

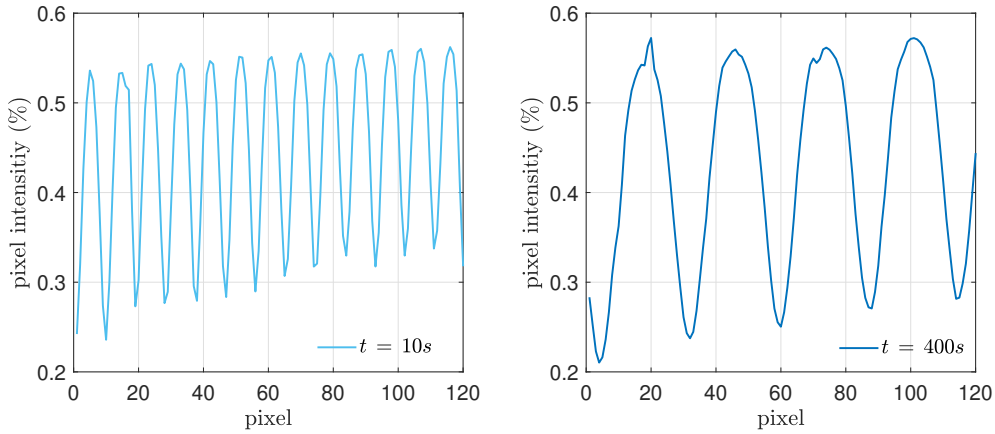

Fig. 3.20 Extrapolated signal after the selection of the interrogation area on the considered oil drop. on the left, the signal extrapolated at $t = 10\,s$; on the right the signal extrapolated at $t = 400\,s$

To calculate the wavelength of a discrete signal, a methodology used by Medici was adapted to our case. This technique allows for identifying the signal peaks (which correspond to the white fringes) and extracting the corresponding maxima, whose difference corresponds to the wavelength. To do this, a threshold is defined as $\overline{S} + 20\% \cdot (y_{max} - y_{min})$, where $\overline{S}$ represents the average value of the signal. If the signal exceeds the threshold while rising and then crosses it again while descending, a peak of the signal, and hence a white fringe, is identified.

To implement this, it is necessary to detect the points of intersection between the signal and the threshold. This is achieved by defining a logical vector that contains a value of 1 at positions x where the signal intensity is greater than the threshold, and 0 elsewhere. By computing the difference between successive elements of the logical vector, a new vector is

obtained. The positions of value 1 in the new vector correspond to the x positions where the signal exceeds the threshold while rising, whereas those with a value of -1 correspond to the x positions where the signal exceeds the threshold while descending. By extracting the indices from this new vector that fall within the interval $[-1, 1]$, the x coordinates corresponding to the various peaks are identified. For better visualization, refer to Fig. 3.20.

As shown in the Fig. 3.20, the first and last crossing points of the threshold define two incomplete fringes. To avoid detecting them, a check is added to the code that excludes these points if they are present. The technique used to do this consists of eliminating the first point if it corresponds to a descending threshold crossing and eliminating the last point if it corresponds to a rising threshold crossing. Since, as shown in the figure, the signal intensity values are sampled at not excessively dense intervals, the described procedure provides intersection points (red points in the figure) that are not exactly centered on the threshold but located around it. This issue can be addressed either by lowering the threshold further (e.g. to $10\% - 15\%$) or by considering the x values of the first points below the threshold as the intersection points.

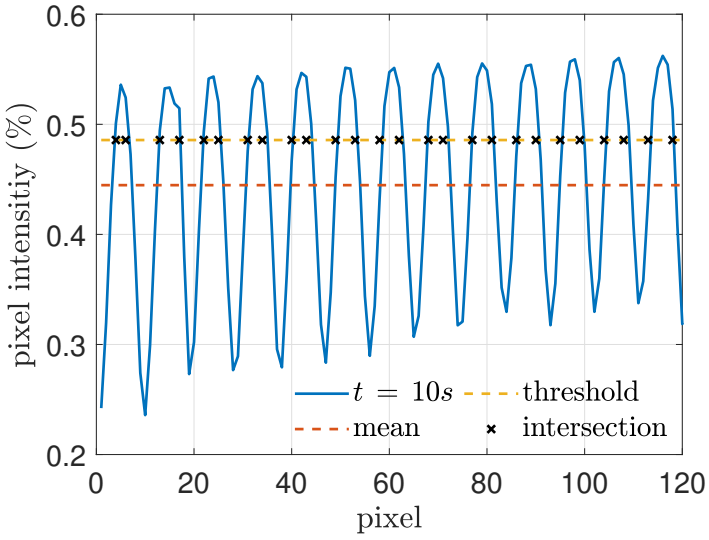

Fig. 3.21 White fringes detection in a generic signal

Once the intervals of the x coordinates corresponding to the white fringes (signal peaks) are detected, the next step is to interpolate the signal values corresponding to each identified peak using a second-degree polynomial. Therefore, for each fringe, a parabola is obtained that interpolates the signal intensity at each crest, as depicted in Fig. 3.22. Since MATLAB returns the coefficients a, b, and c of the second-degree interpolating polynomial, it is

possible to calculate the maximum value corresponding to each parabola by setting the first derivative of the function to zero. This yields:

$$x_{\max} = -\frac{b}{2a} \tag{3.51}$$

By saving the $x_{\max}$ values of each parabola in a vector and evaluating either the median or the average of their differences, the wavelength of the signal in pixels can be obtained. This value can then be easily converted to meters using the calibration factor calculated earlier.

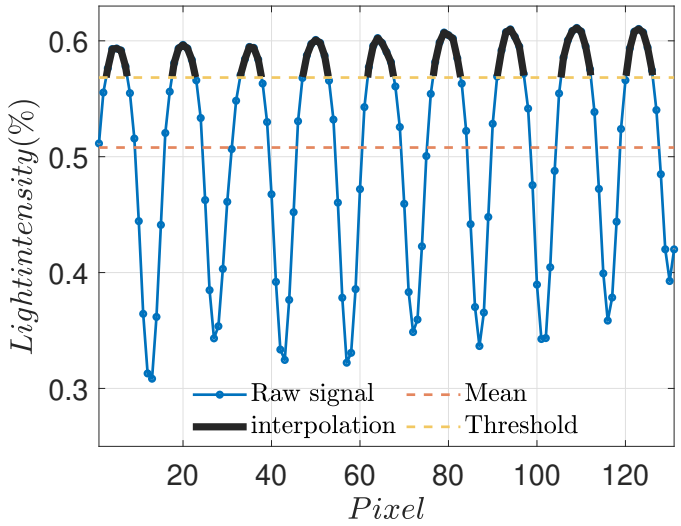

Fig. 3.22 Wavelength calculation on a single snapshot signal, extrapolated from the interrogation area of the considered oil drop.

Wall shear stress calculation

By iterating over each image as described in the previous step, a series of wavelengths Δx is obtained, corresponding to each snapshot in the dataset. With each snapshot linked to a specific, known time, these wavelengths Δx can be plotted as a function of time and their trend linearly interpolated, as illustrated in Fig.3.23. By extracting the slope of the regression line, the term $\frac{\partial x}{\partial t}$ is derived, which in turn allows the calculation of aerodynamic friction. In fact, knowing the oil viscosity μ_{oil} from the oil calibration and Δh_{oil} calculated from Equation 3.45 based on the setup data, the wall shear stress can ultimately be calculated using Equation 3.50.

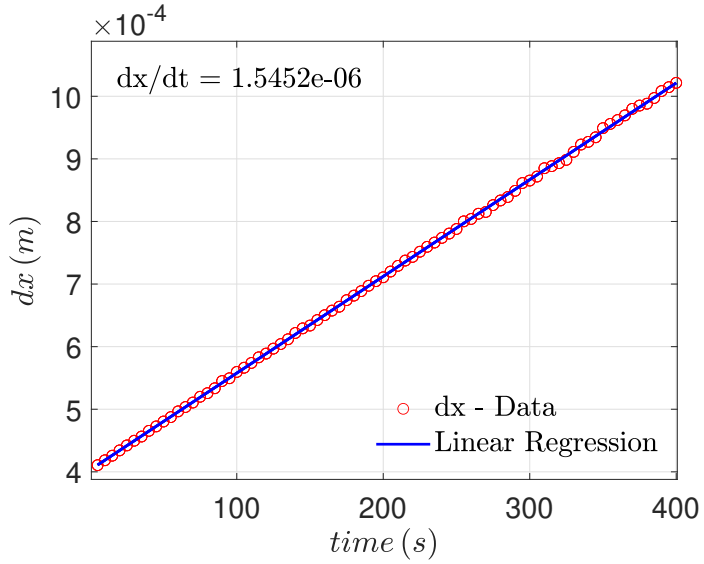

Fig. 3.23 Sample OFI regression

Chapter 4

Wall shear stress measurements

Introduction

Accurate measurement of wall shear stress, τ_w, in pipe flows or in wind tunnels, is crucial to understand the dynamics of turbulent boundary layer and the general behavior of fluid over surfaces. Wall shear stress, which represents the friction force exerted by the fluid on the wall, plays a central role in characterizing the drag forces that affect the efficiency of vehicles, aircraft, and industrial systems. A precise measure of τ_w is essential also for the validation of the computational models, improvements for drag reduction strategies and ensure the reliability of flow control techniques. In this chapter, we aim to address the uncertainty associated with two specific methods: static pressure drop measurements and local measurements using Oil Film Interferometry (OFI). The goal is to highlight how these uncertainties affect the accuracy of wall shear stress estimation and, subsequently, how these uncertainties propagate into normalized flow statistics. This analysis is crucial for interpreting experimental results in high-Reynolds-number turbulent flow studies. Moreover, an analysis of the OFI technique applied to validate an active flow control algorithm can be found in Appendix A.

4.1 Experimental setup

Measurements of wall shear stress in the Long Pipe are carried out using two distinct methodologies: static pressure drop measurements along the pipe and the Oil Film Interferometry (OFI) technique, which computes the evolution of interference fringes to directly determine wall shear stress. Each method offers unique insights into the flow characteristics, with the static pressure drop method providing an averaged, global measurement over a considerable

length of the pipe, and the OFI technique allowing for localized high-resolution assessments. The Long Pipe at the CICLoPE laboratory is equipped with 22 sections, each containing seven pressure taps designed to capture the static pressure at multiple locations (see Fig.4.1). The taps, with an internal diameter of $d = 2\,mm$, are strategically placed to ensure comprehensive pressure measurements. Four of these taps are mounted on the top of the pipe section and are spaced $1\,m$ apart, allowing for an accurate gradient to be measured along the pipe's length. Additionally, four wall taps are distributed around the circumference of the pipe, positioned 90° apart from each other.

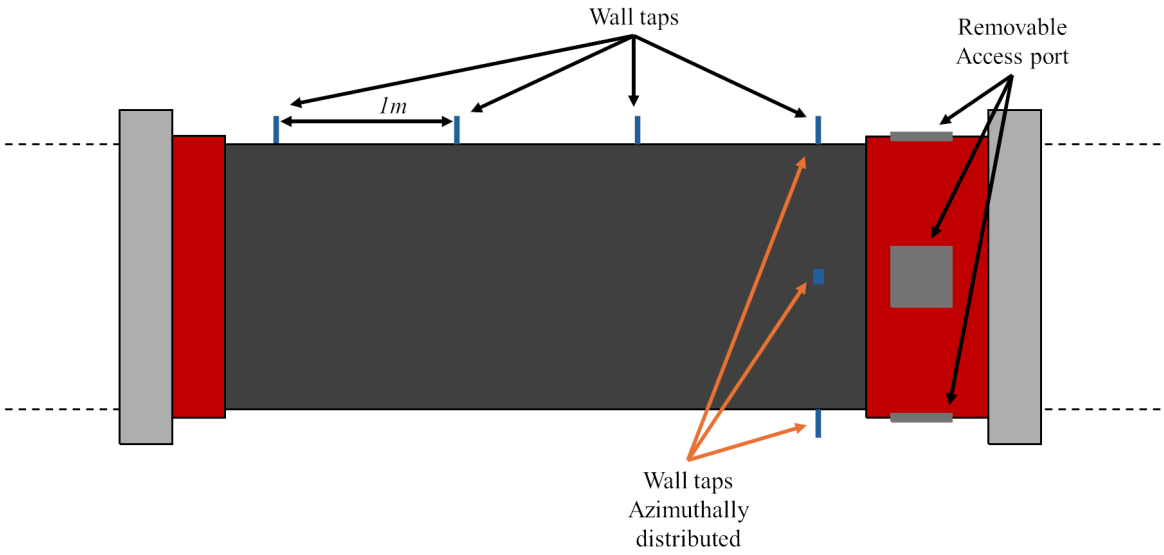

Fig. 4.1 Schematic view of the wall shear stress measurements setup in the Long Pipe

Static pressure measurements are acquired using a differential pressure multi-scanner (DTC Tnitium), which enables simultaneous readings from multiple taps. Alternatively, a mechanical scanivalve is used to connect the taps to a single differential pressure transducer for sequential measurements. The choice between these acquisition systems depends on the specific requirements of the experimental campaign, with the multi-scanner offering faster data acquisition at the expense of potentially higher uncertainty due to multiple transducers being used, each with its own calibration characteristics. In contrast, the single transducer setup provides more consistent measurements, though it introduces systematic bias errors that need to be carefully corrected. Together, these techniques ensure that the static pressure drop can be measured with precision, providing a critical data point to calculate the wall shear stress via the pressure gradient along the pipe.

- **Pressure Multi-Scanner System:** All 21 wall taps were connected to a pressure multi-scanner. In this setup, each pressure transducer has its own associated uncertainty, which can be treated as a random error.
- **Single Pressure Transducer System:** The wall taps were connected, by means of a mechanical Scanivalve, one at a time, to a single pressure transducer. This introduces a systematic bias error into the measurement campaign. However, if this systematic error is known, it can be easily filtered out.

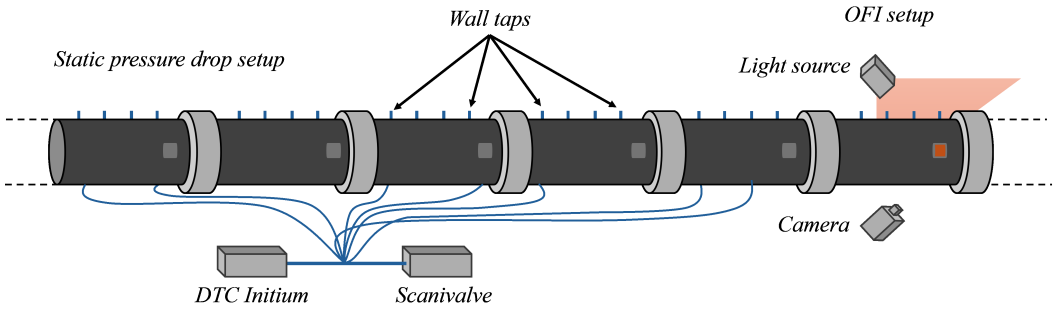

Fig. 4.2 Schematic view of the wall shear stress measurements setup in the Long Pipe

To compare global measurements from the static pressure drop and local measurements from Oil Film Interferometry (OFI), it is important to highlight the key differences in scope and methodology between the two approaches. The static pressure drop method evaluates wall shear stress over the last 60 meters of the Long Pipe, which is 111.5 m in length. This method provides a more global measurement, as it integrates the effects of the entire flow over a large section of the pipe. By measuring the pressure variations along this distance, the wall shear stress is derived as an average value over the pipe's length. While robust, this method can be influenced by imperfections in pressure taps, and residual flow development effects.

In contrast, OFI offers a localized measurement of wall shear stress. This technique directly measures wall shear stress at a specific point on the pipe surface by capturing the evolution of the fringes formed by the oil film applied to the wall. As discussed in Chapter 2, OFI is highly suitable for capturing local flow phenomena, which is especially important in the vicinity of the test section. OFI's ability to provide localized data offers a more detailed view of the small-scale turbulent structures that contribute to the overall wall shear stress. The OFI setup, as shown in Fig. 4.3, is placed in the test section of the Long Pipe. The measurement setup consists of the following components:

- An oil drop is applied on the wall surface of the pipe in the test section.

- A sodium lamp is used as the light source, positioned at a 45-degree angle to the pipe surface to illuminate the oil film and enhance reflection effects on the camera.
- A reflex camera is placed at a corresponding 45-degree angle to capture the evolution of the oil film fringes.

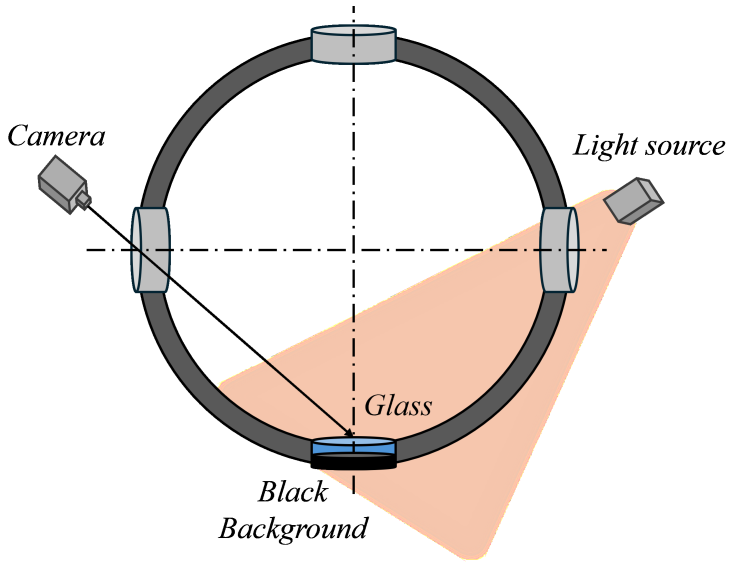

Fig. 4.3 Schematic of the OFI setup in the test section of the Long Pipe, illustrating the placement of the sodium lamp, reflex camera, and black background. The oil drop is applied on the pipe wall, and fringes are captured as the flow develops.

Figure 4.4 shows an actual photograph of the experimental setup, with the sodium lamp and reflex camera in place, illustrating the practical implementation of the configuration. By combining the global static pressure drop method and the local OFI method, we obtain a comprehensive understanding of the wall shear stress distribution in the Long Pipe. Table 4.1 highlights the range of Re_τ, Fan speed setup and reference quantity for τ_w, bulk velocity and characteristic length of the vortices assessed during the experimental activities. During the experiments, the centerline velocity will be measured using a Prandtl type pitot probe, ambient pressure p_{amb} and temperatures T were monitored in the test section using respectively an absolute pressure transducer and two different $PT100$ thermistor placed at the centerline of the pipe and at the wall.

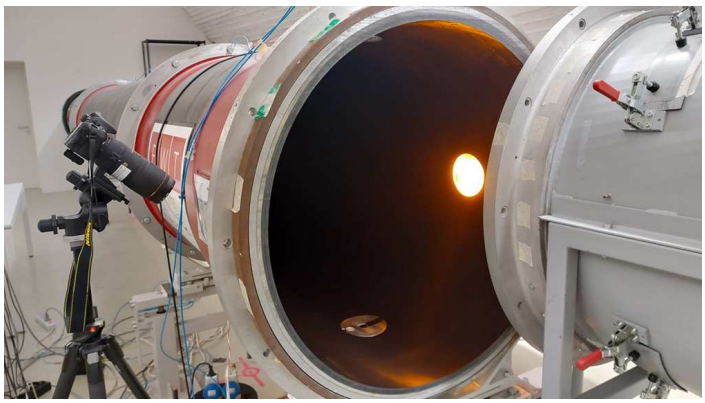

Fig. 4.4 Photograph of the OFI experimental setup, showing the sodium lamp and reflex camera arrangement in the test section of the Long Pipe.

$\tau_w(Pa)$	u_τ	Re_τ	$l_\star(m)$	$U_b(m/s)$	Fan (RPM)
0.022	0.13	4130	1.08e-4	3.17	100
0.054	0.21	6366	7.06e-5	5.10	150
0.099	0.29	8611	5.22e-5	7.06	200
0.157	0.36	10858	4.14e-5	9.12	250
0.228	0.44	13059	3.44e-5	11.17	300
0.311	0.51	15275	2.94e-5	13.27	350
0.407	0.58	17413	2.58e-5	15.31	400
0.514	0.66	19652	2.28e-5	17.48	450
0.635	0.73	21829	2.06e-5	19.61	500
0.763	0.80	23961	1.87e-5	21.71	550
0.910	0.88	26111	1.72e-5	23.87	600
1.065	0.95	28166	1.59e-5	25.91	650
1.230	1.02	30460	1.47e-5	28.19	700
1.435	1.10	32676	1.37e-5	30.41	750
1.631	1.17	34843	1.29e-5	32.60	800
1.843	1.25	37120	1.21e-5	34.88	850
2.067	1.32	39189	1.14e-5	36.98	900

Table 4.1 Experimental parameters for the characterization of the wall shear stress in the Long Pipe Facility.

4.2 Static pressure drop measurements

As described earlier, measurements were conducted across various flow regimes. Figure 4.5 presents the distribution of the pressure coefficient, C_p , for different Re_τ values as a

function of the axial coordinate x of the pipe, where $x = 0\,\text{m}$ corresponds to the exit of the convergent, and the test section is located at $x = 110\,\text{m}$. The C_p values were calculated using the centerline velocity measured approximately 4.5 diameters upstream from the test section.

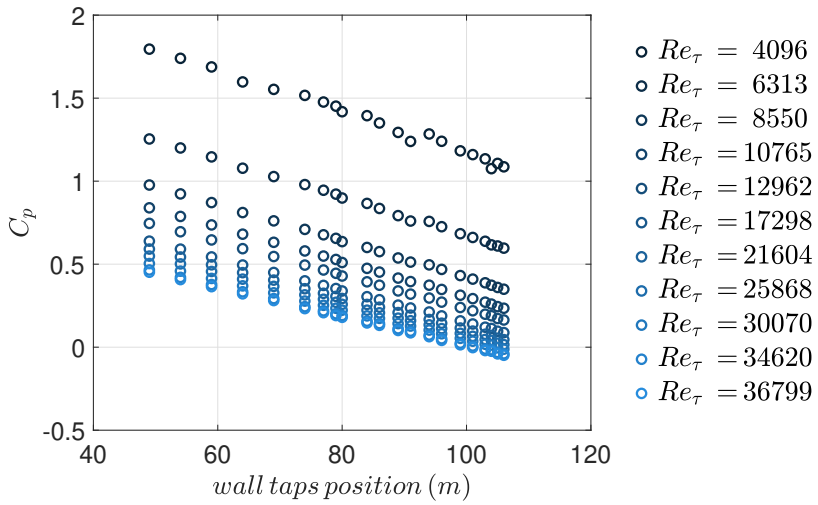

Fig. 4.5 Differential pressure measured in the Long Pipe, considering ambient pressure as a reference.

From Fig.4.5 a linear trend can be observed for all Re_τ cases, without any evident deviation. Even though C_p seems to reach negatives for the highest Re_τ linearity of the pressure drop seems preserved. Since the pressure drop in turbulent pipe flow follows a linear trend, the most straightforward method to compute it is by fitting a straight line to the experimental data points. A key consideration is determining the optimal number of data points to use, i.e., the length over which the linear fit should be applied. Ideally, the pressure gradient (dp/dx) should be measured at the exact location where the wall shear stress (u_τ) is being evaluated, as the pressure drop becomes constant only in fully developed pipe flow (Nikuradse et al., 1950; Schlichting and Gersten, 2016). Some residual flow development may still be present far from the test section. However, using a greater number of data points for the linear fit reduces the sensitivity of dp/dx to bias errors caused by individual pressure taps. Such deviations could arise from small imperfections in the wall pressure taps. To decide the number of pressure taps to be used in the fit, different linear fits were computed from the pressure data set of Fig.4.5, starting from the test section and progressively using an increasing number of upstream pressure taps. To assess the quality of the different fits, the error can be calculated as the difference between the pressure data and the value of the linear fit at the same axial location:

$$p_e(x) = p_{\text{data}}(x) - p_{\text{fit}}(x). \tag{4.1}$$

Then, the standard deviation of the error σ_{p_e} can be computed over the data points used for the fit. In Fig.4.6, σ_{p_e} is plotted against the number of pressure taps used for the fit, while in Fig. 4.7 the same quantity is normalized by a reference value for τ_w, which is taken as the friction velocity resulting from fitting all the points.

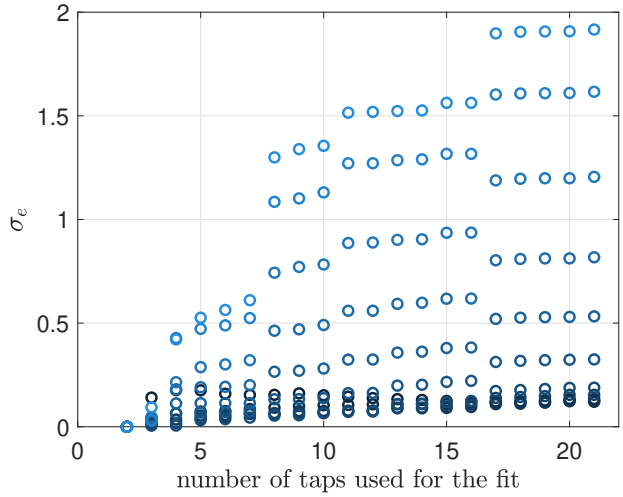

Fig. 4.6 Standard deviation σ_{p_e} of the pressure error as defined in the equation (4.1), displayed as function of the number of taps used to compute the linear fit, with the first one being always as close as possible to the test-section.

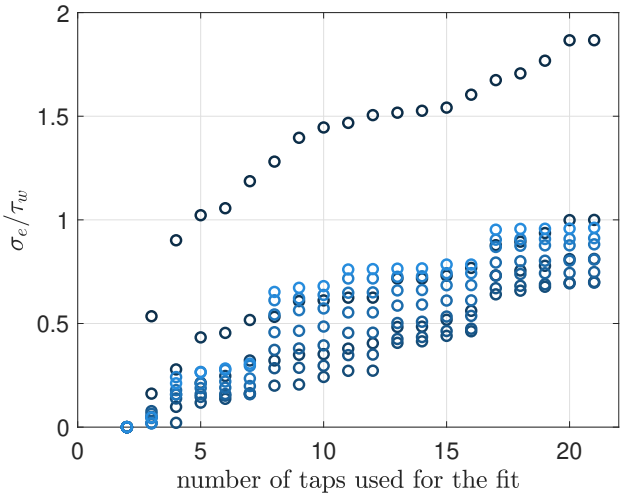

Fig. 4.7 Standard deviation σ_{p_e} of the pressure error as defined in the equation (4.1) normalized by the corresponding value of the wall shear stress τ_w, displayed as function of the number of taps used to compute the linear fit, with the first one being always as close as possible to the test-section.

As can be seen from Fig.4.6 and Fig.4.7, the absolute value of σ_{p_e} increases as more points are added to the fit (starting from 2 taps, where it has to be mathematically zero), and is higher for high Re_τ cases. Although, as seen in Fig.4.7, when normalized by a reference value of the friction velocity (the one resulting from using all the points in the fit), it becomes far more relevant for low Re_τ. It can also be noted that there is a discontinuity and a sharp increase in σ_{p_e} in correspondence with the fourth and ninth taps, possibly indicating a systematic deviation from the fit in those positions. From the standard deviation of the error of the fit, the 95% confidence interval for the slope a of the linear regression $y = ax + b$ can be calculated. For a distribution of n points with coordinates (x_i, y_i):

$$95\%\ \mathrm{CI}_a = \sqrt{\frac{\sum(y_i - ax_i - b)^2}{n-2}} \times \sqrt{\frac{n}{n\sum x_i^2 - (\sum x_i)^2}} \tag{4.2}$$

The 95% confidence interval for the slope of the fitted line is reported in Fig.4.8. It should be noted that the uncertainty computed here is just the uncertainty of the fit, and not the total uncertainty on the determination of dp/dx. Despite the slight increase in σ_{p_e}, the uncertainty in the pressure gradient decreases as more points are added to the fit, with a notable exception when 3 taps are used. Additionally, adding more taps beyond the 8th does not seem to significantly improve the uncertainty for most Reynolds number cases. Based on these observations, it was decided to use the last 8 pressure taps for the computation of the pressure gradient, corresponding to a length of 40 meters.

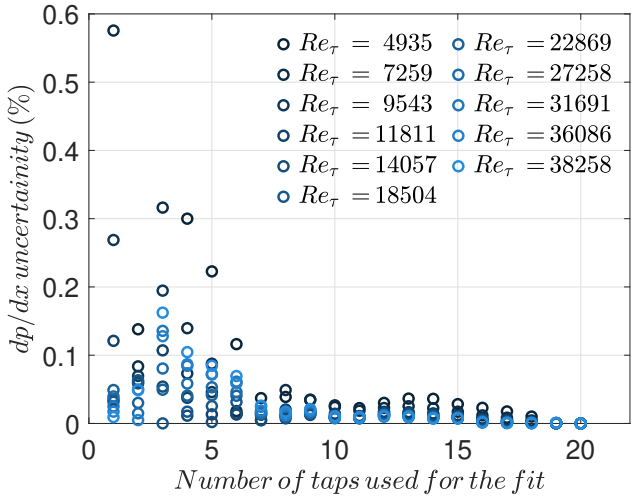

Fig. 4.8 The 95% confidence intervals for dp/dx (expressed as a percentage) are derived from the pressure errors in the linear fits. These intervals are shown as a function of the number of taps included in the fit, with the first tap consistently being the one nearest to the test section.

The procedure outlined was conducted using both acquisition systems mentioned earlier:

Consequently, the uncertainty associated with the measurements will differ depending on the system used. The multi-scanner system is affected by random errors from each individual transducer, while the single transducer system introduces a consistent systematic bias that can be accounted for and corrected if identified. Based on the computational steps described earlier, deviations from the fit were calculated for each wall tap and across all considered Re_τ values. This allowed us to identify potential imperfections in specific taps. Figure 4.9 illustrates the normalized mean standard deviation of the pressure difference from the fit, scaled by the wall shear stress τ_w. The plot shows how this deviation varies with the position of the wall taps along the Long Pipe, with $x = 110\,m$ marking the location of the test section. Highlighting potential issues in the instrumentation used to assess static pressure drop on each wall tap for the entire experimental campaign (i.e., if there is some clear discrepancy in one port).

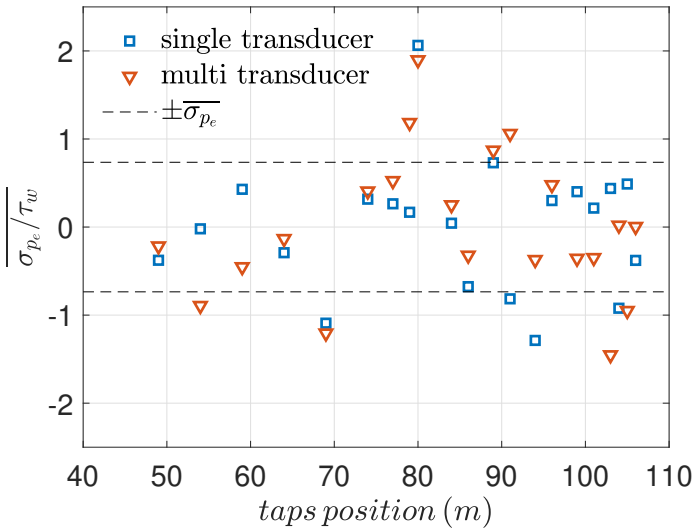

Fig. 4.9 Analysis of deviations from the fit across wall taps. (a) Normalized mean standard deviation of the pressure difference from the fit, scaled by the wall shear stress τ_w, as a function of wall tap position along the Long Pipe.

Figure 4.10 shows the mean values derived from the two measurement systems used, effectively eliminating any transducer or measurement effects. The dashed lines indicate the $\pm\overline{\sigma_{p_e}}$ values computed across all considered taps. This visualization aids in selecting the 8 taps for the fit calculation, helping to exclude any potential imperfections that could impact the static pressure drop calculation and, in turn, directly affect the uncertainty in τ_w. As can be seen from the plot, starting from farthest point on the left, 8 taps need to be picked, eliminating those who exceed the $\overline{\sigma_{p_e}}$ values.

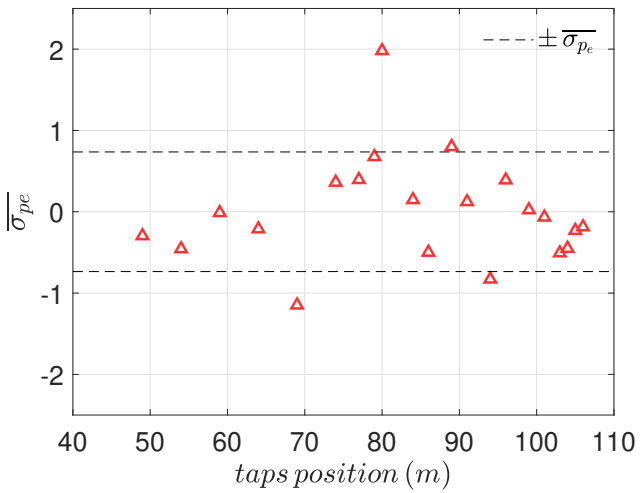

Fig. 4.10 Analysis of deviations from the fit across wall taps.

The static pressure drop can now be computed following the previously outlined steps, excluding any potential issues related to the experimental or instrumental apparatus. Figure 4.11 shows the static pressure drop as a function of Re_τ, comparing the current results with those from a past experimental campaign by Fiorini (2017) and literature data from McKeon et al. (2005). The trend is consistent across all pressure drop measurements, whether using single or multiple transducers. This confirms that a multi-pressure transducer setup can be effectively employed, with the added advantage of selecting wall taps during each acquisition. The selection of the multi-transducer is also based on the short acquisition time required, making it an efficient option. From this point forward, all τ_w values based on pressure drop will be computed using the described method.

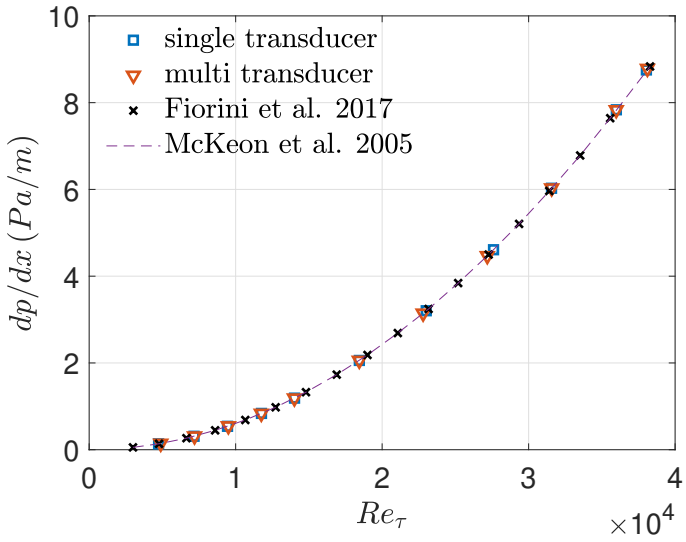

Fig. 4.11 static pressure drop computed as described in the section, data from multi-scanner, single scanner and Fiorini (2017) data

4.3 Oil Film Interferometry measurements

While the static pressure drop method provides an indirect approach to evaluating wall shear stress, Oil Film Interferometry (OFI) presents a more precise and localized alternative. As discussed in Chapter 3, OFI allows for the direct measurement of wall shear stress and offers significant advantages in terms of spatial resolution. Due to its relative small size, OFI captures wall shear stress as a local quantity, making it highly suitable for detailed flow analysis in comparison to the static pressure drop method, where wall shear stress is derived from an average value over a large portion of the pipe's length. In the case of the Long Pipe facility, static pressure drop measurements span approximately the last $40\,m$, which may obscure finer details of the flow. On the other hand, OFI enables the evaluation of shear stress at specific locations along the wall, providing crucial insights into localized flow dynamics, and enhancing the accuracy of turbulence characterization. This makes OFI particularly useful in complex experimental setups where precise measurement of wall shear stress is critical. In this section, we focus on assessing the measurement uncertainty associated with the Oil Film Interferometry (OFI) technique for wall shear stress estimation. Several factors contribute to the uncertainty, and a careful evaluation is critical to ensure the reliability of the results. The main steps taken to quantify these uncertainties include an analysis of the time required to acquire the wall shear stress, determining the precise dimension of the interrogation area, and performing a Monte Carlo simulation to incorporate potential sources of error such as variations in temperature and angle of view. The OFI technique relies on capturing the evolution of interference fringes formed on an oil film applied to the test surface as can be seen from Fig.4.12. Initially, we waited for the Fizeau fringes to become clearly visible before beginning the acquisition process. This waiting period ensured that the fringes were fully developed, enhancing the accuracy of the wall shear stress measurement. The time required to observe the full evolution of the fringes directly impacts measurement accuracy. If the acquisition time is too short, the fringes may not fully develop, leading to an underestimation of the wall shear stress. Conversely, longer acquisition times could introduce additional uncertainties due to environmental factors such as temperature drift or unsteady flow conditions. For this reason, the optimal acquisition time was carefully evaluated based on the flow conditions within the Long Pipe. Figure 4.13 shows the evolution of fringes dimensions dx as function of time.

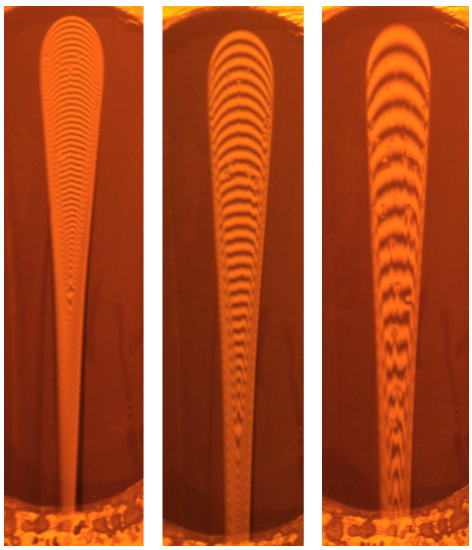

Fig. 4.12 Example of Fizeau fringes evolution in the test-section of the Long Pipe at three different instant of time, the image on the left is the first acquired while the one on the right highlights one of the last snapshot

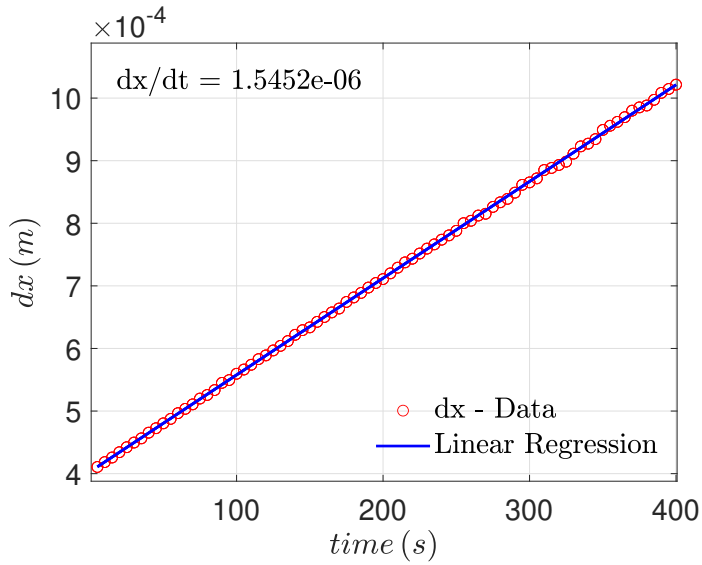

Fig. 4.13 fringes dimension evolution (dx) as function of the acquisition time expressed in seconds; every blue circles corresponds to a snapshot while the black dashed line represents the final regression computed using every snapshots

Figure 4.12 shows the fit error (compared to the one computed using the entire dataset available) as function of time, In the plot is quite clear how the error stabilize below $\pm 1\%$ after $\approx 150s$, thus suggesting that the acquisition time should be longer than that value. A slight overshoot of the error can be seen around 300 s while remaining under the error margin.

This can be caused by imperfection on the fringes due to dust particles that can be trapped in the oil film. Another key parameter is represented by the dimension of the interrogation area (see 4.15), which defines the spatial resolution of the measurement. The minimum interrogation area was set at $60\,px$, ensuring a sufficient number of pixels to accurately capture the fringe evolution. Measurements taken with a smaller interrogation area may result in an underestimation of the wall shear stress due to insufficient data resolution. Figure 4.15 shows the evolution of τ_w as we increase the length of the interrogation area, while keeping the width fixed. The interrogation area dimension effects stabilizes after $125px$, showing less than 1% variation once it reaches $200px$. This stability is crucial to maintain the reliability of the measurement.

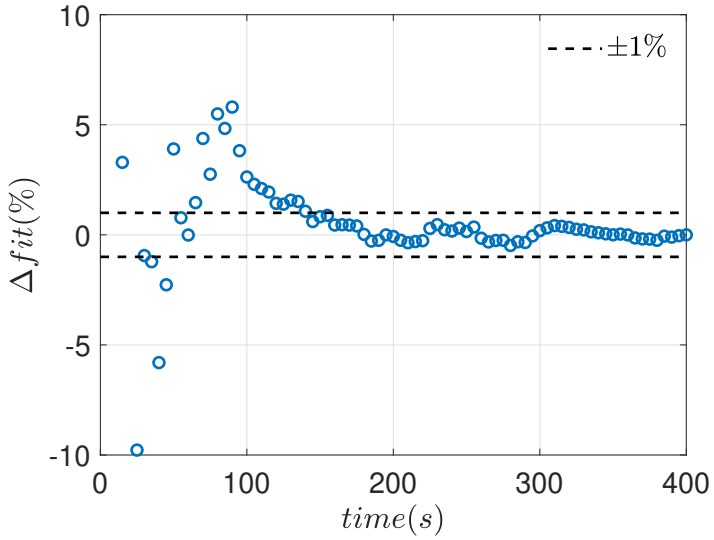

Fig. 4.14 Fit error of the wall shear stress, with respect to the one computed with the entire datasets, as function of acquisition time.

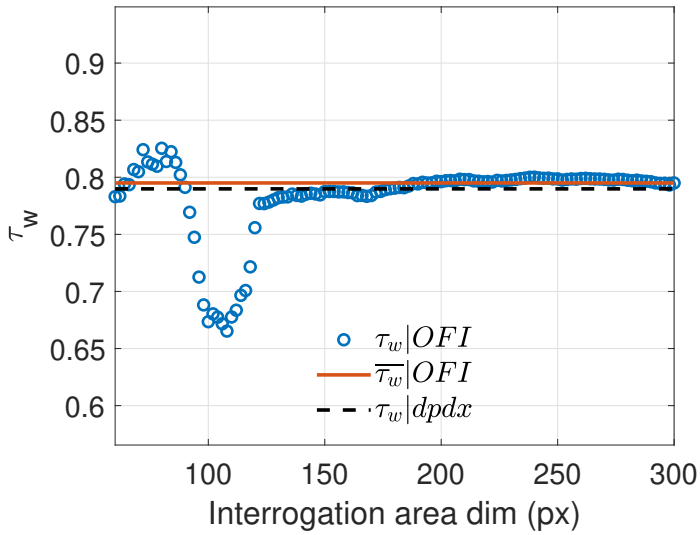

Fig. 4.15 Wall shear stress evolution as function of interrogation area dimension, expressed in px, red line highlights the τ_w mean value; balck dashed line depicts wall shear stress computed using static pressure drop.

To further ensure the accuracy of the wall shear stress measurements, the oil used in the experiments was carefully calibrated using a thermal bath and a capillary viscometer. A calibration curve was extrapolated from these measurements and used to compensate for any temperature drift during the experiments. This meticulous calibration process helps mitigate the influence of temperature variations on oil viscosity, thus enhancing the reliability of shear stress estimations. To quantify the overall uncertainty, a Monte Carlo simulation was conducted. This simulation included key variables such as temperature and the angle of view of the camera capturing the interference fringes. Those two parameters directly enter the computation of Δh as described in (3.34) thus, impacting directly τ_w values. The simulation was conducted on the entire available datasets considering the worst scenario of a random bias error in both temperature acquisition and angle of view.

- **Temperature Effects:** Since oil viscosity is temperature-dependent, any variation in the ambient temperature during the experiment can influence the shear stress estimation. The Monte Carlo simulation accounted for potential fluctuations in temperature, ensuring that the final results reflect a range of realistic conditions.
- **Angle of View:** The angle at which the camera views the oil film plays a significant role in the accuracy of the fringe measurement. Deviations from the optimal angle can distort the observed fringes, leading to errors in the wall shear stress calculation. By

incorporating this variable into the simulation, we evaluated how sensitive the results are to misalignment in the experimental setup.

The Monte Carlo simulation estimated the overall uncertainty for the wall shear stress measurements. Considering a 95% confidence interval, the analysis showed a potential error of $\pm 0.62\%$ in the wall shear stress measurement due to the combined effects of temperature fluctuations and camera angle misalignment.

The combination of a stable acquisition time (after 150 seconds), an adequately sized interrogation area (between $150px$ and $250px$), and careful consideration of temperature and viewing angle effects demonstrates that the OFI technique is a reliable tool for localized wall shear stress measurements. This small-scale, high-resolution measurement technique complements the global measurements obtained from static pressure drop, which integrates data over the last $40m$ of the $111.5m$-long Long Pipe.

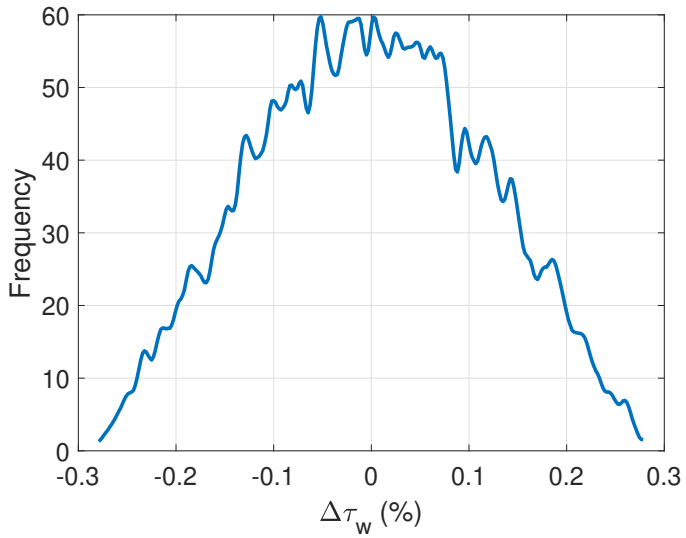

Fig. 4.16 Wall shear stress distribution as results of a montecarlo simulation considering bias errors in the temperature and in the viewing angle

These findings will be used to inform future experiments, particularly in optimizing the setup to further minimize uncertainty, ensuring more precise wall shear stress measurements across a wide range of flow conditions.

4.4 Uncertainty on wall shear stress in the Long Pipe

Wall shear stress measurements in the Long Pipe were obtained then using two distinct techniques: static pressure drop and Oil Film Interferometry (OFI). These parallel measurements

were conducted to evaluate and compare the uncertainties associated with each method, providing a comprehensive assessment of wall shear stress in high Reynolds number turbulent flows.

The static pressure drop method offers a global measurement of wall shear stress by integrating data over the last $40\,m$ of the Long Pipe. This technique assumes fully developed flow and relies on the linear relationship between pressure gradient and wall shear stress. However, it is susceptible to potential systematic errors due to imperfections in pressure taps and bias errors in the pressure transducers as described in the previous sections. Conversely, the OFI technique provides local measurements of wall shear stress. It captures the evolution of interference fringes formed by a thin oil film, offering high spatial resolution within the test section of the pipe. Although more sensitive to environmental factors such as temperature fluctuations and camera alignment, OFI enables the precise estimation of shear stress in a localized region, complementing the global perspective obtained from static pressure drop. Parallel measurements were performed using both methods to assess and minimize the uncertainty in wall shear stress estimation. The comparison between the global and local approaches is critical for developing a more accurate and robust measurement system for turbulent flow experiments in the Long Pipe.

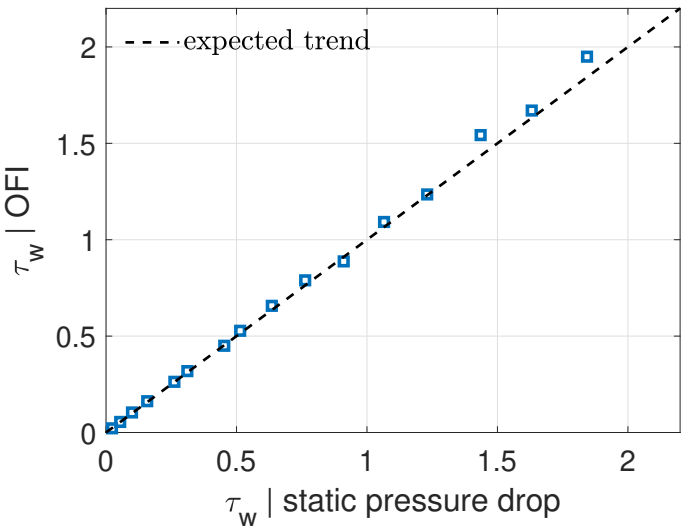

Fig. 4.17 Wall shear stress computed by means of OFI as function of τ_w computed using static pressure drop, black dashed line represents the expected trend

Figure 4.17 shows the comparison between the wall shear stress measurements obtained from both techniques, along with their expected trends. It can be seen that both methods closely follow the expected trend, although some deviations occur at higher Re_τ values.

While Fig. 4.17 captures the general agreement between the measurements, Fig. 4.18 highlights the deviation of the OFI results, using the static pressure drop as a reference quantity.

Based on the uncertainty analysis presented earlier A 2% error margin is considered in this comparison. OFI measurements are associated with a ±0.62% uncertainty, while the static pressure drop method carries a ±1% uncertainty due to fitting errors and transducer accuracy. Under these assumptions, we observe that the measurements fall well within the error band for Re_τ values ranging from 7,000 to 35,000. However, at very low Re_τ, the results deviate more noticeably, likely due to higher uncertainties in the pressure measurements, where very small pressure differences approach the transducer's resolution limits. Conversely, at higher Re_τ values, the OFI measurements become more prone to environmental factors—particularly dust particles accumulating on the oil film in the test section of the Long Pipe—which can distort the measurements done with oil film.

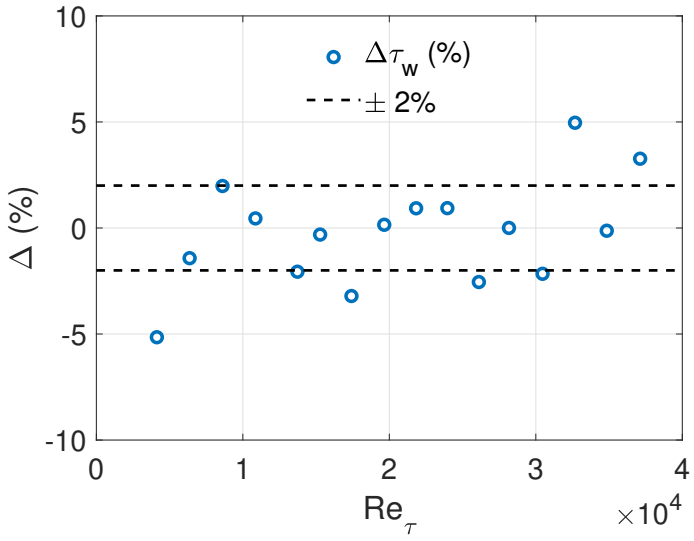

Fig. 4.18 Percentage deviation between wall shear stress computed using OFI and static pressure drop, black dashed line refers to an uncertainty of ±2%

The figure illustrates the relationship between the bulk Reynolds number (Re_{bulk}) and the friction coefficient (C_f) in turbulent pipe flow. Comparison of C_f values obtained using two methods: Oil Film Interferometry (OFI) (represented by red triangles) and pressure drop measurements (DPDX) (depicted by blue squares). Both methods exhibit the expected trend of decreasing C_f with increasing Re_{bulk}, consistent with the turbulent flow behavior in the pipes. For reference, a dashed black curve based on the empirical correlation from McKeon et al. (2005) is included.

Although the experimental data generally align well with the reference curve, a noticeable scatter is present at lower Reynolds numbers, particularly in the range of Re_{bulk} below 2×10^5. This deviation likely stems from inaccuracies in bulk velocity measurements, which are derived from pressure differences at the contraction located at the beginning of the Long Pipe. These discrepancies could influence the accuracy of C_f at lower flow rates, suggesting that potential refinements in the acquisition process may be necessary to improve data consistency in this regime.

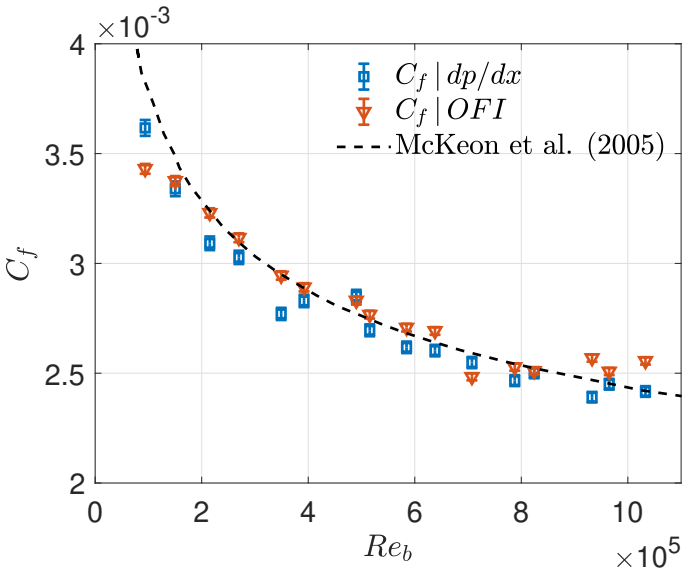

Fig. 4.19 Friction coefficients computed using both OFI and static pressure drop as function of Re_{bulk} which represents the Reynolds number computed by means of the bulk velocity of the pipe; black dashed line represents relationship by McKeon et al. (2005)

Chapter 5

Wall-pressure–velocity correlation

5.1 Introduction

The goal of the present work is to assess the scaling of the statistical correlation between wall-pressure and various components of the turbulent velocity in the logarithmic region of a fully-developed turbulent pipe flow. We present results based on a unique experimental dataset comprising synchronised time series of wall-pressure and velocity, at Re_τ values ranging from ones that are typical of high-fidelity DNS, up to ultra-high Reynolds numbers reaching close to $Re_\tau = 50$k. With similar experiments performed on a boundary layer flow up to a Reynolds number of $Re_\tau \approx 2\,000$ (Baars et al., 2024), a direct comparison between different canonical flows can be drawn, while exploring an unprecedented range of Reynolds numbers. We will address how the wall-pressure–velocity coherence displays Reynolds-number-independence, and how this appears to be universal across several wall-bounded flow configurations. To this end, § 5.2 describes the experimental facility and measurement approach along with the post-processing of the signals acquired. § 5.3 presents wall-pressure fluctuations. Subsequently, § 5.4.1 presents the coherence between wall-pressure (and wall-pressure–squared) and streamwise velocity; this includes a data-driven explanation of the mechanism involved in the larger coherence associated with the square of the wall-pressure signal. In § 5.4.2, a similar analysis considers the coherence between wall-pressure and the wall-normal velocity component.

5.1.1 Sparse sensors and definitions

In wind tunnel testing, time-resolved sensor acquisition focuses on capturing dynamic data at high temporal resolutions, often from sensors such as pressure transducers or microphones that monitor unsteady phenomena. These sensors ($S_1 \dots S_n$) are often sparsely placed at

location ($X_1 \dots X_n$) to balance data resolution and cost or physical limitations. Sparse sensor placement is particularly important in large wind tunnels, where covering the entire test section with sensors is impractical. Instead, key regions such as areas of high turbulence or surface pressure gradients are targeted to ensure meaningful and high-quality data acquisition. The ability to combine and process the signals from these sparsely located, time-resolved sensors is crucial to obtaining clean, usable data (P_i). Using techniques like POD or spectral analysis allows researchers to differentiate between real aerodynamic effects and the noise introduced by the wind tunnel environment.

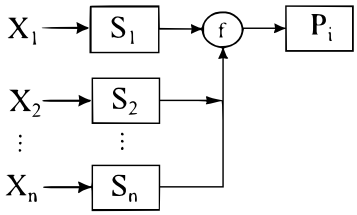

Fig. 5.1 Generic Sparse sensors definition, $X_1 \dots X_n$ represents the location of the n sensors, $S_1 \dots S_n$ indicates the sensors, f correspond to the filter applied, P_i represents the filtered signal

5.2 Experimental setup

An experimental campaign was carried out in the Long Pipe (see Figs. 5.2(a,b)). The facility is realised inside a mountain to minimise background noise and to keep stable environmental conditions, while sound-absorbing material near the two fans ensures minimal acoustic interference in the test section. The closed-loop facility comprises a 111.15 m-long circular pipe with a radius of $R = D/2 = 0.4505$ m. The flow in the test section (nominally at $x' = 105.9$ m = 117.5D downstream of the pipe inlet) can be considered fully developed. Further details relating to the design of the facility are described by Bellani and Talamelli (2016). For the experiments reported in this work, friction Reynolds numbers were in the range $4\,794 \lesssim Re_\tau \lesssim 47\,015$ (with corresponding centreline velocities of $3.837\,\mathrm{m/s} \leq U_{\mathrm{CL}} \leq 44.60\,\mathrm{m/s}$). All testing conditions are reported in Table 5.1.

5.2.1 Measurement instrumentation

Time-resolved pressure sensors were integrated in the wall of the pipe, each within its own cavity communicating with the flow through a pinhole orifice with a diameter of $d_p = 0.3$ mm (see Fig. 5.2(d)). The resonance frequency of the cavity was identified by

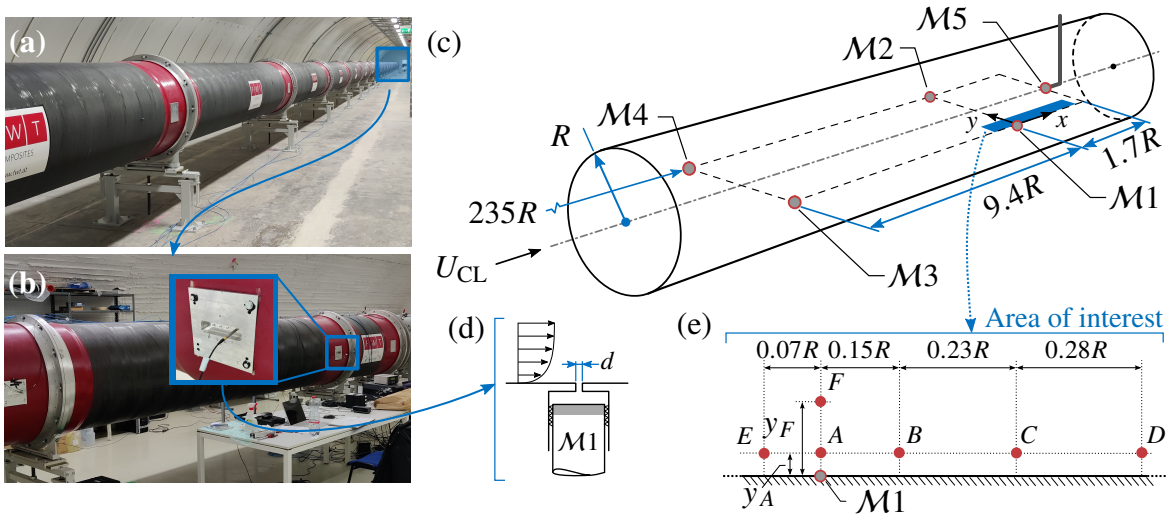

Fig. 5.2 (a) Photograph of the CICLoPE laboratory, with in (b) the test section at the downstream end of the long-pipe facility. (c) Schematic of the sensor placement ($\mathcal{M}1$ to $\mathcal{M}5$) in the pipe. (d) Schematic displaying the design of the pinhole cavity where pressure microphones were integrated. (e) Illustration of the points in the area of interest where acquisitions with single-wire and x-wire probes were performed.

means of an acoustic characterization experiment. Here, inlet and cavity pressures were measured simultaneously in quiescent flow in an anechoic facility. Then, a second-order model was fit to the gain of the linear transfer function, $|H_p(f)|$, relating cavity to inlet pressure in the frequency domain (Tsuji et al., 2007). With this procedure, the resonance of the pinhole-cavity was identified at $f_r = 4\,350$ Hz. This frequency lies beyond the frequency-range that was found to be relevant for the wall-pressure–velocity coherence, even at the highest Re_τ case tested.

The pressure sensors used in this study were GRAS 46BE ¼-inch CCP free-field microphones, chosen for their suitable dynamic range (35 to 160 dB, with a reference pressure of $p_{\text{ref}} = 20\,\mu$Pa) and accuracy of ±1 dB over the frequency range of 10 Hz to 40 kHz. Data acquisition was performed at a sampling rate of $f_s = 51.2$ kHz for a continuous duration of $T_a = 480$ s. The data were collected using two NI9234 analog-input boards with 24-bit A/D resolution. Five microphones were deployed (labeled $\mathcal{M}1$ to $\mathcal{M}5$ in Fig. 5.2(c)). Four microphones ($\mathcal{M}1$ to $\mathcal{M}4$) were flush-mounted in the pipe wall to measure wall-pressure fluctuations, while the fifth microphone ($\mathcal{M}5$) was positioned on a streamlined holder along the pipe's centerline to monitor the facility's acoustic noise. To reduce turbulence-induced pressure fluctuations caused by stagnation effects, microphone $\mathcal{M}5$ was equipped with a GRAS RA0020 nosecone. The wall-mounted microphones were arranged in two streamwise pairs, with a separation distance of 4.22 m ($\Delta x = 9.37R$). Each pair was installed in azimuthally opposite positions to help mitigate acoustic noise. For the purposes of the

	Case	1	2	3	4	5	6	7
	Label	—	—	—	—	—	—	—
Physical flow parameters	Re_τ	4794	7148	14004	22877	31614	38271	47015
	U_τ (m/s)	0.162	0.242	0.473	0.773	1.068	1.293	1.588
	τ_w (Pa)	0.032	0.070	0.269	0.718	1.368	2.008	3.001
	l^* (μm)	94.0	63.0	32.2	19.7	14.3	11.8	9.58
	U_{CL} (m/s)	3.837	5.833	12.11	20.71	29.50	34.13	44.60
Instrumentation characteristics	d_p^+	4.257	6.347	12.43	20.31	28.07	33.98	41.75
	l_{HW}^+	13.30	19.84	38.86	63.48	87.72	106.2	130.5
	f_{s}^+	29.71	13.36	3.482	1.305	0.683	0.466	0.301
	$T_a U_{\mathrm{CL}}/R$	4088	6214	12902	22066	31431	36364	47520
	y_A^+	117.1	174.6	342.0	558.6	771.9	934.5	1148
	y_F^+	649.2	968.0	1896	3097	4281	5182	6366

Table 5.1 Flow parameters of the seven conditions tested in the CICLoPE long-pipe facility, with alongside nondimensional parameters of the instrumentation's geometry and acquisition details.

analysis, a Cartesian coordinate system was adopted, with the origin placed at the center of the pinhole of the pressure microphone as shown in Fig. 5.2(c). The x-axis corresponds to the streamwise direction (positive downstream), while the y-axis points in the wall-normal direction (positive towards the pipe centerline).

Time series of the streamwise velocity were recorded at two wall-normal locations within the logarithmic region ($y_A = 0.011\,\mathrm{m} = 0.025R$ and $y_F = 0.061\,\mathrm{m} = 0.135R$) and at five streamwise positions (labeled A to F in Fig. 5.2(e)) using hot-wire anemometry (HWA), synchronized with pressure signals acquired on the same hardware. The measurements were carried out using a Dantec Streamline 90C10 CTA module and a standard Dantec 55P15 single-wire boundary layer probe. In addition, wall-normal velocity time series were collected using a Dantec 55P61 miniature x-wire probe at two streamwise positions within the logarithmic region (positions A and F in Fig. 6.2(e)). Both single-wire and x-wire probes featured sensing lengths of $l_{\mathrm{HW}} = 1.25\,\mathrm{mm}$ with nominal wire diameters of $d_{\mathrm{HW}} = 5\,\mu\mathrm{m}$, resulting in an aspect ratio of $l_{\mathrm{HW}}/d_{\mathrm{HW}} \approx 250$. Hot-wire probes were calibrated *ex-situ* using a planar jet calibration method. For the single-wire probe, a 5^{th}-order polynomial was fitted to 11 velocity points to obtain the calibration curve $U = f(E)$, where E represents the measured voltage. The x-wire probe was calibrated using seven velocity settings and thirteen angular orientations to generate a two-dimensional look-up table following the

procedure outlined by Burattini and Antonia (2004). This table relates the two velocity components, (U_1, U_2), to the voltages measured by the respective wires, (E_1, E_2). During the experiments, the probe was aligned to measure the streamwise (u) and wall-normal (v) velocity components simultaneously.

5.2.2 Noise-filtering of wall-pressure signals

Even though the facility has been designed to minimize noise in the test section, acoustic contamination is present. Due to the spectral overlap of acoustic facility noise and hydrodynamic wall-pressure fluctuations, a filtering technique was implemented to remove the former. This technique employs harmonic proper orthogonal decomposition (hPOD). For a review of hPOD see the work by Tinney et al. (2020). First, POD kernels are constructed from cross-spectral densities of, in this case, the various pressure signals. Then, the solution of an eigenvalue problem yields the frequency-dependent mode shapes and eigenvalues. By only retaining modes of the measured pressure time series, in which the spectral signature of acoustic noise is absent, the hydrodynamic wall-pressure signal is isolated. Technicalities of the noise-removal procedure can be found in § 2.5.

The presence of acoustic noise within the time series of wall-pressure has not only implications for the wall-pressure spectra, but also for correlation analyses. By construction, acoustic noise and velocity fluctuations are uncorrelated. Consequently, a normalized correlation of the two is lower than the true value when such additive noise is present (Saccenti et al., 2020). To assess the degree of acoustic contamination, a signal-to-noise ratio (SNR) is defined as the intensity-ratio of turbulence-induced hydrodynamic wall-pressure fluctuations, $p_w(t)$, relative to those induced by facility noise: $\mathrm{SNR} = \overline{p_w(t)}^2 / \left(\overline{p_r(t) - p_w(t)}^2\right)$. Here, $p_r(t)$ is the raw microphone pressure (with both acoustic and hydrodynamic content). SNRs in our dataset increase monotonically with Re_τ in the interval $0.08 \leq \mathrm{SNR} \leq 0.25$. Thus even though the noise-removal procedure is intended to retain hydrodynamic wall-pressure only, imperfections in the method presumably yield a larger degree of uncorrelated noise in the low Reynolds number datasets.

Wall-pressure measurements by means of microphones embedded in surface-flush pinholes results in signal contamination from two main sources: (1) acoustic noise from the wind tunnel facility and (2) acoustic resonance of the pinhole cavity as can bee seen in the gray line of Fig.5.3 that highlights raw power spectral densities of wall pressure fluctuations measured by microphone $\mathcal{M}1$. While a correction for the latter can directly be implemented in the frequency domain and takes the form of a division of the spectrum by a correction kernel (Tsuji et al., 2007), the former requires a more elaborate procedure. In particular, when considering a raw microphone signal from one of the sensors in Fig. 6.2(c), it is necessary to

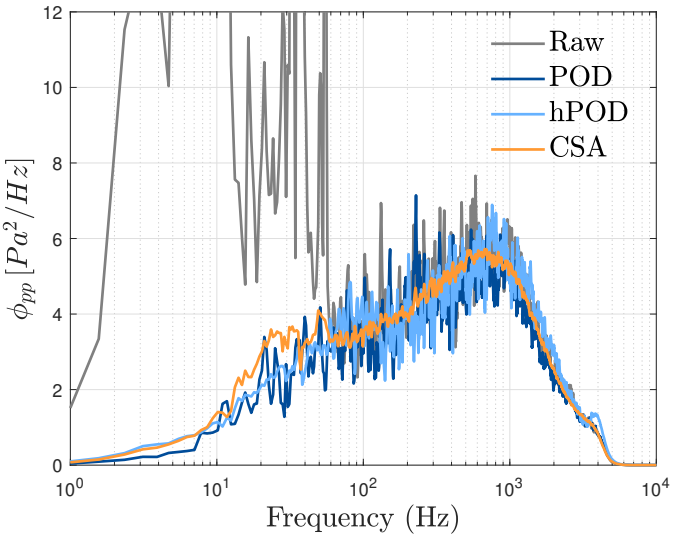

Fig. 5.3 Power spectral densities of the hydrodynamic pressure fluctuation from microphone $\mathcal{M}1$ at $Re_\tau = 14004$: raw signal (grey), filtered using classical POD (blue), filtered with harmonic POD (light blue) and filtered using CSA (orange).

disambiguate hydrodynamic wall-pressure information from the pressure fluctuations merely caused by acoustics. In the case of turbulence-induced fluctuations, especially wall-pressure, they possess negligible streamwise and spanwise coherence when considering relatively large sensor separations. Acoustic pressure fluctuations, however, convect from sensor to sensor retaining high correlation between detection stations, both in the streamwise and the spanwise directions.

With the experimental setup illustrated in § 5.2, the acoustic waves produced by the operation of the CICLoPE facility will be detected by both the pinhole-embedded microphones, $\mathcal{M}1$ to $\mathcal{M}4$, and the centreline microphone, $\mathcal{M}5$. However, the signal measured by $\mathcal{M}5$ will not contain hydrodynamic wall-pressure fluctuations, given its mounting position. Removing acoustic noise requires the identification of spatial modes that are correlated among sensors and whose signatures can be detected at the centreline microphone. To do so, we resort to three different methodology: proper orthogonal decomposition (POD), harmonic proper orthogonal decomposition (hPOD) and spectral subtraction method. Figure 5.3 reports the effect of the three filtering procedures for one Reynolds number, namely $Re_\tau = 14\,004$. As per the figure, all proposed techniques successfully attenuate facility noise. Only a negligible amount of acoustic energy survives at low frequencies in the case of the spectral subtraction method at low Reynolds number. Since POD and hPOD rely on manual mode selection, one must carefully select the modes to retain, since the nominal modes can change from one Reynolds number case to another. This considerably increases the complexity and scalabil-

ity of the method. On the other hand, spectral subtraction method automatically acts upon correlated signals. However, this approach may see a decrease in effectiveness when dealing with partially correlated signals. Inspecting the final filtered result in Fig. 5.3, there is no clear advantage in selecting one of the methods described. Harmonic POD will be used from now on to filter out noise. This method differs from conventional POD, in that the spatial decomposition is now made frequency-dependent (see Tinney et al., 2020). Using Tinney's notation, hPOD allows to compute a set of eigenvalues and eigenmodes of the harmonic complex-valued kernel $\check{R}$:

$$\check{R}(\mathbf{x},\mathbf{x}';f) = \frac{1}{2\pi}\int_{-\infty}^{+\infty} \langle p_{w,i}(\mathbf{x},t)p_{w,j}(\mathbf{x}',t+\tau)\rangle e^{-i2\pi f\tau} d\tau, \tag{5.1}$$

Here, $p_{w,i}$ and $p_{w,j}$ represent different pressure signals, while $\mathbf{x}$ denotes the vector containing the sensor coordinates (for example, $\mathbf{x}_{\mathcal{M}1}$ represents the spatial coordinates of microphone $\mathcal{M}1$). Essentially, $\check{R}$ quantifies the spectral cross-correlation between the two input signals. Unlike conventional POD, where the signal is decomposed into real eigenvalues and eigenmodes, hPOD decomposes the signal into complex-valued, frequency-dependent eigenvalues and eigenmodes. The spectral eigenvalues $\Lambda^{(n)}(\mathbf{x},f)$ form a matrix with dimensions $N_s \times N_f$, where N_s is the number of sensors ($N_s = 5$ in this study), and N_f is the temporal FFT ensemble size (set to $N_f = 2^{15}$ in this work, giving a frequency resolution of $\Delta f = 1.56\,\mathrm{Hz}$). The harmonic eigenmodes $\phi^{(n)}$ are complex-valued and have dimensions $N_s \times N_m \times N_f$, where $N_m = N_s$ is the number of modes.

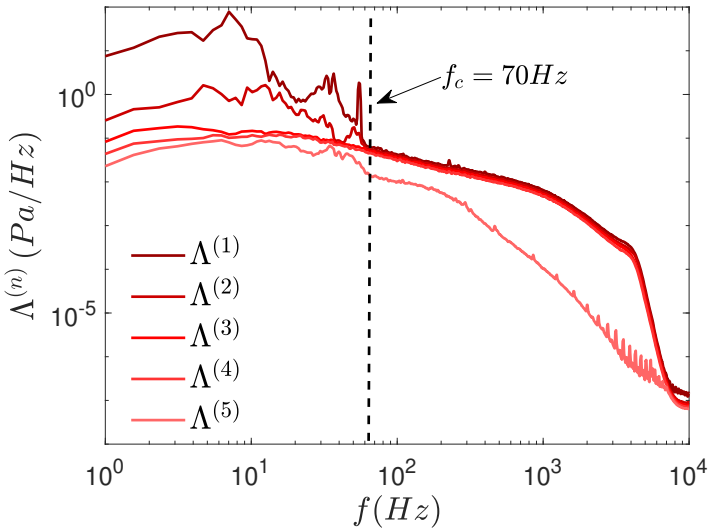

Fig. 5.4 Spectra of the eigenvalues of the complex-valued $\check{R}$ kernel at $Re_\tau = 14\,004$.

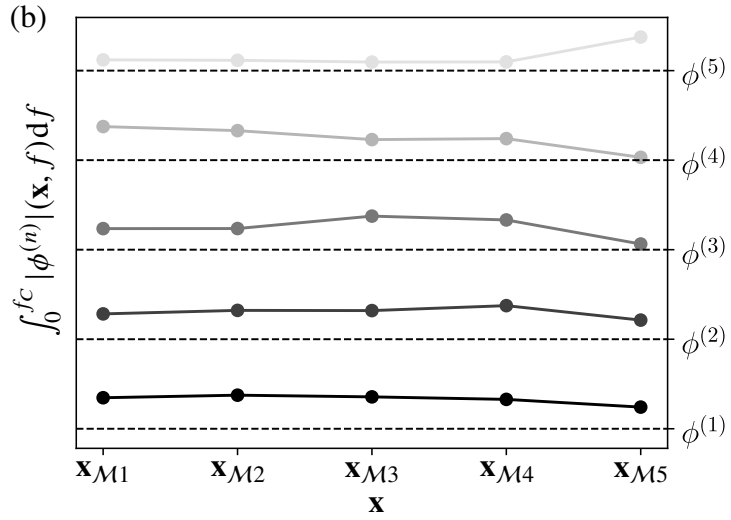

Fig. 5.5 Normalised magnitude of the complex modes $\phi^{(n)}$, integrated in the range $0 < f \lesssim 70\,\mathrm{Hz}$ at $Re_\tau = 14\,004$. Each curve is offset by one unit vertically for graphical readability.

Upon applying hPOD to the microphone signals from the CICLoPE facility, the spectral distribution of the five eigenvalues is presented in Fig. 5.4 for $Re_\tau = 14\,004$. The first two eigenvalues show the most contamination by facility acoustic noise, especially at the low frequencies. The spectral distribution of the first four eigenvalues assumes the typical power-law decay trend in the mid-to-high frequency band. The fifth eigenvalue only contributes significantly to the total energy of the wall-pressure pressure in the low-frequency band of the plot, with negligible energy found beyond $f \gtrsim 60\,\mathrm{Hz}$. To determine which mode set to retain for filtering the wall-pressure signals, the spatial distribution of eigenmodes should be examined. In particular, by construction of the experiment, the ideal set of modes to retain consists of the ones that exhibit no activity at the centreline microphone, $\mathcal{M}5$. To aid in the selection of modes, it is convenient to only consider eigenmodes in the range of $0 < f < f_C$, with $f_C = 70\,\mathrm{Hz}$, as the facility-induced acoustic noise is concentrated in this band. The magnitude of the eigenmodes, integrated in the aforementioned frequency range, is displayed in Fig. 5.5. Upon inspection of the five curves, it is clear that modes 3 and 4 are the ones showing the least (negligible) activity at the centreline microphone $\mathcal{M}5$. Based on this, it was decided reconstruct the wall-pressure signal purely based on these two modes and to discard modes $\phi^{(1)}$, $\phi^{(2)}$ and $\phi^{(5)}$. The energy content of all individual eigenvalues was also inspected and reported in Fig. 5.6, where the energy content per mode (relative eigenvalue contribution) is plotted in the bar chart as a function of the number of modes. The cumulative sum of of the energy is also calculated in order to check that total energy is preserved by the selected algorithm as can be seen in the solid black line in Fig. 5.6.

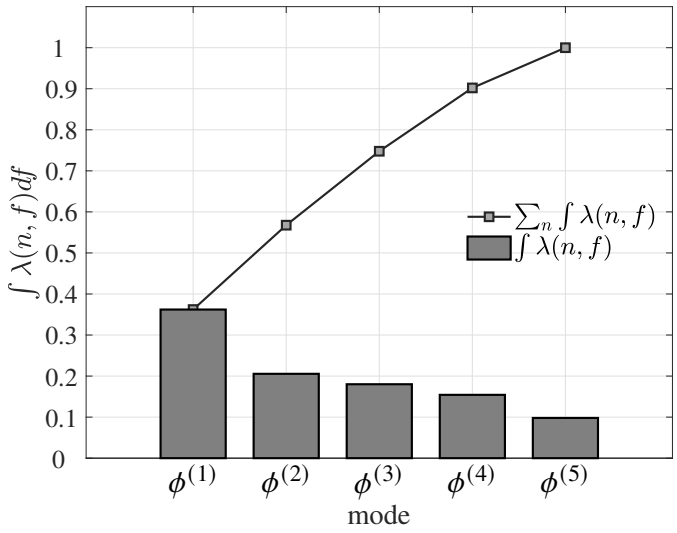

Fig. 5.6 Relative energy content per mode (grey bar plot), cumulative sum of the energy contained in each harmonic mode (solid black curve);

For the other friction Reynolds numbers considered in this study (see Tab. 5.1), a similar procedure was applied. Similar conclusions could be drawn in regards to the selection of modes to retain for filtering, with the only minor difference lying in the selection of the upper frequency bound for acoustic contamination, f_C. For increasing Reynolds numbers, f_C increases, following a greater fan angular velocity.

5.3 Wall-pressure fluctuations

The wall-pressure signals, after noise correction, are reconstructed by retaining only the two most significant modes, and the corresponding power spectral densities (PSDs) are presented in Figs. 5.7 and 5.8. The spectra show a clear alignment of the inner spectral peak at a streamwise wavelength of $\lambda_x^+ \approx 250$, which is consistent across the different Reynolds numbers. Additionally, with increasing Re_τ, a significant rise in the large-scale energy content is observed, in agreement with well-established trends in wall-bounded turbulence literature. This highlights the growing contribution of large-scale motions at higher Reynolds numbers, further emphasizing the importance of accurate noise filtering. Moreover, the large-scale tails of the spectra collapse when the streamwise wavelength is scaled in outer units, as shown in Fig. 5.8. This collapse suggests a form of Reynolds number similarity in the large-scale structures of the flow, reinforcing the universality of wall-pressure spectra in high-Re_τ turbulent flows. The corrected spectra are displayed in Fig. 5.7, where the raw wall-pressure

PSDs are plotted as a function of the inner-scaled streamwise wavelength, $\lambda_x^+ = U_c^+ / f^+$. Here, $U_c^+ = 10$ is taken as the convection velocity, and f^+ represents the inner-scaled frequency. Notably, for the three highest Reynolds number datasets (denoted as sets 5 to 7), a distinct 'wiggle' appears in the spectrum around the location of the inner spectral peak at $\lambda_x^+ \approx 250$. This irregularity is attributed to an imperfect correction for the resonance effect within the pinhole cavity, which is slightly modified in the presence of flow compared to the acoustic calibration conditions. It is important to note that at lower Reynolds numbers, the resonance frequency of the pinhole cavity lies far beyond the range of energetic frequencies relevant to the wall-pressure spectrum. Consequently, the resonance effect becomes negligible at lower Re_τ. However, as Re_τ increases, this resonance frequency approaches the range of the turbulent fluctuations, potentially influencing the observed spectra, particularly in the inner spectral region. These results highlight the importance of accurately accounting for facility-induced effects, such as cavity resonance, to ensure reliable wall-pressure measurements in high-Reynolds-number turbulent flows.

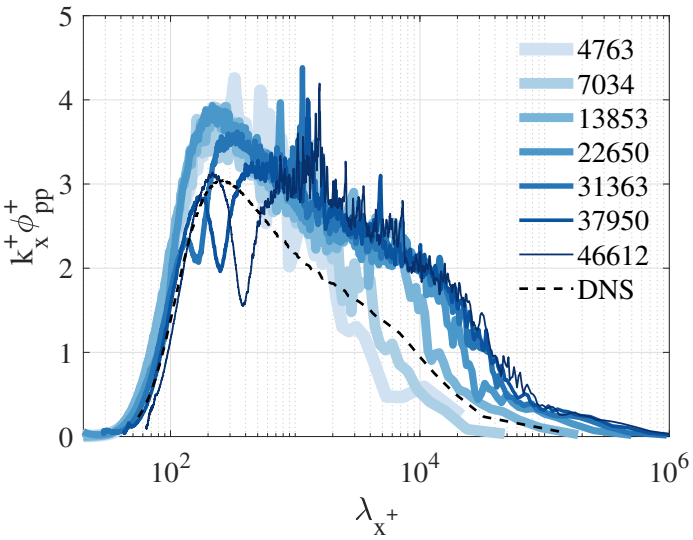

Fig. 5.7 Inner-scaled pre-multiplied power spectral densities of wall-pressure fluctuations acquired from microphone 1, filtered by means of hPOD, DNS data from(Lee and Moser, 2015)

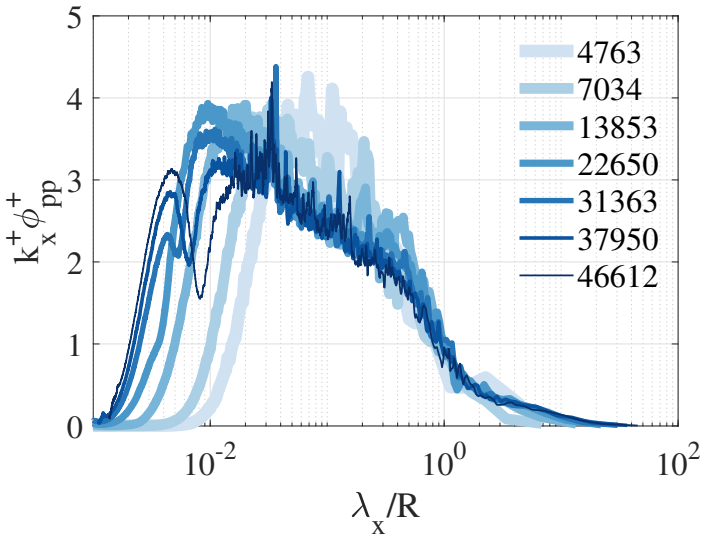

Fig. 5.8 Inner-scaled pre-multiplied power spectral densities of wall-pressure fluctuations acquired from microphone 1, filtered by means of hPOD.

Finally, the effectiveness of the noise removal approach is validated by comparing the wall-pressure intensity filtered using the three different techniques—POD, hPOD, and CSA—with empirical relations provided in Klewicki et al. (2007). As illustrated in Fig. 5.9, the filtered wall-pressure intensities show a good level of agreement with the established empirical findings. This comparison demonstrates the robustness of the filtering methods in capturing the relevant physical characteristics of the wall-pressure field. At lower Reynolds numbers (Re_τ), it is observed that the results from the CSA filtering method slightly deviate from those obtained using POD and hPOD. This discrepancy can likely be attributed to the lower effectiveness of CSA in filtering out noise at very low velocities, where the signal-to-noise ratio (SNR) is insufficient. In these conditions, the weaker signal may not be properly differentiated from noise, leading to a minor underestimation of the wall-pressure intensity. However, for moderate to high Re_τ, all three filtering techniques converge, showing excellent agreement, with the variation in pressure intensity being less than 5% across the different methods. This convergence suggests that the proposed filtering procedures are robust and reliable for higher Reynolds numbers, where the SNR is more favorable, and the flow's large-scale structures dominate the wall-pressure signal. Interestingly, deviations between the filtered intensities and the empirical laws are only noticeable when the inherent uncertainties of the experimental data are disregarded. This indicates that, within the bounds of uncertainty, the filtering techniques provide a faithful reconstruction of the wall-pressure intensities, further supporting their validity. Thus, the application of these noise-filtering algorithms proves to be effective in minimizing facility-induced noise while retaining the

essential flow physics, particularly at high Reynolds numbers where accuracy is critical for drag-reduction studies and other flow-control applications.

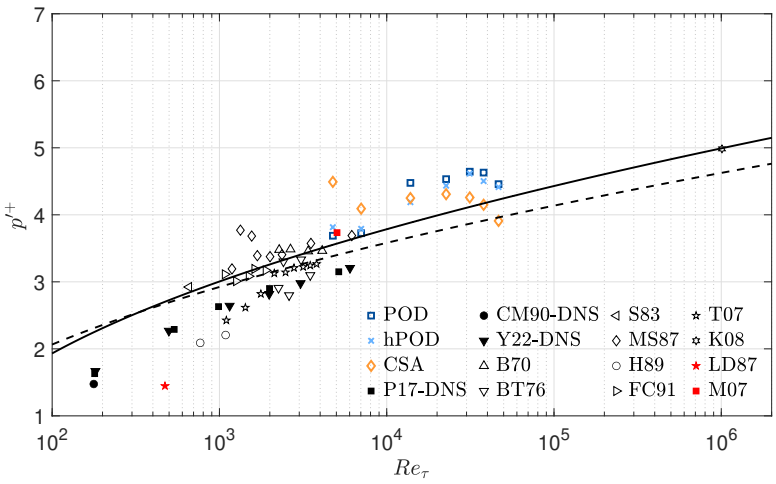

Fig. 5.9 Wall-pressure intensity inferred from integrating the wall-pressure spectra. Current results are compared to several datasets available from the literature. Data are taken from the DNS studies of Panton et al. (2017) (P17-DNS, •, ZPG-TBL), Choi and Moin (1990) (CM90-DNS, ▼, TCF) and Yu et al. (2022) (YU-DNS, ■, pipe flow). Furthermore, data are collected from experimental studies of ZPG-TBL flows: Blake (1970) (B70, △), Bull and Thomas (1976) (BT76, ◁), Farabee and Casarella (1991) (FC91, ▷), Horne (1989) (H89, □), Klewicki et al. (2007) (K08, ⬠), McGrath and Simpson (1987) (MS87, ☆), Schewe (1983) (S83, ⬡) and Tsuji et al. (2007) (T07, ○), and of experimental studies of pipe flows: Lauchle and Daniels (1987) (LD87, ★) and Morrison (2007) (M07, ♦). Solid and dashed lines are the formulations presented by Klewicki et al. (2007), in which the pressure variance increases logarithmically with increasing Re_τ.

5.4 Wall-pressure–velocity coherence

5.4.1 Coherence between streamwise velocity and wall-pressure fluctuations

To analyse the statistical spectral coupling between wall-pressure and streamwise velocity fluctuations, the LCS is employed. For two time series, of streamwise velocity fluctuations, $u(y,t)$, and wall-pressure fluctuations, $p_w(t)$, the LCS is defined as the ratio of the square of the magnitude of their cross-spectrum to the product of their auto-spectra:

$$\gamma^2_{up_w}(y,\lambda_x) \equiv \frac{|\langle \widetilde{U}(y,\lambda_x)\widetilde{P}_w(\lambda_x)\rangle|^2}{\langle|\widetilde{U}(y,\lambda_x)|^2\rangle\langle|\widetilde{P}_w(\lambda_x)|^2\rangle}, \tag{5.2}$$

where the angled brackets $\langle ... \rangle$ indicate ensemble averaging, and capitalised variables with a tilde indicate the application of the Fourier transform, *e.g.* $\widetilde{P}_w(\lambda_x) = \mathcal{F}[p_w(t)]$. The use of the LCS to describe spectral stochastic coupling in turbulence is well documented in the literature and describes the degree of *phase-consistency*.

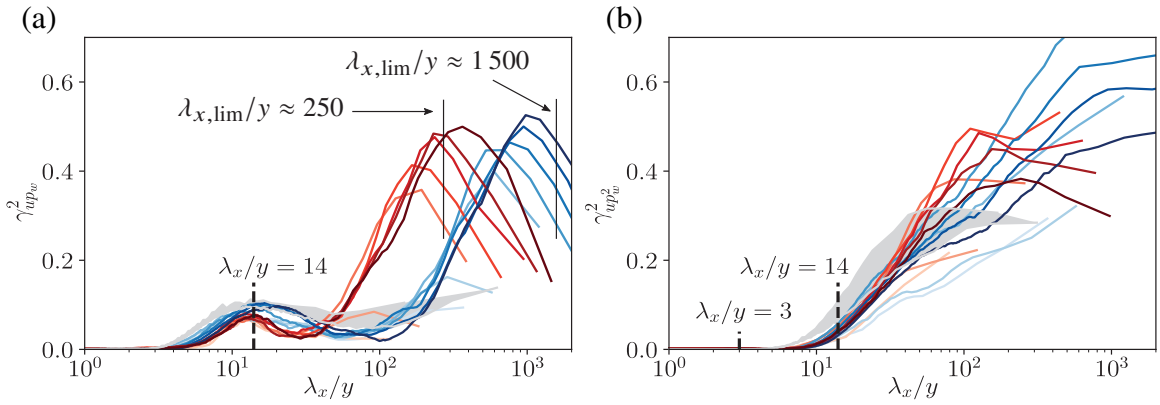

Fig. 5.10 (a) Coherence between streamwise velocity and wall-pressure and (b) wall-pressure–squared fluctuations at points A (blue colour scale) and F (red-based colour scale, with increasing saturation indicating increasing Re_τ) for $4\,794 < Re_\tau < 47\,015$.

Figures 5.10(a,b) report the LCS between $p_w(t)$ and $u(t)$ at positions A and F (see Fig. 6.2(e) for increasing Reynolds numbers. We hereby resort to wall-scaling to normalise the abscissa as λ_x/y, where $y = \{y_A, y_F\}$ for this graph. Wall-scaling reasonably collapses all curves (even with DNS data at $Re_\tau = 5\,200$). This therefore provides evidence that turbulent structures adhering to a self-similar scaling—according to the attached-eddy hypothesis (their flow topology scales with wall-normal distance y)—are the only structures that have a direct, linear imprint on the wall-pressure.

With minimal coherence observed at small wavelengths, a steady increase in the large-scale coherence structure (LCS) is seen in Fig. 5.10(a) as λ_x/y rises, peaking at $(\lambda_x/y, \gamma^2_{up_w}) \approx (14, 0.1)$. As λ_x/y increases further, a slight decrease in coherence is noticed, followed by a rise for $\lambda_x/y \gtrsim 10^2$. This rise remains in a spectral range where velocity fluctuations are still energetically relevant. Specifically, considering the amplitude threshold $k_x^+\phi_{uu}^+ = 0.2$ at the large-scale limits of pre-multiplied streamwise energy spectra, the energy drops below this threshold only for outer-scaled wavelengths of $\lambda_x/R \gtrsim 35$. This limit is included in Fig. 5.10(a), corresponding to $\lambda_{x,\mathrm{lim}}/y \approx \{250, 1\,500\}$ for $y = \{y_A, y_F\}$, respectively. Furthermore, the apparent increase in peak coherence as Re_τ rises is due to the incomplete removal of acoustic noise from the facility. Despite this, the coherence spectra collapse across the full range of Re_τ for both wall-normal positions, $y = \{y_A, y_F\}$. Additionally, an agreement between the experimental curves and DNS data of a turbulent channel flow (Lee and Moser,

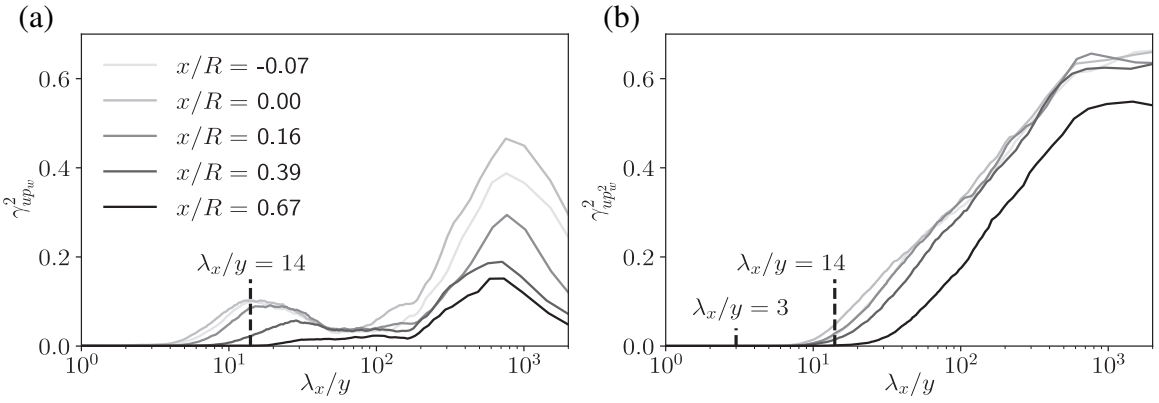

Fig. 5.11 (a) Light grey shaded area illustrates a comparison to DNS data from Lee and Moser (2015) on the left. Coherence between streamwise velocity and wall-pressure and (b) wall-pressure–squared fluctuations for $Re_\tau = 14\,004$ at $-0.07 < x/R < 0.67$ on the right.

2015) is clear. The DNS data, depicted by the grey shaded areas in Figs. 5.10(a,b), represent the range of LCS across different wall-normal positions in the logarithmic region ($80 \lesssim y^+ \lesssim 0.15Re_\tau$, with $Re_\tau = 5\,200$, see Fig. 6 of Baars et al., 2024). Though not shown for clarity, lower Reynolds number TBL flow data also align with the grey shaded region (Baars et al., 2024; Gibeau and Ghaemi, 2021).

When proceeding with the coherence involving the nonlinear term of the wall-pressure, we define the wall-pressure–squared as $p_w^2(t) = p_w^2(t) - \overline{p_w^2(t)}$. In contrast to the behavior displayed by the linear term of wall-pressure, the LCS between wall-pressure–squared and streamwise velocity fluctuations rises sharply starting from $\lambda_x/y \approx 3$ (see Fig. 5.10(b)). Collapse is also observed for all Reynolds numbers tested in the long-pipe facility (apart from the lowest, due to imperfect noise filtering), suggesting Reynolds-number-independent wall scaling in this range of Reynolds numbers. The comparison with DNS results by Lee and Moser (2015) at $Re_\tau = 5\,200$, further elaborated in the work of Baars et al. (2024), shows collapse of the LCS even at a lower Reynolds number, indicating universality of this scaling across both channel and pipe flows. The variation of the LCS as a function of streamwise distance from the wall-pressure sensor (at the same azimuthal location in the pipe) for one Reynolds number ($Re_\tau = 14\,004$) is documented in Fig. 5.11(a). Similar conclusions can be drawn for the streamwise variation of $\gamma^2_{up_w^2}(x, \lambda_x)$ in Fig. 5.11(b), as well as for all other tested Reynolds numbers. In the context of real-time control, such an analysis defines what streamwise separation between sensor(s) and actuator(s) is feasible.

The coherence between wall-pressure and streamwise velocity fluctuations reflects the linear interactions that link these two quantities. Specifically, positive fluctuations in the streamwise velocity are typically associated with positive wall-pressure fluctuations, albeit

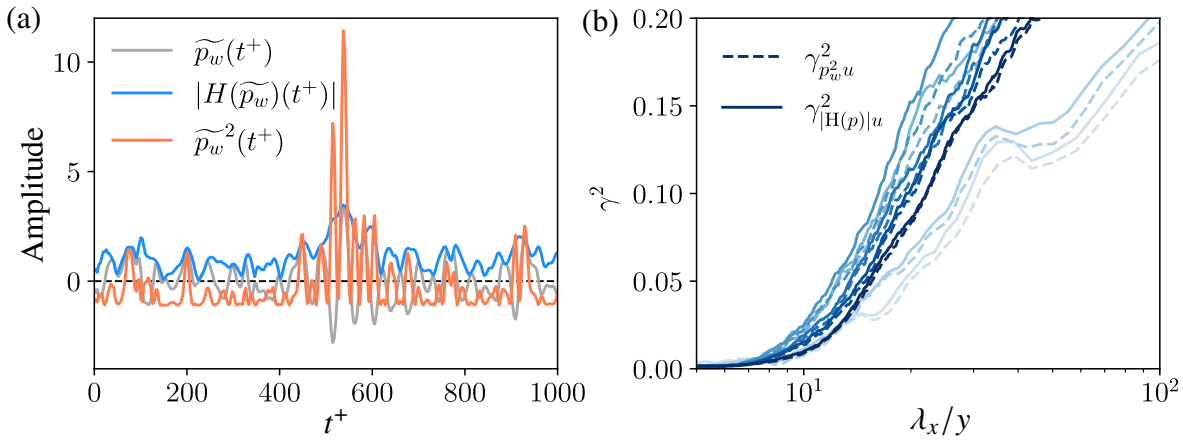

Fig. 5.12 (a) Normalised wall-pressure signal of microphone $\mathcal{M}1$ at $Re_\tau = 14\,004$, its Hilbert transform and the de-meaned wall-pressure–squared signal. (b) LCS between the Hilbert transform of the wall-pressure signal and streamwise velocity fluctuations (solid) at $y = y_A$, compared to the LCS between streamwise velocity and wall-pressure–squared (dashed, same as in Fig. 5.10(b)).

with a certain phase delay (Gibeau and Ghaemi, 2021). However, the mechanism behind the increase in large-scale coherence when considering the squared wall-pressure signal remains less understood. Squaring the wall-pressure signal and observing a corresponding rise in coherence suggests that a modulation effect may be at work. In this scenario, large-scale u fluctuations superimpose onto the flow and nonlinearly alter the wall-pressure field. This indicates a departure from linear dynamics and points towards more complex underlying processes.

To probe this phenomenon more deeply, we employ the Hilbert transform to extract an "envelope" of the wall-pressure signal. This envelope provides a representation of the amplitude variation of the wall-pressure fluctuations over time, which can then be correlated with the fluctuating streamwise velocity signal. Figure 5.12(a) illustrates the normalised wall-pressure signal $[\widetilde{p_w}(t) = p_w(t)/\overline{p_w}]$ at $Re_\tau = 14\,004$, captured at microphone $\mathcal{M}1$ over a short time window. Also shown is the magnitude of the Hilbert transform $|H(p_w)(t)|$, alongside the de-meaned wall-pressure–squared signal. Through visual inspection, it is evident that both the Hilbert-transformed wall-pressure and the squared wall-pressure signal exhibit a similar large-scale structure in their energy content, suggesting a relationship between these quantities.

To quantify this observation, Fig. 5.12(b) presents the large-scale coherence spectra (LCS) between $|H(p_w)(t)|$ and $u(t)$, alongside the LCS between $p_w^2(t)$ and $u(t)$ (as previously shown in Fig. 5.10(b)). A remarkable collapse is observed between the two LCS spectra across all Reynolds numbers tested. This collapse suggests that large-scale variations in wall-

pressure intensity, as captured by both the Hilbert-transformed and squared wall-pressure signals, are closely related to the modulation effects induced by large-scale streamwise velocity fluctuations. These findings offer compelling evidence of the nonlinear coupling between wall-pressure and streamwise velocity fluctuations and demonstrate how large-scale velocity structures modulate the near-wall pressure field, contributing to the overall energy transfer in turbulent flows.

5.4.2 Coherence between wall-normal velocity and wall-pressure fluctuations

To further characterize the dynamics between wall-pressure and velocity events, we extend the analysis presented in the previous section by examining the relationship between wall-pressure fluctuations and wall-normal velocity (v) fluctuations, instead of the streamwise velocity (u) fluctuations. This analysis is important because the wall-normal velocity plays a distinct role in near-wall turbulence dynamics, often linked to the transport of momentum away from the wall. The coherence between $v(t)$ and $p_w(t)$, illustrated in Fig. 5.13(a), reveals a peak at $\lambda_x/y \approx 10$ and $\gamma^2_{vp_w} \approx 0.15$, which is approximately 50% higher than the peak coherence observed between $u(t)$ and $p_w(t)$. This suggests that wall-normal velocity fluctuations have a stronger influence on the wall-pressure than streamwise velocity fluctuations do. Moreover, when the wall-pressure fluctuations are squared, the levels of coherence, denoted by $\gamma^2_{vp_w^2}$, further increase (see Fig. 5.13(b)), with a notable rise starting at $\lambda_x/y \approx 3$. This behaviour remains consistent across all tested Reynolds numbers, indicating a form of Reynolds-number-independence in the coupling between v and p_w^2.

The stronger coherence between wall-normal velocity and wall-pressure fluctuations is consistent with findings in prior studies (*e.g.*, Gibeau and Ghaemi, 2021), and can be physically explained by considering the non-permeability boundary condition at the wall. Specifically, when downward-directed velocity events (those with a negative v component) approach the wall, the fluid is decelerated and stagnates, generating a positive fluctuation in wall pressure. Conversely, upward-directed velocity events (those with $v > 0$) tend to cause a local reduction in pressure near the wall. This reciprocal relationship results in a strong coupling between $v(t)$ and $p_w(t)$. Additionally, the observed peak in coherence occurs at a shorter wavelength than the peak coherence between $u(t)$ and $p_w(t)$, which is consistent with the fact that the most intense v fluctuations are typically concentrated at smaller scales compared to u fluctuations. The distinct role of v fluctuations in redistributing momentum and energy across the boundary layer likely contributes to their more pronounced effect on wall-pressure fluctuations, particularly at shorter wavelengths.

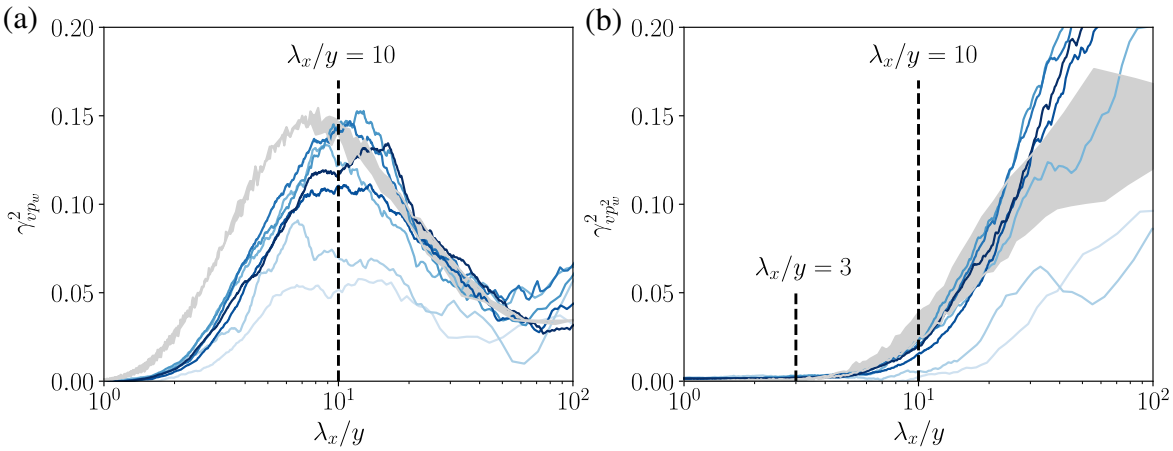

Fig. 5.13 (a) Coherence between wall-normal velocity and wall-pressure and (b) wall-pressure–squared fluctuations at point A for $4\,794 < Re_\tau < 47\,015$. Light grey shaded area illustrates a comparison to DNS data from Lee and Moser (2015).

Chapter 6

Conclusions

This thesis is part of a larger project aimed at developing both active and passive drag reduction strategies while advancing the understanding of scaling laws in turbulent flows. Within this framework, the research addresses critical challenges in high Reynolds number pipe flows, focusing on reducing uncertainty in wall shear stress measurements, exploring scaling laws, and investigating the coherence between wall-pressure and velocity fluctuations—key elements for enabling advanced flow control strategies. To do so, an experimental study was carried out mainly at the Long Pipe facility at the CICLoPE laboratory of the University of Bologna. The facility is exceptional, offering access to high Reynolds number wall turbulence with a level of resolution that is unparalleled elsewhere. The thesis includes a characterization of the uncertainty of wall shear stress combining two different techniques. Oil film interferometry allows obtaining a 'localized' value of skin friction while static pressure drop gives a 'global' information related to τ_w. Wall-pressure fluctuations measured using a sparse sensors setups of microphones are then acquired. Inner and outer scaling laws in pressure fluctuations are addressed after the implementation of a POD based filtering technique to the signal. Moreover, wall-pressure–velocity coherence is assessed in the range of $4\,794 \lesssim Re_\tau \lesssim 47\,015$, combining simultaneous measurements of five different microphones with an Hot-wire and an X-wire acquisitions at different streamwise and wall-normal locations. The specific contributions of this research, which collectively address the overarching goals of advancing drag reduction strategies and scaling law assessments in turbulent flows, can be summarized as follows:

- **Oil Film Interferometry** In this phase of the study, the development and refinement of Oil Film Interferometry (OFI) within the CICLoPE long-pipe facility have established it as a precise local measurement tool for assessing wall shear stress in high Reynolds number turbulent flows. The system's overall uncertainty has been reduced to approx-

imately 0.62%, with an optimized interrogation area of 150 $pixels$ and an acquisition time of $\approx 200\,s$, making OFI a reliable option for detailed turbulence measurements as a the local information. Additionally, OFI was employed to validate opposing flow control techniques in turbulent boundary layers, demonstrating its effectiveness in evaluating control strategies. These advancements highlight OFI's potential in providing accurate, localized wall shear stress data, enhancing the CICLoPE facility's contributions to turbulence and flow control research.

- **Wall shear stress uncertainty** The uncertainty analysis reveals that a 2% error margin is appropriate for comparing wall shear stress measurements obtained through OFI and static pressure drop acquisition. The OFI technique carries a refined uncertainty which is less than 1 %, while the static pressure drop method shows an uncertainty of $\pm 1\%$ due to fitting errors and transducer limitations. Within these bounds, the measurements align well across Re_τ values from 7 000 to 35 000, falling comfortably within the error margin. However, at lower Re_τ values, measurement deviations become more pronounced, likely due to the higher uncertainties in pressure measurements where smaller pressure differences approach the resolution limits of the transducer, such problematic maybe also be caused by the impressive dimension of the Long Pipe facility. Conversely, at higher Re_τ, OFI measurements are increasingly susceptible to environmental influences, such as dust particle buildup on the oil film in the Long Pipe's test-section, which can introduce measurement distortions mainly related to data processing. These findings underscore both the accuracy and the limitations of the OFI and static pressure drop methods. Wavelet analysis along with machine learning algorithms may be a possible solution to overcome limitation at High Re numbers especially for OFI acquisition.

- **Wall-pressure fluctuations** This study has demonstrated the effectiveness of applying classical POD, harmonic POD (hPOD), and Conditional Spectral Analysis (CSA)—to extract key physical insights from wall-pressure measurements in a high Reynolds number turbulent flow setting from a sparse sensor configuration, a common issue while dealing with experimental approach where instruments positioning and accessibility may become challenging. A key obstacle was effectively filtering out facility-related noise while preserving the critical hydrodynamic information characteristic of turbulent wall-bounded flows. The results confirmed that noise-corrected wall-pressure signals successfully captured relevant flow structures, with the filtered energy spectra aligning with the expected small-scale energy peak at $\lambda_x^+ \approx 250$, consistent with near-wall dynamics. A progressive increase in large-scale energy content with higher

Re_τ values was also observed, as predicted in existing literature. When scaling the streamwise wavelength in outer units, the spectra demonstrated good collapse, affirming the physical relevance of the extracted data. The robustness of the noise-filtering approach was further validated by comparing wall-pressure intensities derived through POD, hPOD, and CSA methods with empirical relationships (Klewicki et al., 2007). At high Reynolds numbers, all three models exhibited less than a 5% deviation, indicating reliable filtering performance. Although some discrepancies were noted at lower Re_τ, particularly in the CSA method, these were primarily attributed to limitations in filtering very low-velocity signals where the SNR is minimal. Overall, this study confirms the validity of these models not only for effectively denoising complex turbulent datasets but also for accurately extracting hydrodynamic pressure data; an essential element for applications in flow control and drag reduction. These models provide a solid framework for further turbulence research, ensuring that core flow features are maintained even in noise-prone environments.

- **Wall-pressure–velocity coherence** This investigation offers a detailed experimental campaign into the statistical correlation between hydrodynamic wall-pressure and velocity fluctuations in the logarithmic region of a turbulent pipe flow. By examining this correlation, we aimed to uncover fundamental physical insights as a precursor to developing transfer functions suitable for real-time flow control algorithms. Utilizing a distinctive dataset collected at high friction Reynolds numbers within CICLoPE's Long Pipe facility, our findings demonstrate a consistent linear coherence between wall-pressure and velocity fluctuations in the logarithmic region of turbulent wall-bounded flows. This coherence appears to exhibit both Reynolds-number-independence and universality across various wall-bounded flow types. These findings reveal an inherent, Reynolds-number-independent statistical coherence, providing robust evidence of the potential for scalable, application-ready control strategies based on wall-pressure inputs for real-time flow management.

This experimental work at the CICLoPE Long Pipe facility has advanced wall-turbulence research through the development and application of the Oil Film Interferometry (OFI) technique. Significant progress has been made in minimizing uncertainties in wall shear stress measurements, achieved through careful calibration of the OFI technique and its comparison with static pressure drop data along the Long Pipe. The refined OFI method has not only enabled precise wall shear stress measurements but has also been employed to validate real-time control algorithms in high Reynolds number flows. Additionally, an examination of wall-pressure and velocity coherence in the turbulent flow has provided insights into the

potential for a scalable approach in active drag reduction strategies. Together, these advancements reinforce CICLoPE's role as a key facility for tackling fundamental challenges in turbulence and flow control at high Reynolds numbers, with promising implications for real-time, application-level flow control solutions.

References

Abbassi, M. R., Baars, W. J., Hutchins, N., and Marusic, I. (2017). Skin-friction drag reduction in a high-Reynolds-number turbulent boundary layer via real-time control of large-scale structures. *Intl. J. Heat Fluid Flow*, 67:30–41.

Adrian, R. J. (2007). Hairpin vortex organization in wall turbulence. *Physics of Fluids*, 19(4).

Adrian, R. J., Meinhart, C. D., and Tomkins, C. D. (2000). Vortex organization in the outer region of the turbulent boundary layer. *Journal of Fluid Mechanics*, 422:1–54.

Baars, W. J., Dacome, G., and Lee, M. (2024). Reynolds-number scaling of wall-pressure–velocity correlations in wall-bounded turbulence. *J. Fluid Mech.*, 981:A15.

Baidya, R., Baars, W. J., Zimmerman, S., Samie, M., Hearst, R. J., Dogan, E., Mascotelli, L., Zheng, X., Bellani, G., Talamelli, A., Ganapathisubramani, B., Hutchins, N., Marusic, I., Klewicki, J., and Monty, J. P. (2019). Simultaneous skin friction and velocity measurements in high Reynolds number pipe and boundary layer flows. *Journal of Fluid Mechanics*, 871:377–400.

Bailey, S. C., Kunkel, G. J., Hultmark, M., Vallikivi, M., Hill, J. P., Meyer, K. A., Tsay, C., Arnold, C. B., and Smits, A. J. (2010). Turbulence measurements using a nanoscale thermal anemometry probe. *Journal of Fluid Mechanics*, 663:160–179.

Balakumar, B. J. and Adrian, R. J. (2007). Large-and very-large-scale motions in channel and boundary-layer flows. *Philosophical Transactions of the Royal Society A: Mathematical, Physical and Engineering Sciences*, 365(1852):665–681.

Bellani, G. and Talamelli, A. (2016). The final design of the Long Pipe in CICLOPE. In Peinke, J., Kampers, G., Oberlack, M., Wacławczyk, M., and Talamelli, A., editors, *Progress in Turbulence VI*, pages 205–209, Cham. Springer International Publishing.

Blake, W. K. (1970). Turbulent boundary-layer wall-pressure fluctuations on smooth and rough walls. *J. Fluid Mech.*, 44(04).

Bruun, H. H. (1996). Hot-wire anemometry: principles and signal analysis. *Measurement Science and Technology*, 7(10):024.

Bull, M. K. and Thomas, A. S. W. (1976). High frequency wall-pressure fluctuations in turbulent boundary layers. *Phys. Fluids*, 19(4):597–599.

Burattini, P. and Antonia, R. A. (2004). The effect of different X-wire calibration schemes on some turbulence statistics. *Exp. in Fluids*, 38(1):80–89.

Cadot, O., Douady, S., and Couder, Y. (1995). Characterization of the low-pressure filaments in a three-dimensional turbulent shear flow. *Physics of Fluids*, 7(3):630–646.

Cantwell, B. (1981). Organized motion in turbulent flow. *Annual review of fluid mechanics*, 13(1):457–515.

Choi, H. and Moin, P. (1990). On the space-time characteristics of wall-pressure fluctuations. *Phys. Fluids*, 2(8):1450–1460.

Chue, S. (1975). Pressure probes for fluid measurement. *Progress in aerospace sciences*, 16(2):147–223.

Clean Sky 2 Initiative (2021). Clean aviation goals by 2035. https://www.cleansky.eu/.

Dacome, G., Mörsch, R., Kotsonis, M., and Baars, W. J. (2024a). Opposition flow control for reducing skin-friction drag of a turbulent boundary layer. *Phys. Rev. Fluids*, 9(6):094604.

Dacome, G., Mörsch, R., Kotsonis, M., and Baars, W. J. (2024b). Opposition flow control for reducing skin-friction drag of a turbulent boundary layer. *Phys. Rev. Fluids*, 9(6):064602.

Deck, S., Renard, N., Laraufie, R., and Weiss, P.-E. (2014). Large-scale contribution to mean wall shear stress in high-Reynolds-number flat-plate boundary layers up to $Re_\theta = 13650$. *Journal of Fluid Mechanics*, 743:202–248.

Del Alamo, J. C. and Jiménez, J. (2009). Estimation of turbulent convection velocities and corrections to taylor's approximation. *Journal of Fluid Mechanics*, 640:5–26.

Del Alamo, J. C., Jiménez, J., Zandonade, P., and Moser, R. D. (2006). Self-similar vortex clusters in the turbulent logarithmic region. *Journal of Fluid Mechanics*, 561:329–358.

Discetti, S., Bellani, G., Örlü, R., Serpieri, J., Vila, C. S., Raiola, M., Zheng, X., Mascotelli, L., Talamelli, A., and Ianiro, A. (2019). Characterization of very-large-scale motions in high-re pipe flows. *Experimental Thermal and Fluid Science*, 104:1–8.

Farabee, T. M. and Casarella, M. J. (1991). Spectral features of wall pressure fluctuations beneath turbulent boundary layers. *Physics of Fluids A: Fluid Dynamics*, 3(10):2410–2420.

Fiorini, T. (2017). Turbulent pipe flow-high resolution measurements in ciclope. *PhD thesis*.

Franklin, R. and Wallace, J. M. (1970). Absolute measurements of static-hole error using flush transducers. *Journal of Fluid Mechanics*, 42(1):33–48.

Ganapathisubramani, B., Hutchins, N., Hambleton, W., Longmire, E., and Marusic, I. (2005). Investigation of large-scale coherence in a turbulent boundary layer using two-point correlations. *Journal of Fluid Mechanics*, 524:57–80.

Ganapathisubramani, B., Longmire, E. K., and Marusic, I. (2003). Characteristics of vortex packets in turbulent boundary layers. *Journal of Fluid Mechanics*, 478:35–46.

Gibeau, B. and Ghaemi, S. (2021). Low-and mid-frequency wall-pressure sources in a turbulent boundary layer. *Journal of Fluid Mechanics*, 918:A18.

Guala, M., Hommema, S., and Adrian, R. (2006). Large-scale and very-large-scale motions in turbulent pipe flow. *Journal of Fluid Mechanics*, 554:521–542.

Head, M. and Bandyopadhyay, P. (1981). New aspects of turbulent boundary-layer structure. *Journal of fluid mechanics*, 107:297–338.

Hecht, E. (2002). *Optics*. Pearson education. Addison-Wesley.

Hellström, L. H., Marusic, I., and Smits, A. J. (2016). Self-similarity of the large-scale motions in turbulent pipe flow. *Journal of Fluid Mechanics*, 792:R1.

Horne, M. P. (1989). *Physical and computational investigation of the wall pressure fluctuations in a channel flow*. Phd thesis, The Catholic University of America.

Hutchins, N. and Marusic, I. (2007a). Evidence of very long meandering features in the logarithmic region of turbulent boundary layers. *J. Fluid Mech.*, 579:1–28.

Hutchins, N. and Marusic, I. (2007b). Large-scale influences in near-wall turbulence. *Philos Trans A Math Phys Eng Sci*, 365(1852):647–64.

Hutchins, N., Monty, J. P., Ganapathisubramani, B., Ng, H. C. H., and Marusic, I. (2011). Three-dimensional conditional structure of a high-Reynolds-number turbulent boundary layer. *Journal of Fluid Mechanics*, 673:255–285.

Hutchins, N., Nickels, T. B., Marusic, I., and Chong, M. S. (2009). Hot-wire spatial resolution issues in wall-bounded turbulence. *Journal of Fluid Mechanics*, 635:103–136.

Hwang, Y. (2015). Statistical structure of self-sustaining attached eddies in turbulent channel flow. *Journal of Fluid Mechanics*, 767:254–289.

IATA (10/2020). Aircraft emissions and fuel efficiency. https://www.iata.org/.

ICAO (2019). Fuel efficiency improvements and emission reduction strategies. https://www.icao.int/.

Jiménez, J. and Hoyas, S. (2008). Turbulent fluctuations above the buffer layer of wall-bounded flows. *J. Fluid Mech.*, 611:215–236.

Karman, V. (1930). Mechanische ahnlichten und turbulenz. *Proc. Third Intern. Congr. Appl. Mech.*, 1:85–93.

Kim, K. C. and Adrian, R. J. (1999). Very large-scale motion in the outer layer. *Physics of Fluids*, 11(2):417–422.

King, L. V. (1914). On the convection of heat from small cylinders in a stream of fluid: Determination of the convection constants of small platinum wires with applications to hot-wire anemometry. *Philosophical Transactions of the Royal Society of London Series A*, 214:373–432.

Klewicki, J. and Falco, R. (1990). On accurately measuring statistics associated with small-scale structure in turbulent boundary layers using hot-wire probes. *Journal of Fluid Mechanics*, 219:119–142.

Klewicki, J. C., Priyadarshana, P. J. A., and Metzger, M. M. (2007). Statistical structure of the fluctuating wall pressure and its in-plane gradients at high Reynolds number. *Journal of Fluid Mechanics*, 609:195–220.

Kline, S. J., Reynolds, W. C., Schraub, F. A., and Runstadler, P. W. (1967). The structure of turbulent boundary layers. *Journal of Fluid Mechanics*, 30(4):741–773.

Kolmogorov, A. N. (1941). The local structure of turbulence in incompressible viscous fluid for very large reynolds. *Numbers. In Dokl. Akad. Nauk SSSR*, 30:301.

Lauchle, G. C. and Daniels, M. A. (1987). Wall-pressure fluctuations in turbulent pipe flow. *The Physics of Fluids*, 30(10):3019–3024.

Lee, M. and Moser, R. D. (2015). Direct numerical simulation of turbulent channel flow up to $Re_\tau = 5200$. *J. Fluid Mech.*, 774:395–415.

Ligrani, P. and Bradshaw, P. (1987). Spatial resolution and measurement of turbulence in the viscous sublayer using subminiature hot-wire probes. *Experiments in Fluids*, 5(6):407–417.

Livesey, J., Jackson, J., and Southern, C. (1962). The static hole error problem: An experimental investigation of errors for holes of varying diameters and depths. *Aircraft Engineering and Aerospace Technology*, 34(2):43–47.

Marusic, I. and Monty, J. P. (2019). Attached eddy model of wall turbulence. *Annual Review of Fluid Mechanics*, 51(1):49–74.

Mascotelli, L. (2020). High reynolds number experiments in the long pipe at ciclope. *PhD thesis*.

Mathis, R., Hutchins, N., and Marusic, I. (2009). Large-scale amplitude modulation of the small-scale structures in turbulent boundary layers. *Journal of Fluid Mechanics*, 628:311–337.

McGrath, B. E. and Simpson, R. L. (1987). Some features of surface pressure fluctuations in turbulent boundary layers with zero and favorable pressure gradients. *NASA Contractor Rep.*, 4051.

McKeon, B., Zagarola, M., and Smits, J. (2005). A new friction factor relationship for fullydeveloped pipe flow. *Journal of Fluid Mechanics*.

McKeon, B. J. and Smits, A. J. (2002). Static pressure correction in high reynolds number fully developed turbulent pipe flow. *Measurement Science and Technology*, 13(10):1608.

Monkewitz, P., Duncan, R., and Nagib, H. (2010). Correcting hot-wire measurements of stream-wise turbulence intensity in boundary layers. *Physics of Fluids*, 22(9).

Monkewitz, P. A. and Nagib, H. M. (2015). Large-reynolds-number asymptotics of the streamwise normal stress in zero-pressure-gradient turbulent boundary layers. *Journal of Fluid Mechanics*, 783:474–503.

Monty, J., Stewart, J., Williams, R., and Chong, M. (2007). Large-scale features in turbulent pipe and channel flows. *Journal of Fluid Mechanics*, 589:147–156.

Morrison, J. F. (2007). The interaction between inner and outer regions of turbulent wall-bounded flow. *Phil. Trans. Royal Soc.*, 365(1852):683–98.

Naguib, A. M., Wark, C. E., and Juckenhöfel, O. (2001). Stochastic estimation and flow sources associated with surface pressure events in a turbulent boundary layer. *Phys. Fluids*, 13(9):2611–2628.

Naughton, J. W. and Sheplak, M. (2002). Modern developments in shear-stress measurement. *Progress in Aerospace Sciences*, 38(6-7):515–570.

Nikuradse, J. et al. (1950). Laws of flow in rough pipes. *Translation of the 1933 paper*.

Örlü, R., Fiorini, T., Segalini, A., Bellani, G., Talamelli, A., and Alfredsson, P. H. (2017). Reynolds stress scaling in pipe flow turbulence—first results from CICLoPE. *Philosophical Transactions of the Royal Society A: Mathematical, Physical and Engineering Sciences*, 375(2089).

Panton, R. L., Lee, M., and Moser, R. D. (2017). Correlation of pressure fluctuations in turbulent wall layers. *Physical Review Fluids*, 2(9):094604.

Perry, A. and Chong, M. (1982). On the mechanism of wall turbulence. *Journal of Fluid Mechanics*, 119:173–217.

Perry, A. E., Henbest, S., and Chong, M. S. (1986). A theoretical and experimental study of wall turbulence. *Journal of Fluid Mechanics*, 165:163–199.

Pirozzoli, S., Romero, J., Fatica, M., Verzicco, R., and Orlandi, P. (2021). Reynolds number trends in turbulent pipe flow: a dns perspective. *arXiv e-prints*, pages arXiv–2103.

Pope, S. B. (2000). *Turbulent Flows*. Cambridge University Press.

Prandtl, L. (1926). Application of the" magnus effect" to the wind propulsion of ships. Technical report, NACA.

Rainbird, W. (1967). *Errors in measurement of mean static pressure of a moving fluid due to pressure holes*. National Research Council Canada.

Ray, A. (1956). *On the effect of orifice size on static pressure reading at different Reynolds numbers*. Aeronautical Research Council.

Rayle, R. E. (1949). *An investigation of the influence of orifice geometry on static pressure measurements*. PhD thesis, Massachusetts Institute of Technology.

Renard, N. and Deck, S. (2016). A theoretical decomposition of mean skin friction generation into physical phenomena across the boundary layer. *J. Fluid Mech.*, 790:339–367.

Richardson, L. F. (1922). *Weather prediction by numerical process*. University Press.

Richardson, R., Zhang, Y., and Cattafesta, L. N. (2023). Sensor decontamination via conditional spectral analysis. *Experiments in Fluids*, 64(10):163.

Romano, G. P. (1995). Analysis of two-point velocity measurements in near-wall flows. *Experiments in fluids*, 20(2):68–83.

Ruedi, J. D., Nagib, H., Österlund, J., and Monkewitz, P. A. (2003). Evaluation of three techniques for wall-shear measurements in three-dimensional flows. *Experiments in Fluids*, 35(5):389–396.

Saccenti, E., Hendriks, M. H. W. B., and Smilde, A. K. (2020). Corruption of the Pearson correlation coefficient by measurement error and its estimation, bias, and correction under different error models. *Sci. Rep.*, 10(438).

Sasaki, K., Vinuesa, R., Cavalieri, A. V. G., Schlatter, P., and Henningson, D. S. (2019). Transfer functions for flow predictions in wall-bounded turbulence. *J. Fluid Mech.*, 864:708–745.

Schewe, G. (1983). On the structure and resolution of wall-pressure fluctuations associated with turbulent boundary-layer flow. *J. Fluid Mech.*, 134:311–328.

Schlichting, H. and Gersten, K. (2016). *Boundary-layer theory*. springer.

Schoppa, W. and Hussain, F. (1998). A large-scale control strategy for drag reduction in turbulent boundary layers. *Phys. Fluids*, 10(5):1049–1051.

Segalini, A., Örlü, R., Schlatter, P., Alfredsson, P. H., Rüedi, J.-D., and Talamelli, A. (2011). A method to estimate turbulence intensity and transverse taylor microscale in turbulent flows from spatially averaged hot-wire data. *Experiments in Fluids*, 51:693–700.

Segalini, A., Rüedi, J.-D., and Monkewitz, P. A. (2015). Systematic errors of skin-friction measurements by oil-film interferometry. *Journal of Fluid Mechanics*, 773:298–326.

Shaw, R. (1960). The influence of hole dimensions on static pressure measurements. *Journal of fluid mechanics*, 7(4):550–564.

Smits, A. J., McKeon, B. J., and Marusic, I. (2011a). High–Reynolds number wall turbulence. *Annu. Rev. Fluid Mech.*, 43:353–375.

Smits, A. J., Monty, J., Hultmark, M., Bailey, S. C. C., Hutchins, N., and Marusic, I. (2011b). Spatial resolution correction for wall-bounded turbulence measurements. *Journal of Fluid Mechanics*, 676:41–53.

Squire, L. C. (1961). The motion of a thin oil sheet under the steady boundary layer on a body. *Journal of Fluid Mechanics*, 11(2):161–179.

Tanner, L. H. and Blows, L. G. (1976). A study of the motion of oil films on surfaces in air flow, with application to the measurement of skin friction. *Journal of Physics E: Scientific Instruments*, 9(3):194.

Taylor, G. I. (1938). The spectrum of turbulence. *Proceedings of the Royal Society of London. Series A-Mathematical and Physical Sciences*, 164(919):476–490.

Theodorsen, T. (1952). Mechanisms of turbulence. In *Proceedings of the 2ˆ< nd> Midwestern Conference on Fluid Mechanics, 1952*.

Thomas, A. and Bull, M. (1983). On the role of wall-pressure fluctuations in deterministic motions in the turbulent boundary layer. *Journal of Fluid Mechanics*, 128:283–322.

Tinney, C. E., Shipman, J., and Panickar, P. (2019). Proper-Orthogonal-Decomposition-Based Reduced-Order Models for Characterizing Ship Airwake Interactions. *AIAA Journal*, 58(2):633–646.

Tinney, C. E., Shipman, J., and Panickar, P. (2020). Proper-orthogonal-decomposition-based reduced-order models for characterizing ship airwake interactions. *AIAA J.*, 58(2):633–646.

Tomkins, C. D. and Adrian, R. J. (2003). Spanwise structure and scale growth in turbulent boundary layers. *Journal of Fluid Mechanics*, 490:37–74.

Townsend, A. (1976). *The structure of turbulent shear flow*. Cambridge university press.

Tropea, C., Yarin, A., and Foss, J. (2007). *Springer Handbook of Experimental Fluid Mechanics*. Springer.

Tsuji, Y., Fransson, J. H. M., Alfredsson, P. H., and Johansson, A. V. (2007). Pressure statistics and their scaling in high-Reynolds-number turbulent boundary layers. *J. Fluid Mech.*, 585:1–40.

Welch, P. (1967). The use of fast fourier transform for the estimation of power spectra: a method based on time averaging over short, modified periodograms. *IEEE Transactions on audio and electroacoustics*, 15(2):70–73.

World Economic Forum (2021). Future of zero-carbon aviation. https://www.weforum.org/.

Wu, X. and Moin, P. (2009). Direct numerical simulation of turbulence in a nominally zero-pressure-gradient flat-plate boundary layer. *Journal of Fluid Mechanics*, 630:5–41.

Wyngaard, J. (1968). Measurement of small-scale turbulence structure with hot wires. *Journal of Physics E: Scientific Instruments*, 1(11):1105.

Yu, M., Ceci, A., and Pirozzoli, S. (2022). Reynolds number effects and outer similarity of pressure fluctuations in turbulent pipe flow. *Intl. J. Heat Fluid Flow*, 96:108998.

Zagarola, M., Smits, A., Orszag, S., and Yakhot, V. (1996). Experiments in high reynolds number turbulent pipe flow. In *34th Aerospace Sciences Meeting and Exhibit*, page 654.

Örlü, R., Fransson, J. H., and Henrik Alfredsson, P. (2010). On near wall measurements of wall bounded flows—the necessity of an accurate determination of the wall position. *Progress in Aerospace Sciences*, 46(8):353–387.

List of figures

List of tables

Appendix A: Application to active flow control

In recent years, significant attention has been given to real-time control strategies in turbulent boundary layer (TBL) flows, particularly for applications such as drag reduction and flow manipulation. A crucial aspect of these control systems is the accurate and localized measurement of wall shear stress, which directly influences the near-wall flow dynamics. Oil Film Interferometry (OFI), as discussed in Chapter 3, is a powerful tool for measuring wall shear stress with high spatial and temporal resolution, making it particularly suited for integration into advanced flow control systems.

In this section, we present an application of the OFI technique within a real-time control framework for TBL regulation. By leveraging the precise measurements obtained through OFI, we can better estimate and respond to fluctuations in the near-wall velocity, improving the overall performance of the control system. A schematic of the proposed real-time control system is shown in Fig. 6.1a, illustrating how upstream sensing and downstream actuation zones are linked through a multiple-input single-output (MISO) control strategy, where the wall-based measurements serve as inputs for controlling flow dynamics.

A.1 Turbulent boundary layer facility

Experiments were carried out in an open-return wind tunnel facility (W-Tunnel) at Delft University of Technology. The facility has a cross-sectional area of $0.6 \times 0.6\,\mathrm{m}^2$ at the inlet of the test section and the freestream velocity is set at $U_\infty = 15\,\mathrm{m/s}$. A test section with a length of 3.75 m is employed, comprising a flexible ceiling configured for a zero-pressure-gradient streamwise development of the flow. At a distance of 2.90 m downstream of the trip (P40-grit sandpaper), the TBL attains a thickness of $\delta = 0.07\,\mathrm{m}$ and a friction velocity of $U_\tau = 0.49\,\mathrm{m/s}$, to yield $Re_\tau \approx 2\,240$. The canonical parameters of the TBL flow (including the momentum thickness θ and the wake parameter Π) are reported in Tab. 6.1. Additional details regarding the design and characterization of this TBL facility can be found in the

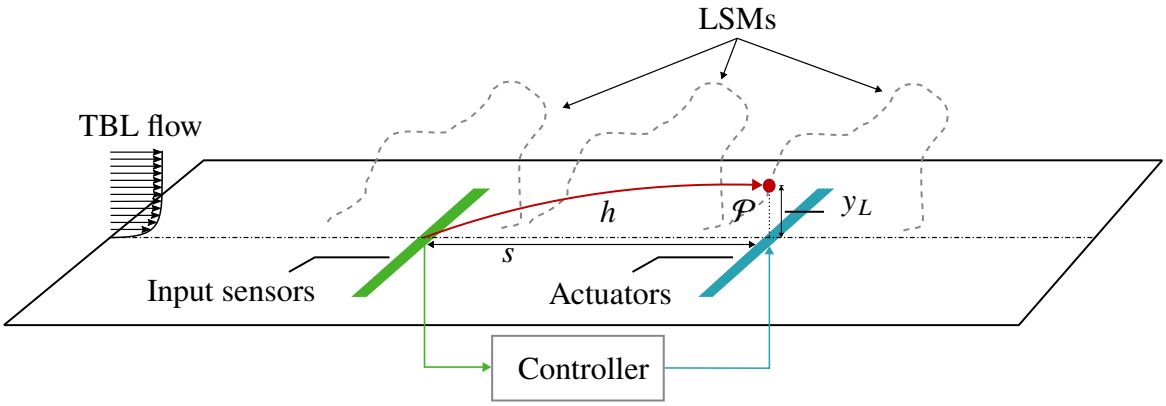

Fig. 6.1 Schematic of the real-time control system implemented in this study, comprising an upstream sensing and a downstream actuation zones.

work of Dacome et al. (2024b). A Cartesian right-handed coordinate system is employed that is centered at $x' = 2.90$ m downstream of the trip and at the spanwise centerline of the test section. A schematic of the experimental setup is presented in Fig. 6.2a.

U_∞ (m/s)	δ (mm)	θ (mm)	Re_θ	U_τ (m/s)	Re_τ	Π	l^* (μm)
15	69.9	6.83	6 830	0.49	2 240	0.61	31.25

Table 6.1 Experimental parameters of the uncontrolled TBL flow in the W-Tunnel facility at $x' = 2.90$ m downstream of the sandpaper trip ($x = 0$).

A.2 Control hardware

For wall-pressure sensing, a spanwise array of seven microphones is used, positioned at $x = -2.4\delta$. The total width of the array is $b = 1.8\delta$, with a spanwise spacing between adjacent sensors of $\Delta z_m = 0.29\delta = 0.17b$. This spacing was selected based on the average spanwise separation of (V)LSMs in a turbulent boundary layer (TBL) (Hutchins et al., 2011). The sensors are GRAS 46BE ¼-in. free-field CCP microphones, with a nominal sensitivity of 3.6 mV/Pa. These microphones have a suitable dynamic range for capturing the pressure fluctuations of interest (35 to 160 dB, referenced to a pressure of $p_{\text{ref}} = 20\mu$Pa) and offer an accuracy of ±1 dB in the 10 Hz to 40 kHz range. Each microphone is mounted within a circular pinhole-cavity, connected to the boundary layer flow via a circular neck-orifice with a diameter of $d_p^+ = 12.8$ ($d_p = 0.4$ mm). Cavity resonance is not a concern, as the resonance frequency, $f_r = 2,725$ Hz, lies well above the frequency range of interest for real-time flow control (Baars et al., 2024).

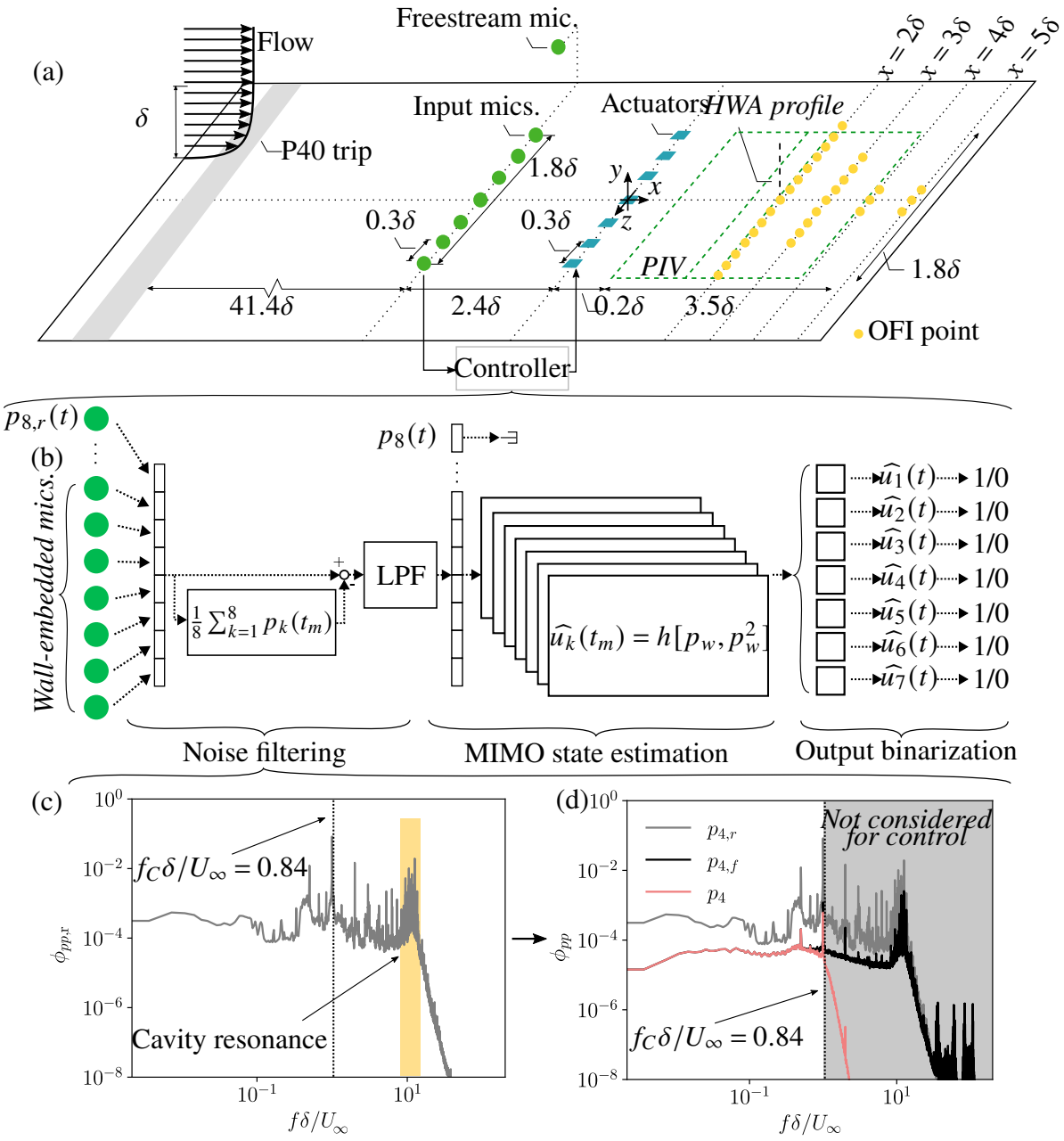

Fig. 6.2 (a) Schematic representation of the control hardware (*i.e.* sensors and actuators) employed for control embedded in the TBL facility. (b) Schematic indicating the real-time processing of the input data through the control logic within one time-step of the controller, running at $f_{\text{loop}} = 10\,\text{kHz}$. Lower insets displaying (c) the spectrum of the raw signal from the central input sensor $[p_4(t)]$ and (d) the spectrum obtained after the application of the noise-filtering procedure and the conditioning low-pass filter on $p_4(t)$.

An additional microphone of the same type was mounted on a streamlined holder in the freestream and fitted with a GRAS RA0020 nosecone to minimize turbulence pressure

fluctuations caused by stagnation. This microphone monitors the acoustic noise generated by the wind tunnel and helps implement noise-removal techniques. Seven unsteady blowing jets with no net mass flux are used as actuators, arranged in a spanwise array and located $s = 2.4\delta$ downstream of the wall-embedded microphones ($x = 0$, see Fig. 6.2a). The spanwise positioning and spacing between the actuators are identical to those of the input sensors. Compressed, dry air is discharged into the TBL through streamwise-elongated rectangular slits with dimensions $0.2\delta \times 0.02\delta$. These actuators are designed to counteract downward-directed large-scale structures from the logarithmic region by inducing an upwash at and downstream of the injection site. The jets operate in an on/off manner, with the exit velocity either set to 0 (off) or $v_{\text{jet}} = 0.4U_\infty$ (on), ensuring the jet plume reaches the logarithmic region without penetrating beyond $y = \delta$ (Dacome et al., 2024b). Figure 6.2a shows the arrangement of the control hardware within the TBL facility.

A.3 Direct skin-friction quantification

The primary goal of the real-time controller is to target large-scale velocity fluctuations in the logarithmic region, as their interaction with smaller scales in the inner region can lead to drag reduction. Suppressing turbulent velocity fluctuations can significantly influence the main mechanisms responsible for generating skin friction (Deck et al., 2014; Renard and Deck, 2016). Figure 6.3 shows the skin-friction values for both the uncontrolled flow and the flow under opposing control. Specifically, Figs. 6.3a and 6.3b depict the absolute wall-shear stress for the two cases, while Fig. 6.3c illustrates the relative change between them, $\Delta\tau_w = 100 \times (\tau_{w,\text{opp}} - \tau_{w,\text{unc}})/\tau_{w,\text{unc}}$. The relative difference indicates a positive drag reduction across most measurement points, with some deviations at $x = 2\delta$ and $x = 3\delta$. These deviations are likely due to post-processing or measurement errors rather than actual physical inconsistencies in wall shear. Nonetheless, when considering the overall trend, the skin-friction drag shows a spanwise uniformity in both the controlled and uncontrolled flows. At these downstream locations, the wake of the jet-induced actuator flow near the wall is not influenced by spanwise variations in the flow in the logarithmic region and above.

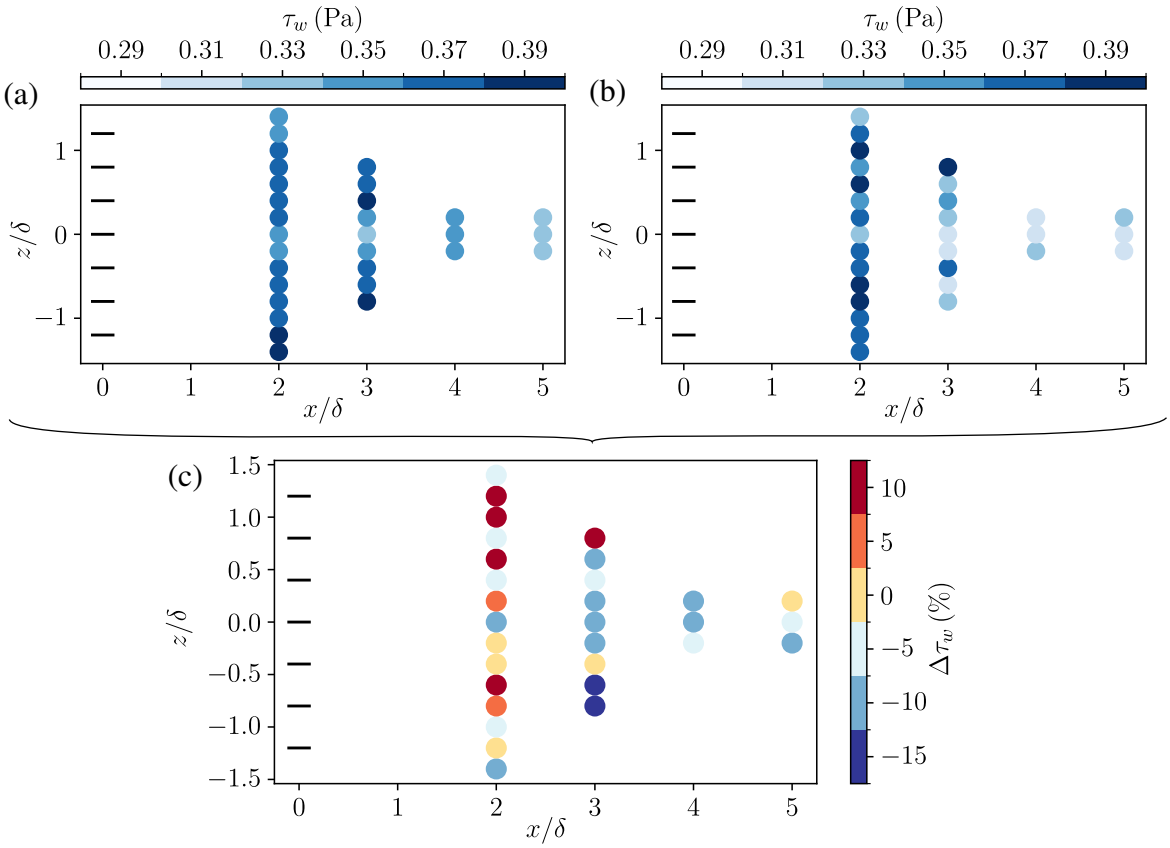

Fig. 6.3 Absolute wall-shear stress at several locations on the wall downstream of the jet actuators obtained from OFI data for (a) the uncontrolled flow and (b) the flow subject to opposing control. (c) Relative difference between the wall-shear stress of the opposing and uncontrolled cases.

Appendix B: Report on the weather events of May 16, 2023

Authors: Alessandro Talamelli, Gabriele Bellani, Lorenzo Lazzarini, Rithvik Magal, Lorenzo Magnani, Alex Ravaioli, Yari Basso

Affiliation: Dipartimento di Ingegneria Industriale, Università di Bologna CIRI Aerospace, Università di Bologna

Abstract

On May 16, 2023, the CICLoPE Laboratory in Predappio was significantly impacted by severe weather events, resulting in landslides and extensive flooding. Several areas of the facility suffered damage, including blocked emergency exits, flooded tunnels, and compromised parts of the return circuit of the wind tunnel. Efforts to manage the emergency began immediately, with subsequent actions aimed at draining water, clearing mud, and restoring accessibility. During the following months, a series of recovery operations were performed, including debris removal, structural reinforcements, and drainage improvements. Restoration efforts continued into 2024, with the final steps focused on securing the laboratory infrastructure and restoring safe access. This report documents the emergency response, damage assessment, and comprehensive recovery operations required to rehabilitate the CICLoPE facility for future research activities.

B.1 Emergency management

The areas affected by the events are shown in the diagram in Fig.B.4. On Tuesday, 16 May, several landslides affected the terrain in which the laboratory is located. From a survey conducted some days later, the situation is described in detail in the survey shown in Fig. B.5. The relief has 4 significant landslides indicated by A, B, C, D, and E. Around 3 PM the relief near the emergency exit, C, with consequent flooding of the transverse tunnel of escape (area 4). The entire emergency exit floods in a few hours. Also on Tuesday, two smaller landslides are generated near the main entrance (B, E) that cause an influx of water and land. In addition, two smaller landslides are generated near the main entrance (B, E) that cause an influx of water and land, as can be seen in Fig.B.7.

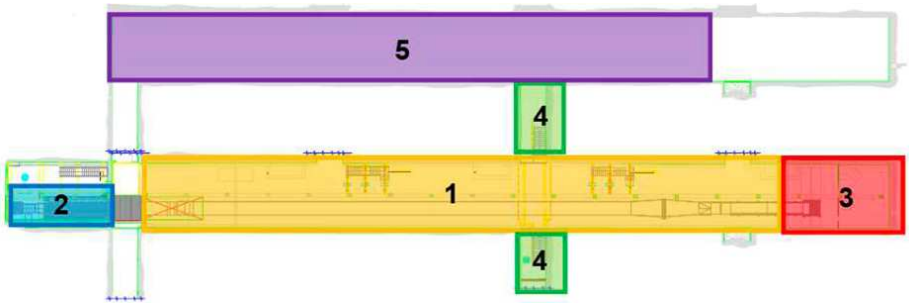

Fig. B.4 Schematic of areas affected by flooding in CICLoPE Laboratory.

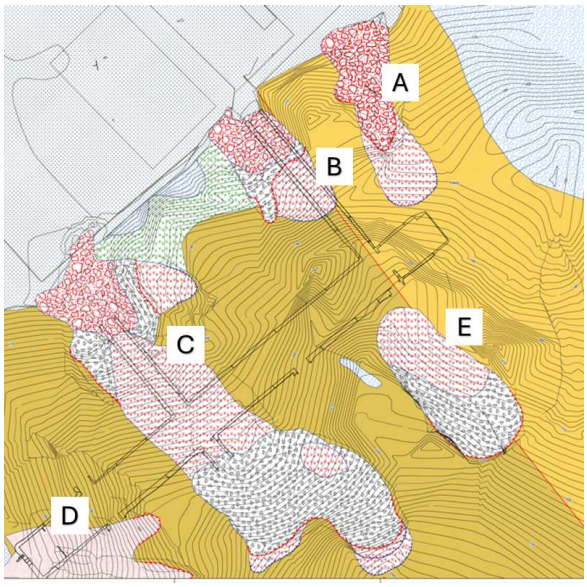

Fig. B.5 Relief of landslides affecting the CICLoPE Laboratory.

Fig. B.6 Landslide on emergency exit (C).

Fig. B.7 Landslide near main entrance (B, E).

On Wednesday 17 a survey of the tunnels shows that at the main entrance a large pool of water mixed with mud has formed and arrives at the level of the parking lot in front

Fig. B.8 Flooding near the main entrance.

Fig. B.9 Mud removing operations using a water pump.

On Thursday 18, a pump is purchased to evacuate stagnant water at the main entrance. After the evacuation of water, a significant amount of mud remains in the entrance door. The quantity and compactness prevent manual removal. The Mayor of Predappio is alerted, who puts us on a list for mechanical intervention.

On the morning of Friday 19 it is noticed that the water has again filled the access area (see Fig.B.10). This suggests the need to clear access from water and mud and at the same time restore the water purging system before further rains occur.

Fig. B.10 Flooding near the main entrance.

The escape corridor adjacent to the mountain is completely blocked (see Fig.B.11).

Fig. B.11 Obstruction of the corridor leading to the emergency exit.

On Monday 22, taking advantage of the good weather, the entrance is cleared (see Fig.B.12). We were then able to access the inside to make a quick check of the situation. The lower floor has a widespread flooding, caused by the collapse of the border wall with Matturro. The collapse is related to the filling of the underground room due to the D. There

are debris (even large) up to the engine system. The depth of flooding varies from almost zero near the ground floor in front of the baths to 15-20 cm at the end of the tunnel.

Fig. B.12 Caption

Fig. B.13 State of the laboratory at first entrance following the flood of 16 May.

The cavity is completely filled with water and the part of the return circuit in stainless steel, fully submerged, has raised about 50 cm going to raise the floating floor (see Fig.B.14) and damaging the wall of plasterboard. The rise of the stainless steel elements caused a general rise of the tunnel up to the test chamber which was uprooted from the supports (see Fig.B.16). The supports also failed in the carbon fiber elements before the "test section".

The whole part of the circuit, from the submerged elements to the carbon fiber element in front of the laboratory will have to be dismantled and revised (see Fig.B.15). The structure of the upper floor seems to have not been damaged. Likewise the second adjacent tunnel.

Fig. B.14 Laboratory situation at first entrance after the flood of 16 May.

Fig. B.15 damage to plasterboard and flooding of the lower cavity housing part of the wind tunnel return circuit.

Fig. B.16 Lifting of the tunnel due to the floating of the wind tunnel.

On Tuesday, 23 May, a task of clearing the area in front of it was assigned to an enterprise from Predappio that by means of small excavators and bobcats eliminated the soil present in entry freeing the entire gate of access.

Fig. B.17 First clearance activities at the main entrance.

On Wednesday 24, an attempt was made to clear the access corridor from the deposited mud. Unfortunately, the very liquid state of the mixture present within the corridor did not allow the use of means for which it was necessary to proceed by hand.

Simultaneously, work was carried out to clear the water pumping and evacuation system. First, drainage from manhole 2, located in front of the entrance to manhole 1 at the center of the square, was restored. This process functions by gravity and does not have pumps. Second, the inlet grate 3, which channels water into manhole 2, was cleaned, and the pump

Fig. B.18 Flooding at the main entrance with mud-removal operations, showing two different stages.

that transports water from the central grate 4 to manhole 1 was activated. Finally, pump 5 was reactivated to start evacuating water into the basin of the return circuit.

On the afternoon of Wednesday, May 24, Professor Berti, a geologist from the Alma Mater, conducted an inspection. Professor Berti visually inspected the entire ridge of the collapsed mountain, and, using a drone, was able to examine the conditions of the landslide areas more closely. The type and shape of the landslide do not allow for a simple clearing of the emergency exit; instead, consolidation work is needed first.

On Thursday, May 25, ventilation was restored, allowing for the evacuation of humidity in the tunnels and helping to preserve the infrastructure. Additionally, the most important equipment was transferred to the Visitor Center. Meanwhile, the pump was left operating to continue emptying the water in the underground cavity.

On Monday, May 29, it was observed that the gradual removal of water had returned the gallery to its original position. Any potential damage to parts of the return circuit and the PIPE positioning system must be assessed and quantified.

B.2 Recovery activities

August 2023

In August, the *Brigadeci* company set up the construction site to restore the laboratory . The site was cleared, and mud was removed from areas 1, 2, and 3, which was appropriately analyzed before disposal. All damaged drywall walls in area 2 were removed, and all debris from the collapse of the wall in area 3 was cleared and disposed of (see Fig.B.19). The flooring in area 2 was removed, and the drywall walls were restored. Additionally, the upper part of area 4 was emptied (see Fig.B.20,B.22,B.23).

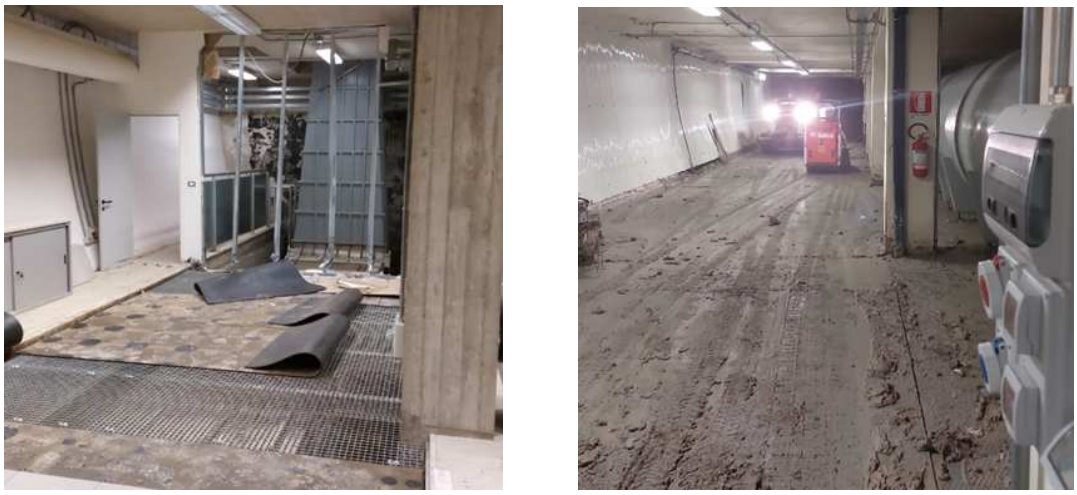

Fig. B.19 Removal of floating floor and mud in the main entrance.

Fig. B.20 Removal of debris caused by the break-in of the separation wall.

Fig. B.21 Recovery of return circuit placed in the cavity under the floor.

Fig. B.22 Area 3 recovery operations.

Fig. B.23 External deposit of mud and solid debris.

September 2023

Reinforcement of the ceiling in area 3 (see Fig.B.24, B.25). Demolish all the walls. The mud was removed and transported to the collection point in Predappio Alta. The debris was loaded and delivered. An armed brickwork was laid to isolate the laboratory from the landslide D which destroyed the Matturro shed. Clean up all areas of interest.

Fig. B.24 Restoration and closure of the landslide access in area 3.

Fig. B.25 Restoration and closure of the landslide access in area 3.

Fig. B.26 Restoration of laboratory floor/walls and return circuit.

November 2023

Restoration of the return circuit. Repair of the carbon fiber duct and its positioning system, which had been damaged by the lifting movement. Replacement of the flooring and drywall walls.

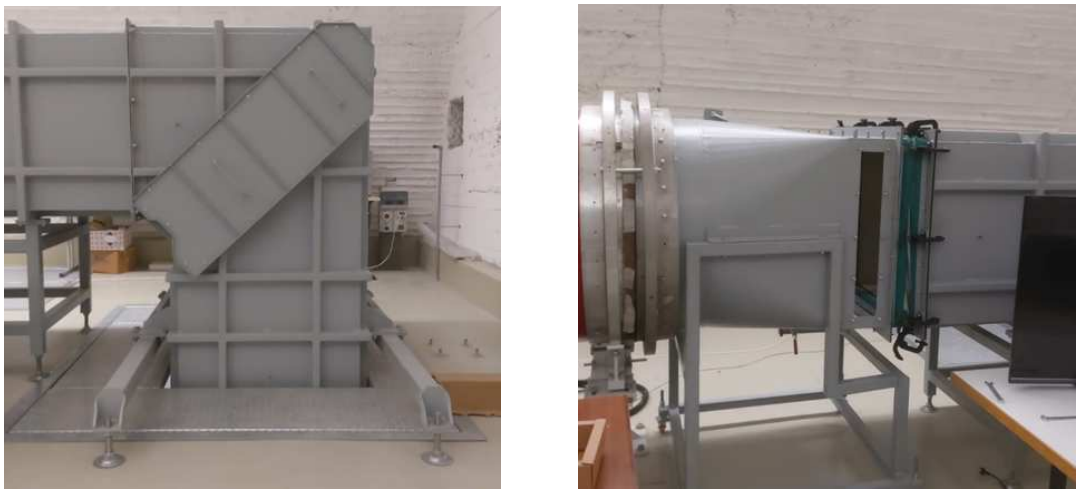

Fig. B.27 Restoration of laboratory floor/walls and return circuit.

Fig. B.28 Repair of the pipe supports damaged by the lifting movement.

March 2024

Removal of soil near the main entrance. Restoration of drainage areas. Repair of the boundary fence with the neighboring property. Finally, the square in front of the tunnel entrance was restored, along with the drainage systems. The fence near the road was also repaired.

Fig. B.29 Removal of the landslide near the main entrance. Installation of drainage material and restoration of the fence.

Fig. B.30 Removal of the landslide near the main entrance. Installation of drainage material and restoration of the fence.

Fig. B.31 Removal of the landslide near the main entrance. Installation of drainage material and restoration of the fence.

Fig. B.32 Repairing the drainage system

Appendix C: Centerline mean velocity trends and normal stress in the long pipe

Abstract

The CICLoPE facility at the University of Bologna in Forli, Italy, is a unique facility providing fully developed pipe flow up to Reynolds numbers near Re_τ of 50,000 with exceptional spatial resolution and stable operating conditions as described by Fiorini (2017) and Mascotelli (2020), and illustrated in Chapter 2. Measurements obtained over the last two years, on the centerline of the pipe in the fully developed test section, with pitot probes for streamwise mean velocity (±0.2% accuracy) and hot wires for the streamwise normal stress (±5% accuracy) are reported here and compared to other data.

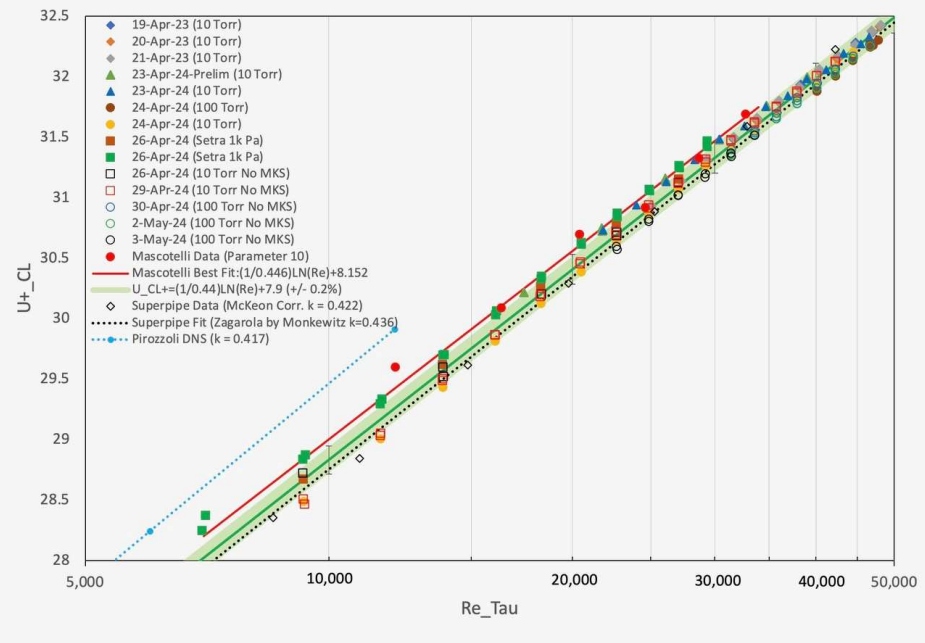

Fig. C.33 Centerline mean velocity from CICLoPE compared to other data

Figure C.33 compares the measurements to earlier data from CICLoPE by Fiorini (2017) and Mascotelli (2020), to the superpipe data of McKeon et al. (2005), and to the DNS results of Pirozzoli et al. (2021). The large amount of data obtained with several pressure transducers and repeated over one year provide a reliable correlation of the centerline velocity to equal (1/0.44) Ln(Ret) + 7.9, providing a Kármán coefficient for pipe flow of 0.44.

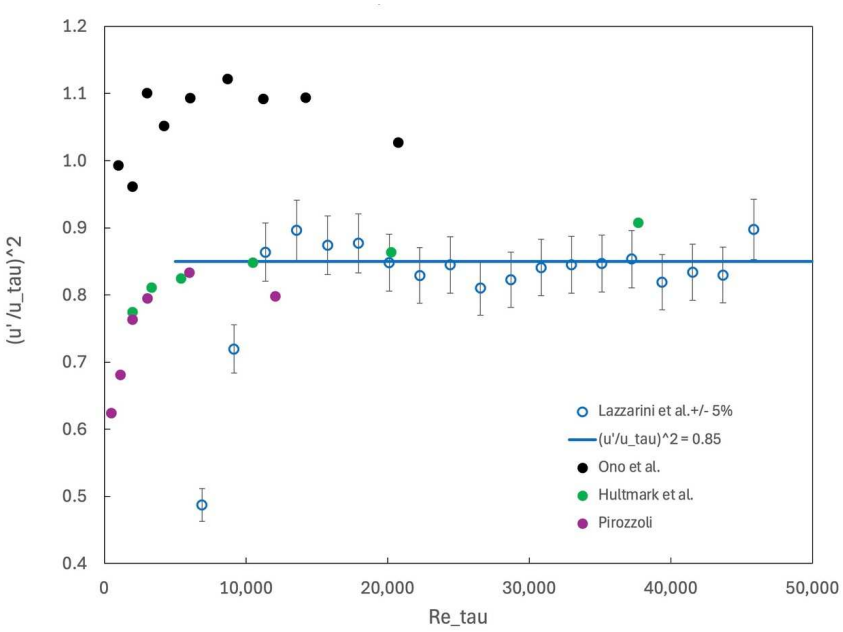

Fig. C.34 centerline normal stress with comparison

Figures C.34 and C.35 reveal high Reynolds number trends of the streamwise normal stress to be constant and equal to 0.85, the skewness to equal -0.5 and the kurtosis to equal 3.5, all with high degree of certainty.

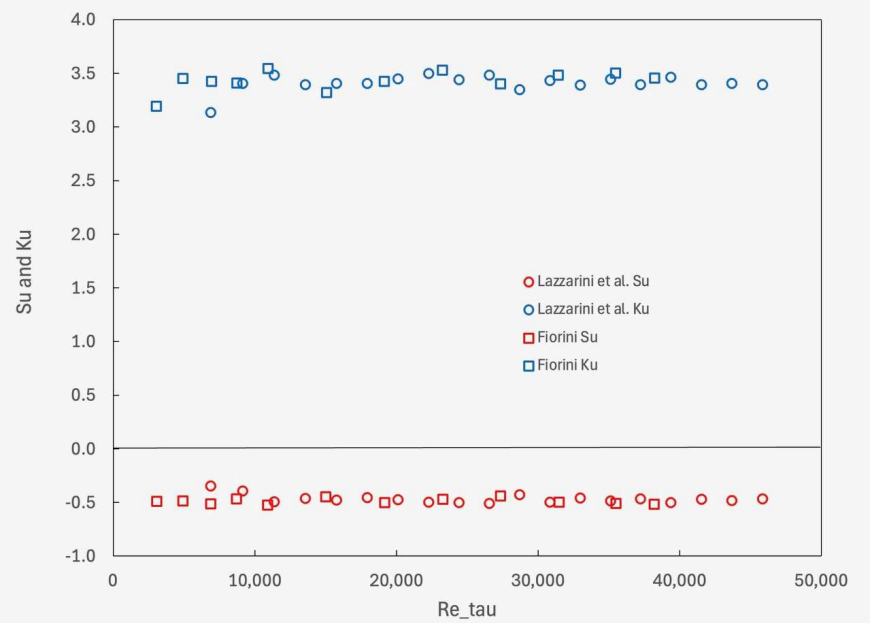

Fig. C.35 Skewness and kurtosis from CICLoPE